

TOPICAL REVIEW

Pseudopotential-based studies of electron transport in graphene and graphene nanoribbons

To cite this article: Massimo V Fischetti *et al* 2013 *J. Phys.: Condens. Matter* **25** 473202

View the [article online](#) for updates and enhancements.

You may also like

- [Dominant scattering mechanism in SiC MOSFET: comparative study of the universal mobility and the theoretically calculated channel mobility](#)
Teruyuki Ohashi, Ryosuke Iijima and Hiroshi Yano

- [High-performance N-polar GaN enhancement-mode device technology](#)
Uttam Singisetty, Man Hoi Wong and Umesh K Mishra

- [The magnetic moment enigma in Fe-based high temperature superconductors](#)
Norman Mannella

TOPICAL REVIEW

Pseudopotential-based studies of electron transport in graphene and graphene nanoribbons

**Massimo V Fischetti¹, Jiseok Kim¹, Sudarshan Narayanan¹,
Zhun-Yong Ong¹, Catherine Sachs¹, David K Ferry² and Shela J Aboud³**

¹ Department of Materials Science and Engineering, The University of Texas at Dallas, Richardson, TX 75080, USA

² School of Electrical, Computer, and Energy Engineering, Arizona State University, Tempe, AZ 85287, USA

³ Energy Resources Engineering Department, Stanford University, Stanford, CA 94305, USA

E-mail: max.fischetti@utdallas.edu

Received 9 August 2013

Published 18 October 2013

Online at stacks.iop.org/JPhysCM/25/473202

Abstract

The theoretical understanding of electron transport in graphene and graphene nanoribbons is reviewed, emphasizing the help provided by atomic pseudopotentials (self-consistent and empirical) in determining not only the band structure but also other fundamental transport parameters such as electron–phonon matrix elements and line-edge roughness scattering. Electron–phonon scattering in suspended graphene sheets, impurity and remote-phonon scattering in supported and gated graphene, electron–phonon and line-edge roughness scattering in armchair-edge nanoribbons are reviewed, keeping in mind the potential use of graphene in devices of the future very large scale integration technology.

(Some figures may appear in colour only in the online journal)

Contents

1. Introduction	3.3. Dielectric screening	15	
2. Electronic structure of graphene and armchair-edge nanoribbons	3.4. Electron–phonon scattering rates	16	
2.1. Density functional theory and empirical pseudopotentials	2	3.5. Electron mobility and drift velocity	17
2.2. Carbon and hydrogen empirical pseudopotentials	2	4. Electron transport in armchair-edge graphene nanoribbons	20
2.3. Band structure of graphene	3	4.1. Electron–phonon interaction and electron mobility	21
2.4. Graphene nanoribbons	3	4.2. Line-edge roughness scattering	24
2.5. Ab initio thermodynamics	4	5. Additional scattering processes in supported graphene	29
2.6. Phonon spectra in graphene	5	5.1. Remote-phonon scattering	29
3. Electron transport in graphene	8	5.2. Charged-impurity scattering in supported and top-gated graphene	32
3.1. Electron–phonon Hamiltonian	9	6. Conclusions	34
3.2. Electron–phonon matrix elements	10	Acknowledgments	34
	13	References	34

1. Introduction

A current welcome development in the study of electronic transport in nanometre-scale structures and devices is the use of tools historically limited to the study of the atomic and electronic structure of crystals to determine transport characteristics. For example, an excellent and comprehensive review of the electronic properties of a two-dimensional electron gas (2DEG) published in 1982 [1] paid little attention to—and made no use of—the ionic (pseudo)potentials of Si when dealing with Si inversion layers and analysing their transport properties. In contrast, a more recent review of a similar study of the electronic properties of—and transport in—graphene [2] relies quite heavily on the details of the atomic configuration and how it affects the electronic properties. This change of attitude is probably due to the improved accuracy of band structure calculations via density functional theory (DFT), as well as increased computing power, but it is also dictated by the necessity of extracting basic transport parameters—such as effective masses and deformation potentials, for example—which are not easily obtained from experiments when dealing with the novel structures, systems, and materials which are being explored in our attempts to scale electronic devices for the future very large scale integration (VLSI) technology.

Here we present a partial review of the present theoretical understanding of electron transport in *ideal* graphene as it is emerging from these pseudopotential-based studies. We shall largely ignore disorder and its effect on transport, a topic that has been recently reviewed by Mucciolo and Lewenkopf [3] and is also the focus of the review of the electronic properties of graphene nanostructures by Molitor and co-workers [4]. We shall also ignore studies motivated explicitly by the analogy of the electronic dispersion in graphene with the dynamics of (massless) Dirac fermions and on their chiral properties leading to such unique transport phenomena as a finite universal DC conductivity at the neutrality point, Klein tunnelling, or an anomalous quantum Hall effect, as reviewed in [2], as well as interesting electro-optical properties, such as a frequency-independent absorption of undoped graphene [5] and an approximately universal AC conductivity at large frequencies [6]. Such a narrow focus will allow us to emphasize the connection between what are usually called *ab initio* methods (term arguably used beyond its etymological meaning and here stretched to include empirical pseudopotentials) and electronic transport itself. Indeed, this connection is particularly important in the case of graphene: when dealing with such a novel material, whose promise does not need to be reiterated [7] but is still in its technological infancy, we have to assess its potential limits in the ideal scenarios that only theory can provide. This review is partial in many ways: we shall consider only ideal single-layer graphene and ribbons; we shall deal only with steady-state transport, ignoring the high-frequency response; and we shall review critically only the literature that is strictly connected with our own original work. Specifically (and here we provide a brief synopsis of this review) in section 2 we shall first review DFT and empirical pseudopotential (EP)

based calculations of the electronic properties of graphene and graphene nanoribbons. While the former's main attraction is the ability to provide reliable atomic configurations, its ‘bandgap problem’ and heavy computational cost (both quickly disappearing issues) make it still less attractive for analysing electron transport, and more agile EP-based calculations are still useful. The particular case of C is almost unique, since flexible EPs have been provided [8] which reproduce remarkably well not only the band structure of both sp^3 -coordinated diamond and sp^2 -coordinated graphene, but also of bent C nanotubes (CNTs).

We shall then consider the intrinsic electron–phonon interaction in suspended ideal single-layer graphene sheets (sections 3.1–3.4), since this constitutes an unavoidable scattering process which sets the upper bounds for the ultimate electronic performance of graphene. For this reason the strength of the interaction in the context of electronic transport has been studied using DFT [9], EPs [10], and other atomistic models [11, 12]. We shall then see in section 3.5 how these results have been used to study the electron mobility [13–15] and high-field drift velocity [16–22].

Opening a gap is a requirement if we wish to use single-layer graphene as a channel material for nanoelectronic logic applications, and this can be achieved by employing graphene in the form of armchair-edge nanoribbons. Therefore, given their utmost practical interest, we review in section 4 the study of electron transport in these systems, focusing on the present understanding of the electron–phonon coupling [23–32] and its impact on the electron mobility and high-field velocity, discussed in section 4.1. In section 4.2 we also discuss the important role played by scattering due to roughness at the edges [23, 33].

Finally, in any realistically envisioned use, graphene will be supported by a polar insulator—and possibly be gated. Therefore additional scattering processes are expected to limit the electrical performance of these supported systems and are reviewed in sections 5.1 and 5.2: scattering with interfacial excitations resulting from the coupling, or ‘hybridization’, of the polar-optical modes of the substrates and the plasmons of the graphene sheet (modes often referred to as ‘remote phonons’, somewhat improperly) [34–41] and scattering with charged impurities in the substrate or gate [42–47].

2. Electronic structure of graphene and armchair-edge nanoribbons

Understanding charge transport in solids requires three distinct ingredients: an accurate knowledge of the electronic excitation spectrum of the structure, needed to treat the kinematics of the charge carriers; an accurate treatment of the collision processes governing the transport; and a set of equations (semiclassical or quantum) together with the algorithms needed to solve them—numerically in most interesting cases. In the following we shall not delve into the latter issue, limiting our discussion to the semiclassical study of the electron mobility and velocity–field characteristics employing the Boltzmann transport equation. Instead, this section and section 2.1 will focus on the former issues. In

Table 1. Local pseudopotential parameters for C and H from Kurokawa *et al* [8]. The pseudopotentials are normalized to the atomic volume of C in diamond.

	b_0	b_1	b_2	b_3	b_4	b_{-1}	b_{-2}	b_{-3}	b_{-4}	E_{cutoff}
C		1.781	1.424	0.354	0.938					15
H	-0.397	0.02759	0.1754	-0.0531		0.0811	-1.086	2.71	-2.86	15

particular, this section will deal with the atomic and electronic (band) structure of ideal single-layer graphene sheets and of nanoribbons.

2.1. Density functional theory and empirical pseudopotentials

As mentioned in our opening paragraph, DFT calculations of the electronic structure of materials, and specifically graphene and graphene nanoribbons, are becoming routine. In general, the benefit of using DFT versus the local EP (LEP) approaches presented here stems from the ability of DFT to compute the atomic equilibrium position through a conjugate-gradient optimization using the Hellmann–Feynman forces or more rigorous methods such as the QMMD [48]. Atomic positions may change due to edge relaxation (nanoribbons, nanoribbons terminated with various functional groups), reconstruction on the edges [49] or plane (e.g., graphane [50]), and strain [51] influencing the electronic structure and transport properties. On the other hand, due to the computational intensity of *ab initio*-based methods, DFT is still restricted to simulations of relatively small structures (hundreds to thousands of atoms) whereas EP can be used to compute the band structure of structures with orders of magnitude more atoms ($\gtrsim 10^5$ atoms) [52]. Using the two methods in conjunction permits a calibration of both DFT and EP methods.

The band structure computed from EP will generally be more realistic for excited states (conduction band) compared to DFT, since the parameters have been calibrated with experimental measurements, whereas DFT can be used to investigate the effects of geometric optimization.

In the rest of this subsection we shall follow mainly [53], a reference that covers the use of empirical pseudopotentials to study the electronic structure and transport in a range of materials and structures wider than what is discussed here.

2.2. Carbon and hydrogen empirical pseudopotentials

Empirical pseudopotentials suffer from their lack of portability, since the screening effect of valence electrons is empirically frozen for each particular atomic configuration. Indeed the eigenvalue problem to be solved can be written as:

$$\sum_{\mathbf{G}'} \left[\frac{\hbar^2}{2m} |\mathbf{k} + \mathbf{G}|^2 \delta_{\mathbf{G}, \mathbf{G}'} + V_{\mathbf{G}-\mathbf{G}'}^{(\text{lat})} \right] u_{\mathbf{G}', \mathbf{k}}^{(n)} = E_n(\mathbf{k}) u_{\mathbf{G}, \mathbf{k}}^{(n)}, \quad (1)$$

where the eigenvectors $u_{\mathbf{G}, \mathbf{k}}^{(n)}$ are the Fourier components of the Bloch functions

$$\psi_{\mathbf{k}}^{(n)}(\mathbf{r}) = \frac{1}{\Omega} e^{i\mathbf{k} \cdot \mathbf{r}} \sum_{\mathbf{G}} u_{\mathbf{G}, \mathbf{k}}^{(n)} e^{i\mathbf{G} \cdot \mathbf{r}}, \quad (2)$$

the eigenvalues $E_n(\mathbf{k})$ give the dispersion in band n , \mathbf{G} are the vectors of the reciprocal lattice, and Ω is a normalization volume. In this equation $V_{\mathbf{G}}^{(\text{lat})}$ are the Fourier components of the pseudopotential which implicitly lump the contributions (Hartree and exchange–correlation) of the valence electrons.

It is therefore remarkable that for the case of carbon Kurokawa *et al* [8] have proposed a local empirical pseudopotential that yields satisfactory results for the cases of sp^3 -coordinated diamond as well as for sp^2 -coordinated *trans*-polyacetylene (that is, essentially 3-wide armchair nanoribbons). The Fourier components of this empirical pseudopotential for C are determined by:

$$V_{\text{C}}(q) = \frac{b_1(b_3q^2 - b_2)}{e^{b_3q^2 - b_4} + 1}, \quad (3)$$

and, for H:

$$V_{\text{H}}(q) = \begin{cases} b_0 + b_1q + b_2q^2 + b_3q^3 & \text{for } (q \leq 2) \\ b_{-1}/q + b_{-2}/q^2 + b_{-3}/q^3 + b_{-4}/q^4 & \text{for } (q > 2). \end{cases} \quad (4)$$

Here q denotes the magnitude of a vector \mathbf{q} in reciprocal space. Table 1 lists the parameters appearing in the expressions above. Kurokawa *et al* have successfully employed this pseudopotential to study amorphous C–H-based crystallites. This C pseudopotential can also be used to calculate the band structure of graphene, as shown below, and of CNTs, as shown in [53]. Another remarkable property of this EP consists of the fact that among the many other empirical pseudopotentials proposed for C in the diamond structure, local [54] and nonlocal [55], Kurokawa *et al* provide an expression which is both suitable for a general q —and not only for the vectors \mathbf{G} of the reciprocal lattice of diamond—as well as yielding the correct workfunction for C in the diamond structure [8].

Using a cutoff energy of 25 Ryd, the plane-wave method used here yields an indirect diamond $\Gamma'_{25}-\Delta_1$ gap of about 5.0 eV and reasonable values also for the direct $\Gamma'_{25}-\Gamma_2$, X_4-X_1 , and L'_3-L_3 gaps. For numerical convenience in the following we present results obtained employing a cutoff energy of 15 Ryd, which yields almost the same direct gap, but a slightly smaller value for the indirect $\Gamma'_{25}-\Delta_1$ gap of 4.2 eV. We have spot-checked our results for graphene, nanoribbons, and CNTs employing a larger cutoff of 25 Ryd without finding any significant difference. Finally, we have neglected the spin–orbit interaction because of its small strength in C [56]. This permits the study of a more general structure than diamond or graphene, such as strained structures, ribbons, bilayers, and CNTs.

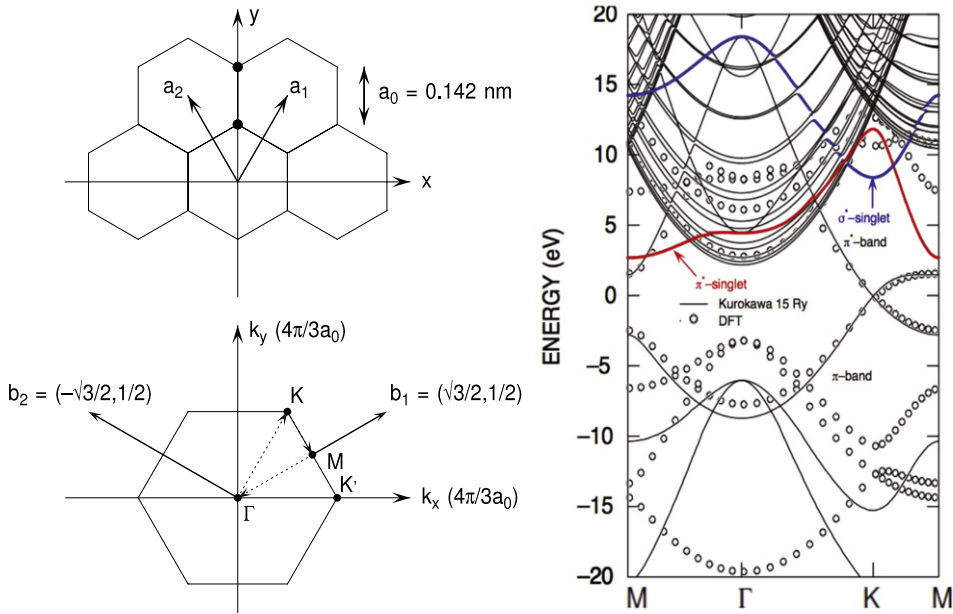


Figure 1. Top left: primitive translation vectors and position of the atoms (dots) for graphene. Bottom left: hexagonal 2D Brillouin zone of graphene, main symmetry points, and trajectory in k -space employed in the plot at right. Right: band structure for graphene obtained using the Kurokawa empirical pseudopotentials (solid lines) and self-consistent pseudopotentials (DFT, dashed lines). A separation of $10\sqrt{3}a_0/2$ along z has been assumed between adjacent sheets. The bands highlighted in colour and indicated by arrows are the σ^* (blue) and π^* (red) singlet bands, whose interaction and hybridization result in an interesting and unexpected behaviour of the bandgap in single-wall zigzag ($n, 0$) carbon nanotubes of small diameter when using EPs. The use of Kurokawa pseudopotentials, in particular, yields relatively small energies for the π^* -singlet band along the $M-\Gamma$ line (≈ 2.5 eV above the Fermi level) compared to energies three times as large obtained using the self-consistent DFT shown here and also reported in the literature [58, 59].

We shall now present results for the band structure of graphene and graphene nanoribbons (GNRs) obtained using Kurokawa's LEPs.

2.3. Band structure of graphene

As is generally the case when using plane-wave methods, the calculation of the electronic excitation spectrum of structures that are periodic in three dimensions, a supercell is constructed to recover the lost periodicity in one dimension (infinite graphene sheet) or in two dimensions (GNRs and CNTs). Here the band structure of an infinite graphene sheet has been calculated assuming the sheet is contained in a supercell, and various supercells are replicated periodically so that neighbouring sheets are separated by a distance $Na_0(2/\sqrt{3})$, where a_0 is the C–C bond length, (see (5) below). Examples of results available in the literature with which we can compare the quality of the Kurokawa empirical pseudopotentials are the qualitative results by Ajiki and Ando [57], by Reich [58] for *ab initio* results, and by Khoshnevisan [59] for graphene using the ‘Quantum Espresso’ *ab initio* DFT/local-density-approximation (LDA) method [60].

The real-space structure of graphene can be described by a two-atom 2D unit cell with basis vectors [57]:

$$\begin{aligned} \mathbf{a}_1 &= \frac{a_0\sqrt{3}}{2} (1, \sqrt{3}, 0), \\ \mathbf{a}_2 &= \frac{a_0\sqrt{3}}{2} (-1, \sqrt{3}, 0), \\ \mathbf{a}_3 &= \frac{a_0\sqrt{3}}{2} (0, 0, N), \end{aligned} \quad (5)$$

where $a_0 \approx 0.142$ nm and N (=10 in the results presented below) is the separation between sheets along the z -axis. The coordinates of the two C atoms in the cell are:

$$\mathbf{r}_1 = a_0 (0, 1, 0), \quad \mathbf{r}_2 = a_0 (0, 2, 0), \quad (6)$$

while the basis vectors in reciprocal space are:

$$\begin{aligned} \mathbf{b}_1 &= \frac{4\pi}{3a_0} \left(\frac{\sqrt{3}}{2}, \frac{1}{2}, 0 \right), \\ \mathbf{b}_2 &= \frac{4\pi}{3a_0} \left(-\frac{\sqrt{3}}{2}, \frac{1}{2}, 0 \right), \\ \mathbf{b}_3 &= \frac{4\pi}{3a_0} \left(0, 0, \frac{\sqrt{3}}{2N} \right). \end{aligned} \quad (7)$$

Figure 1 shows the basis geometry in real and k -space, as well as the band structure obtained using the Kurokawa empirical pseudopotentials and DFT calculations. Compared to the *ab initio* results shown here and reported in the literature [58, 59], the Kurokawa pseudopotentials exhibit the

'correct' behaviour of the $\pi-\pi^*$ band at energies close to the Fermi level and the correct band crossing (Dirac point) at the symmetry point K, but exhibit a set of bands at Γ at a lower energy and compress the $\pi-\pi^*$ band energetic separation near $k = 0$. The Fermi velocity at the Dirac point of $v_F \approx 9.5 \times 10^7 \text{ cm s}^{-1}$ is in good agreement with DFT results, but about 15% smaller than experimental data and GW-corrected values [61].

2.4. Graphene nanoribbons

In armchair-edge graphene nanoribbons (AGNRs) quantum confinement causes the opening of a gap. However, this feature, required from a practical perspective, exhibits a qualitative behaviour significantly different from the more customary particle-in-a-box situation in which the zero-point energy (and so the gap) increases monotonically with increasing confinement. Instead, one observes the emergence of three families of AGNRs characterized by the number of atomic layers N_a along the width of the AGNR (see figure 2), the energy gap oscillating as N_a takes the values $3p$, $3p + 1$, or $3p + 2$, where p is an integer. This 'peculiar' behaviour is due to the spatial distribution of the Clar resonance structures (i.e., Clar sextets) [62]. This is a well-characterized effect in the chemistry community, most notably for explaining the behaviour of poly-aromatic hydrocarbons [63], and it has been recognized by Ezawa [64, 65] in the electronics community. We shall refer to this property as the 'claromatic' behaviour (or 'claromaticity') of AGNRs [66].

In simple terms, in aromatic compounds C atoms are bonded with sp^2 -coordination, the remaining (p_z) bonds forming the π band. However, one alternative possible way to visualize the formation of the π band is to consider these bonds resonating among different C atoms, as in a benzene ring. In graphene and AGNRs we can draw the hexagonal lattice and connect neighbour C atoms with double bonds when possible. In so doing, we obtain a structure in which some of the hexagonal rings will have three double-bonded C atoms. These rings are labelled 'Clar sextets'. Note that the presence of two adjacent Clar sextets is not allowed, as this would imply the presence of C atoms with five bonds. In graphene, clearly there is no unique configuration (pattern) of Clar sextets: we can consider many equivalent patterns, the structure resonating among all of these possible patterns, thus forming the π band. Each possible configuration of Clar sextets is called a 'Kékule pattern'. In AGNRs, when the edge bonds are terminated by a single H atom, the edge rings will be necessarily Clar sextets because the terminating H atoms force single edge bonds. This will happen at both edges. Therefore, depending on the number of atomic lines along the width of the ribbon, we may have three possible cases: (1) two possible resonating Kékule patterns exist. The π -electrons will be localized along the edges with a resonant path in the centre region of the ribbon that will contribute to the stability of the structure, thus giving rise to a large gap/ionization energy. (2) Only one resonant Kékule pattern is possible. The π -electrons are localized, yielding an intermediate gap. (3) Many possible Kékule patterns can

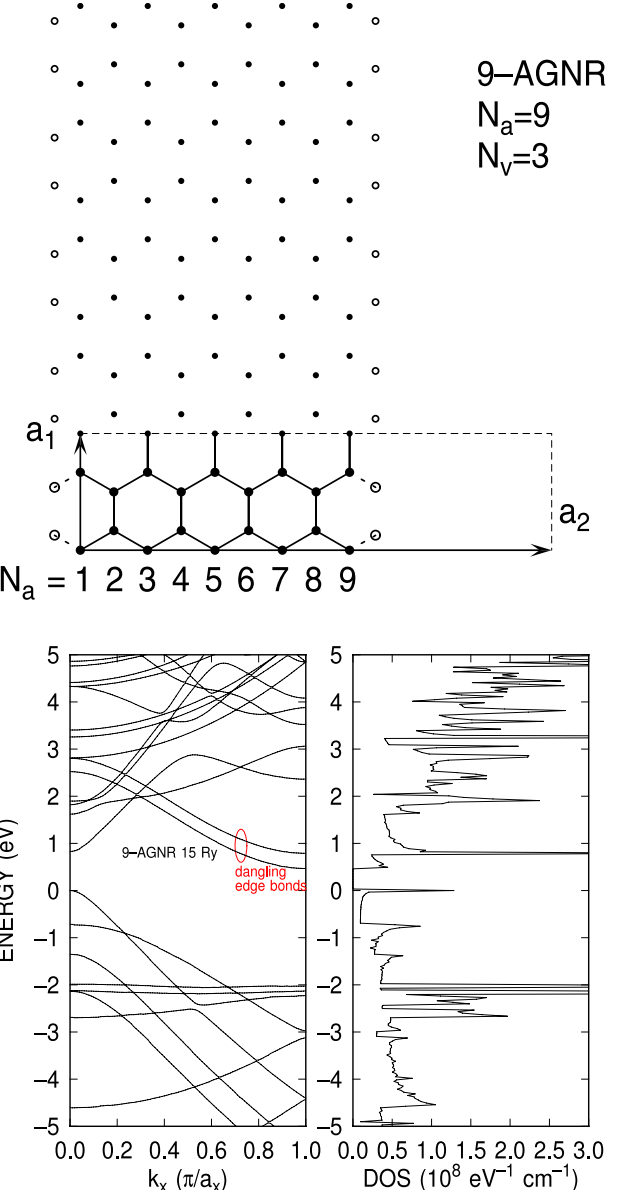


Figure 2. Top: projection on the (x, y) plane of the supercell used to treat an $N_a = 9$ armchair-edges graphene nanoribbon. The dashed lines define the supercell—including the three vacuum 'cells' separating adjacent ribbons—while the thick dots show the C atoms in the supercell, the thinner dots simply show the periodically replicated structure of the ribbon. Hydrogen terminations are shown as circles. A distance of $4\sqrt{3}a_0$ between planes has been assumed in the calculations by defining a primitive translation vector of such a length along the direction perpendicular to the plane of the ribbon. Bottom: Band structure and density of states for the bare-edge 9-AGNR illustrated in the top frame, obtained using the Kurokawa local empirical pseudopotentials. Note the bands associated with edge-states resulting from the edge-C dangling bonds. Here, and in the following, graphene ribbons are separated by $N_v\sqrt{3}a_0$, with $N_v = 4$ (unlike the choice of $N_v = 3$ made to sketch the ribbon in the left panel of this figure), along the plane of the ribbon, and by $N_y\sqrt{3}a_0$, with $N_y = 3$, along the direction perpendicular to the sheets. The energy has been set to zero at the top of the valence band. The quantity $a_x = 3a_0$, where a_0 is the C–C bond length, indicates the size of the unit cell along the axial direction of the ribbon.

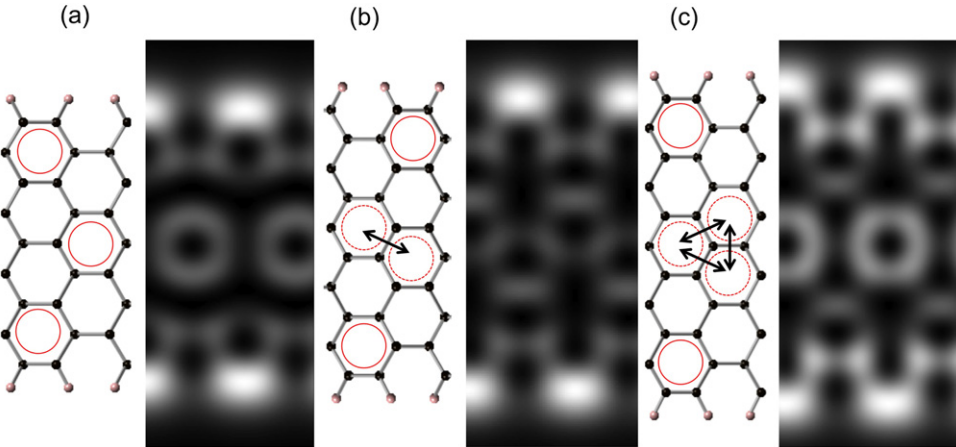


Figure 3. DFT computed STM images for the three classes of AGNRs. The first class (a) $N_a = 3p$ (9-AGNR) has a single unique Kékule pattern with Clar sextets denoted with the solid circles; the second class (b) $N_a = 3p + 1$ (10-AGNR) has two possible Kékule patterns formed by two Clar sextets denoted with dashed red circles. The arrows indicate the resonating behaviour. Finally, the third class (c) $N_a = 3p + 2$ (11-AGNR) exhibits many Kékule patterns formed by the many Clar sextets (dashed red circles).

be formed. The π -electrons are mainly delocalized except at the edges of the ribbon, leading to a small gap. These three different possibilities occur respectively for ribbons with widths given by a number of atomic lines $N_a = 3p + 1$ (two Kékule pattern), $N_a = 3p$ (one Kékule patterns), and $N_a = 3p + 2$ (many Kékule patterns), giving rise to the bandgap scaling $E_{g,3p+1} > E_{g,3p} > E_{g,3p+2}$. If we terminate the edges with, say, H_2 instead, the opposite will happen, since the edge rings will be prevented from being Clar sextets by the double terminating edge bonds and the appearance of Kékule patterns (claromaticity) as a function of ribbon width will be different. We note parenthetically that this behaviour is absent in zigzag-edge GNRs (ZGNRs). Also, the lack of a gap in these structures makes them less interesting for nanoelectronics applications; as a consequence electron transport in ZGNRs has not been studied as extensively as in AGNRs and we shall ignore them here. Nevertheless, a discussion of their LEP-based band structure is given in [53].

The Kékule patterns can be visualized through computationally generated scanning tunnelling microscope (STM) images using the wavefunctions (which can be obtained from DFT or EP) through the Tersoff–Hamann approximation [67, 68] of the current:

$$I(x, y, z, U) = \sum_n |\Psi_n(x, y, z)|^2 \times [f(E_F - E_n) - f(E_F + eU - E_n)], \quad (8)$$

where E_F is the Fermi energy, U is the applied potential, and E_n is the energy in band n corresponding to the wavefunction Ψ_n . A plot of the calculated STM images from DFT simulations using the ‘Vienna *ab initio* simulation package’ (VASP) [69–72] is shown in figure 3 for $N_a = 9, 10$ and 11 AGNRs. These VASP simulations have been performed using the projector-augmented wave method (PAW). Exchange–correlation is represented with the revised Perdew–Burke–Ernzerhof (PBE) model of the generalized gradient approximation (GGA). A plane-wave cutoff of

550 eV was applied with a Γ -centred Monkhorst–Pack mesh of $11 \times 1 \times 1$ in k -space. A Methfessel–Paxton Gaussian smearing of order 1 with a width of 0.05 was used to accelerate convergence. Geometric optimization was performed with the conjugate-gradient algorithm until the absolute value of the forces was less than $0.3 \text{ eV } \text{\AA}^{-1}$. Optimization of the graphene unit cell resulted in a C–C bond length of 1.426 \AA . The wavefunctions are sampled at a distance $z = 0.2 \text{ nm}$ above the AGNRs and a value of $eU = -0.5 \text{ eV}$ (which captures the highest two valence bands) was chosen for the applied potential energy.

In comparison, empirical tight binding (ETB) calculations [64, 65, 73] and calculations based on the Weyl (massless Dirac) equation [74, 75] have found a different width-dependence compared to DFT and EP, and predict $E_{g,3p} \approx E_{g,3p+2} > E_{g,3p+1} = 0$, so $3p + 2$ GNRs are predicted to be semimetallic. This is due to the inability of nearest-neighbours-only models to capture the basic physics of the resonant Clar structures, as noted by Zhao *et al* [76]. In contrast, *ab initio* DFT (LDA and with GW corrections) calculations [77–79] also predict $E_{g,3p+1} \geq E_{g,3p} > E_{g,3p+2} \neq 0$, which implies that all AGNRs are semiconducting. This reveals a major shortcoming of ETB (in its nearest-neighbour implementation) compared to *ab initio* results. While Son *et al* [77] have emphasized the importance of the relaxation of the edge C–C bonds, we find that this is a secondary contribution to the width-dependence of the AGNR bandgap. Indeed we find the same *ab initio* behaviour ourselves even without accounting for this effect. Note also that the value of the calculated bandgap increases dramatically when performing GW calculations (compare the results of [77] with those of [79], for example).

In our EP-based simulations of AGNRs, we employ a supercell with its axial direction along the x -axis, width along the y -axis and out-of-plane direction along the z -axis. Thus,

the primitive translation vectors in real space are:

$$\begin{aligned}\mathbf{a}_1 &= (3a_0, 0, 0), \\ \mathbf{a}_2 &= (0, (N_c + N_v)\sqrt{3}a_0, 0), \\ \mathbf{a}_3 &= (0, 0, N_z\sqrt{3}a_0),\end{aligned}\quad (9)$$

where N_c is the number of cells between the edges (i.e., along the y direction). This is related to the width parameter of the ribbon [77], N_a , via $N_a = 2N_c$ (for even N_a) or $N_a = 2N_c + 1$ (for odd N_a). N_v is the number of cells separating the ribbons along the y (width) direction, and N_z is the number of cells of extension $\sqrt{3}a_0$ separating the planes on which adjacent ribbons lie (in the vertical z direction). All results presented below have been obtained using $N_v = 4$ and $N_z = 3$. In each supercell there will be $4N_c + 2$ (odd N_a) or $4N_c$ (even N_a) atoms. The four atoms in the cell adjacent to the ‘left’ edge (i.e., the edge at the smallest value of y) will have coordinates:

$$\begin{aligned}\mathbf{\tau}_1 &= (0, 0, 0), & \mathbf{\tau}_2 &= a_0 \left(\frac{1}{2}, \frac{\sqrt{3}}{2}, 0 \right), \\ \mathbf{\tau}_3 &= a_0 \left(\frac{3}{2}, \frac{\sqrt{3}}{2}, 0 \right), & \mathbf{\tau}_4 &= a_0 (2, 0, 0).\end{aligned}\quad (10)$$

The remaining atom coordinates will be given by replicating these coordinates $N_c - 1$ times by translating them by an amount $l\sqrt{3}a_0$ (with $l = 1, N_c - 1$) along the positive y direction:

$$\begin{aligned}\mathbf{\tau}_{4l+1} &= \mathbf{\tau}_1 + l\sqrt{3}a_0\hat{\mathbf{y}}, & \mathbf{\tau}_{4l+2} &= \mathbf{\tau}_2 + l\sqrt{3}a_0\hat{\mathbf{y}}, \\ \mathbf{\tau}_{4l+3} &= \mathbf{\tau}_3 + l\sqrt{3}a_0\hat{\mathbf{y}}, & \mathbf{\tau}_{4l+4} &= \mathbf{\tau}_4 + l\sqrt{3}a_0\hat{\mathbf{y}},\end{aligned}\quad (11)$$

where $\hat{\mathbf{y}}$ is the unit vector along the y -axis. For odd N_a two more C atoms must be added at the ‘right’ edge (that is, the edge at the largest value of y) by translating atoms 1 and 4 in (10) by an amount $\sqrt{3}a_0N_c$:

$$\begin{aligned}\mathbf{\tau}_{4N_c+1} &= \mathbf{\tau}_1 + N_c\sqrt{3}a_0\hat{\mathbf{y}}, \\ \mathbf{\tau}_{4N_c+2} &= \mathbf{\tau}_4 + N_c\sqrt{3}a_0\hat{\mathbf{y}}.\end{aligned}\quad (12)$$

The dangling sp^2 (or σ) orbitals of the edge-C atoms can be saturated by adding H atoms along the direction of the missing C–C bonds, assuming a C–H bond length equal to that of methane (CH_4), 0.109 19 nm.

Figure 2 (bottom) shows the band structure of a bare-edge (as opposite to H-terminated) 9-AGNR. Figure 4 shows similar results for H-terminated 5- and 7-AGNRs. Note that the $k_x = 0$ energy gap obtained for the 5-AGNR (0.197 eV, unlike the zero gap predicted by ETB models based on only nearest-neighbours coupling via p_z -orbitals only) is much smaller than the gap obtained for the 7-AGNR (1.612 eV), as expected from the $E_{g,3p+1} > E_{g,3p} > E_{g,3p+2} \neq 0$ ordering predicted by first-principles approaches. Also, edge-states lower the gap [80] but disappear when the edge bonds are terminated with H using the pseudopotential parameters listed in table 1, as shown in figure 4. In all cases these gaps are in agreement with the first-principles, non-GW-corrected results of [77] and our DFT calculations, as shown in figure 5. Only for the smallest-width ribbon (3-AGNR) is the gap noticeably smaller than what is obtained from first-principles

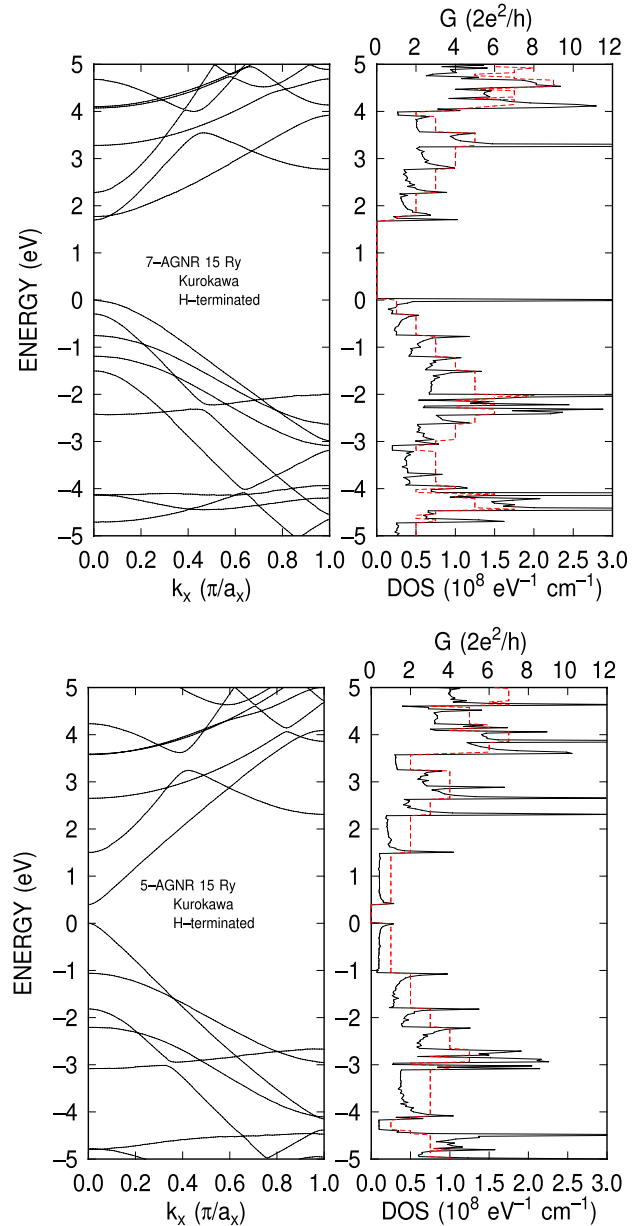


Figure 4. Band structure (left frames) and density of states (right frames, black solid line) and ballistic conductance (right frames, dashed red lines) for an $N_a = 7$ (top) and an $N_a = 5$ (bottom) H-terminated armchair-edge graphene nanoribbon. Note that while empirical tight-binding models based on nearest-neighbour-only coupling and on p_z -orbitals only predict a semimetallic (no gap) behaviour for the 5-AGNR, empirical pseudopotentials yield semiconducting behaviour even in the absence of the distortion of the edge C–C bonds found by first-principles calculations [77]. Note the absence of the edge-states bands thanks to the H termination of the edge bonds.

calculations, presumably because of the growing importance of edge-bond distortion noticed by Son *et al* [77]. The fact that experiments [81] have not confirmed this claromatic behaviour has been explained by Querlioz and co-workers on the grounds of disorder [82]. Tseng *et al* [83] have similarly argued that the clustering of the gap around values corresponding to the largest $3p + 1$ gap is the result of line-edge roughness (ER or LER) which allows electron

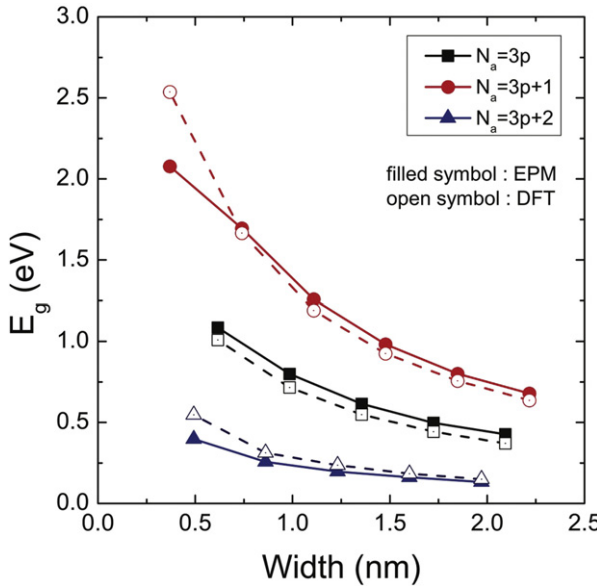


Figure 5. The three ladders of the bandgap at $k = 0$ as a function of ribbon width for armchair-edge graphene nanoribbons. The EP results (filled symbols) have been obtained using Kurokawa's pseudopotentials with H-terminated edge bonds and are in excellent qualitative agreement and good quantitative agreement with DFT GGA calculations shown here (DFT). The results are also in good agreement with the non-GW-corrected DFT + LDA calculation of Son *et al* [77]. GW corrections yield much larger gaps for the quasiparticle energy [79], while nearest-neighbour ETB models can predict qualitatively incorrect gaps and an incorrect ordering of the three ladders[77].

transmission only at the largest local gap. We shall see in section 4.2 how strongly LER and the claromatic properties of AGNRs may affect electron transport.

2.5. Ab initio thermodynamics

The claromatic properties of AGNRs we have just discussed depend crucially on how edge-atom bonds are terminated. And we have hinted at the importance of the claromatic behaviour in determining electron-transport properties. It is therefore of great interest to understand which terminations (H , H_2 or other functional groups) are most stable and/or most likely to be realized in practice. Since DFT is a ground-state theory and we are interested in room-temperature behaviour, additional insight is needed to study systems at finite temperature and pressure. Such insight can be provided by *ab initio* thermodynamics. The ultimate goal would be, of course, to find an edge-termination which could minimize the claromatic behaviour. Here we shall be less ambitious and simply illustrate the usefulness of *ab initio* thermodynamics considering the two cases of edge-bond termination with single H atoms and with H_2 . We show that, in practice, in addition to controlling the width of a ribbon, it may be very difficult to control even the type of edge-bond termination.

Ab initio thermodynamics can be used in conjunction with the ground-state calculations of DFT to estimate the relative stability of surfaces of different stoichiometry at finite temperatures and in the presence of gas-phase species.

Following the approach of Scheffler *et al* [84] for GNRs in chemical equilibrium with a gas-phase hydrogen reservoir, the edge free energy can be written as:

$$\gamma_{\text{edge}} = \frac{1}{2L} [G_{\text{GNR}+H} - N_C g_C - N_H \mu_H], \quad (13)$$

where L is the length of the ribbon, $G_{\text{GNR}+H}$ is the Gibbs free energy of the ribbon terminated with hydrogen, N_C and N_H are the number of carbon and hydrogen atoms respectively, g_C is the Gibbs free energy per formula unit of the graphene sheet, and μ_H is the chemical potential of the hydrogen defined as a function of temperature (T) and pressure (p):

$$\begin{aligned} \mu_H(T, p) &= \frac{1}{2} \mu_{H_2}(T, p) \\ &= \frac{1}{2} \left[E_{H_2} + E_{H_2}^{\text{ZPE}} + \mu_{H_2}(T, p^0) + k_B T \ln \left(\frac{p}{p^0} \right) \right]. \end{aligned} \quad (14)$$

In this equation E_{H_2} is the internal energy calculated with DFT, $E_{H_2}^{\text{ZPE}}$ the zero-point energy, and $\mu_{H_2}(T, p^0)$ is the chemical potential at $p^0 = 1$ atm and is computed with the gas-phase enthalpy and entropy from the NIST JANAF table [85]. The last term represents the contribution from the pressure of the surrounding gas-phase environment. The expression given by (13) can be further simplified by approximating the Gibbs free energy with the Helmholtz free energy, which has been shown to be reasonable for oxide surfaces at pressures below 100 atm [84]. Furthermore, the vibrational contribution to the energy due to the C–C bonds is assumed not to be significantly different between the ribbons and the graphene sheet—and therefore approximately cancels. The temperature dependence is included through the hydrogen atoms, although even this term will be relatively small for these systems [86]. Therefore the edge free energy can be written as

$$\gamma_{\text{edge}} = \frac{1}{2L} \left[E_{\text{GNR}+H} - N_C E_C - F_H^{\text{vib}} - \frac{N_H}{2} \mu_{H_2} \right]. \quad (15)$$

Within the harmonic approximation the vibrational contribution to the energy due to the hydrogen atoms can be written as:

$$F_H^{\text{vib}} = \frac{\hbar\omega}{2} + k_B T \ln \left(1 - e^{-\hbar\omega/k_B T} \right). \quad (16)$$

Figure 6 shows a plot of the edge free energy of a 7-AGNR terminated with a single hydrogen atom (sp^2 bonds of the edge carbon atoms) and with double hydrogen atoms (sp^3 bonds of the edge carbon atoms) as a function of the H_2 chemical potential. Also shown on the second axis is the partial pressure p_H of gas-phase H_2 at several values of the temperature. The edge free energy is found to be insensitive to the number of atoms along the width of the ribbon and does not show any claromatic dependence. As can be seen by the negative edge free energies, the hydrogen-terminated ribbons are more thermodynamically stable than a sheet of graphene for hydrogen concentrations greater than those that exist at ambient conditions ($\sim 5 \times 10^{-7}$ atm). Furthermore, the ribbons terminated with double hydrogen atoms are more thermodynamically stable than those with a single hydrogen, except at extremely low hydrogen partial pressures.

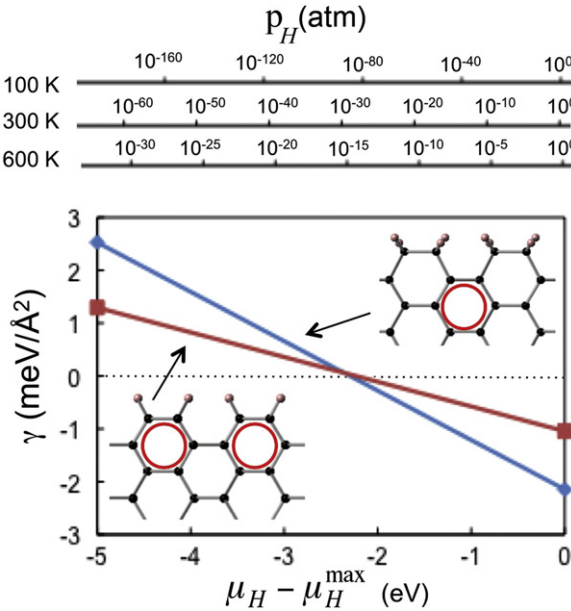


Figure 6. Calculated surface free energy versus hydrogen chemical potential for a 7-AGNR with the edges terminated with single hydrogen atoms (red line) and with two hydrogen atoms (blue line), using *ab initio* thermodynamics. The zero of the surface free energy corresponds to the energy of a graphene sheet. The top axis shows the corresponding hydrogen partial pressures p_H at three temperatures. Their very small values show that, in the presence of even minute amounts of hydrogen, H₂-terminated AGNRs are more stable. H-terminated AGNRs can be obtained only at very high temperatures and extremely small H partial pressures. The schematic diagrams show that the Clar sextets are either forced at the edges (H-terminated AGNRs) or away from them (H₂-terminated AGNRs).

These results are consistent with the studies of single and double hydrogen passivation of ribbons found in [86, 87]. Lu *et al* [87] also looked at the edge free energy of ribbons passivated with varying ratios of single and double hydrogen atoms and found that for a high hydrogen chemical potential the structures with all sp^3 bonds of the edge carbon atoms are the most stable. For the AGNRs terminated with double hydrogen atoms, the carbon atoms at the edges can no longer support a Clar resonance, since they are already sp^3 bonded. This changes the Kékule patterns that arise in the ribbons and a different trend in the bandgap is observed as a function of ribbon width (figure 7), given by $E_{g,3p} > E_{g,3p+2} > E_{g,3p+1}$. It is possible to modify the expression of the edge free energy of the ribbons to compute the thermodynamic stability of other functional groups terminating the edges, which in turn can influence the electronic structure. The interested reader is referred to current work in the literature [88, 89]. As a partial conclusion of this brief discussion, the sensitivity of the final configuration (H or H₂ termination) on processing temperature and pressure shows that the practical realization of a uniform type of termination may be difficult to achieve. Therefore, electronic transport in AGNRs may be sensitive not only to the edge roughness (see section 4.2), but also to the thermodynamical processing conditions.

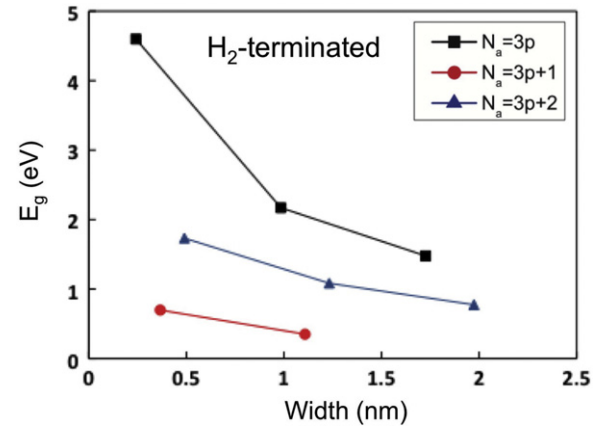


Figure 7. Bandgap versus width for AGNRs terminated with two hydrogen atoms computed with DFT. Note the different claromatic dependence compared to AGNRs terminated with single hydrogen atoms, shown in figure 5.

2.6. Phonon spectra in graphene

Electron–phonon scattering constitutes an unavoidable intrinsic limitation to charge carrier transport in solids and an accurate description of the phonon dispersion and polarization vectors is a basic ingredient required to calculate the strength of these processes. In analogy with the empirical and *ab initio* treatment of the electronic dispersion we have discussed in section 2.5, here we shall present two methods to deal with this issue: the empirical Born–von Kármán model and a more sophisticated model based on DFT perturbation theory. A comparison between the two methods will also help us understand the basic physical elements involved.

At an empirical level, the calculation of the phonon dispersion relation for bulk graphene that we use follows closely the methodology set forth in the book by Saito *et al* [90], which followed that of Al-Jishi and Dresselhaus [91]. Within the Born–Oppenheimer approximation, the dispersion relation is calculated using the Born–von Kármán model for lattice dynamics in the harmonic approximation [92].

The equation of motion for ion γ in cell l moving in the i th direction can be written as:

$$\begin{aligned} F_i^{l\gamma} &= M_\gamma \ddot{\Delta}_{l,\gamma,i} \\ &= -\frac{\partial V}{\partial \Delta_{l,\gamma,i}} \\ &= -\sum_{l',\gamma',j} K_{i,j}(l\gamma; l'\gamma') \Delta_{l',\gamma',j}, \end{aligned} \quad (17)$$

where $\Delta_{l,\gamma,i}$ and $\ddot{\Delta}_{l,\gamma,i}$ are the ion's displacement and acceleration, respectively, V is the potential and $K_{i,j}$ is the atomic force constant. Expanding the potential and retaining only the second-order term (the zeroth-order term is constant and the first-order term is the total force on the atom and so vanishes at equilibrium):

$$V(\mathbf{r}) \approx \frac{1}{2} \sum_{l\gamma} \sum_{l'\gamma'} \nabla_\Delta^2 V(\mathbf{r} - \mathbf{r}_l - \mathbf{r}_{l'} - \mathbf{r}_{\gamma'} - \mathbf{r}_{\gamma'}) \Delta_{l,\gamma} \Delta_{l',\gamma'}, \quad (18)$$

where τ_γ is the coordinate of ion γ , \mathbf{r}_l the coordinate of the cell, and ∇_Δ denotes the differentiation with respect to the displacement within the gradient. The atomic force constant in the i th direction of ion γ in unit cell l due to a displacement in the j th direction of ion γ' in cell l' is:

$$K_{i,j}(l\gamma; l'\gamma') = \frac{\partial^2 V}{\partial \Delta_{l,\gamma,i} \partial \Delta_{l',\gamma',j}} \Big|_0, \quad (19)$$

where the ‘0’ means that this quantity is evaluated at the equilibrium positions of the ions. The Fourier transformed (or ‘modified’ [92]) dynamical matrix is defined as:

$$D_{i,j}(\gamma\gamma'; \mathbf{q}) = (M_\gamma M_{\gamma'})^{-1/2} \sum_{l'} K_{i,j}(l\gamma; l'\gamma') \times \exp\{-i\mathbf{q} \cdot [\mathbf{r}_l + \tau_\gamma - \mathbf{r}_{l'} - \tau_{\gamma'}]\}. \quad (20)$$

Note that this matrix does not depend on l thanks to the symmetry of the lattice. The dynamical matrix can then be used to solve the sixth degree secular equation:

$$|D_{i,j}(\gamma'\gamma; \mathbf{q}) - \omega^2(\mathbf{q})\delta_{\gamma\gamma'}\delta_{i,j}| = 0, \quad (21)$$

for ω , the normal mode frequencies, where the force-constants are taken from Zimmerman *et al* [93], and only fourth-nearest-neighbours atoms are considered [94]. Since the basis of the unit cell of graphene contains two atoms, there are six polarizations (labelled by the index η in the following) for each wavevector \mathbf{k} . Three of the modes are acoustic, for which $\omega \rightarrow 0$ as $\mathbf{q} \rightarrow 0$, and three optical; two of each of these branch types are transverse (T), two are longitudinal (L), and two more are ‘out-of-plane’ or ‘flexural’ modes (Z). Note that although we have employed a 3-vector \mathbf{q} , the dynamical matrix $D_{i,j}(\gamma\gamma'; \mathbf{q})$ depends only on the in-plane components \mathbf{Q} of the phonon wavevector, since in (20) all coordinates in the argument of the exponential have vanishing z components. Therefore in the following we shall label $\omega_{Q,\eta}$ the dispersion of branch η .

The computed phonon dispersion using the Born–von Kármán model is shown in figure 8, and also shown for comparison is the phonon dispersion calculated with the second method mentioned above, namely density functional perturbation theory (DFPT) [95] using the Quantum Espresso package [60]. As can be seen in the figure, the primary difference between these methods is a dip in the highest energy optical modes at the Γ -point [96] seen in the DFPT dispersion. This corresponds to the Kohn anomaly [96–99] due to the dielectric screening of the ion–ion interactions caused by electrons excited by the phonon from the valence to the conduction band via an intravalley excitation. The other known Kohn anomaly, located at the K-point and due to a similar screening effect but assisted by an $K-K'$ intervalley process assisted by an A'_1 K-phonon, is not resolved in these DFPT results, but has been reported by Piscanec *et al* [96]. Lazzeri *et al* [98] have emphasized the need to employ GW corrections beyond the GGA-corrected LDA to capture correctly this Kohn anomaly.

It should be noted that the identification of the modes (longitudinal or transverse, acoustic or optical) is correct only in the neighbourhood of the Γ -point. As we move away

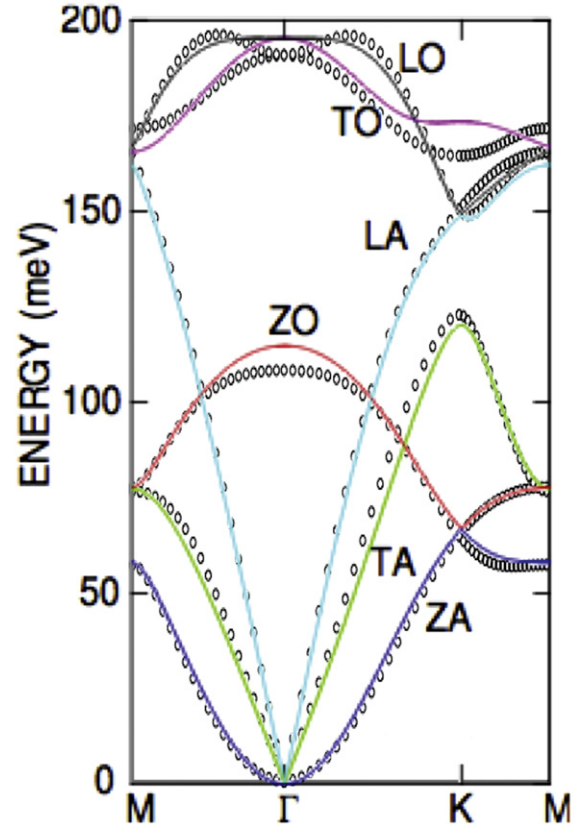


Figure 8. The phonon dispersion used here, calculated using a fourth-nearest-neighbours Born–von Kármán model (solid lines) compared with phonons calculated with the DFPT method implemented with Quantum Espresso (open circles).

from the centre of the first Brillouin zone (BZ), transverse and longitudinal modes cannot be unambiguously separated from a physical perspective (although they may be tracked continuously mathematically). Although this identification is irrelevant from a numerical perspective (the results we will present below do not depend on how we label each particular excitation associated with a particular matrix element and energy), a deeper physical understanding certainly benefits from it. We have labelled ‘transverse’ modes with a smaller value of the dot-product $|\mathbf{e}_{Q,\eta}^\gamma \cdot \mathbf{Q}|$, and ‘longitudinal’ those with a larger dot-product. Similarly, having identified transverse and longitudinal modes, towards the zone-edge we have labelled ‘acoustic’ the lower energy modes. A significant ambiguity remains in separating LA, TO, and LO modes in the zone-edge region along the K–M line.

3. Electron transport in graphene

In this section we shall deal with the intrinsic limits of electron transport in graphene. As mentioned before, we shall consider only single-layer graphene. Also, in order to limit the length of our already extensive discussion, we shall concentrate on steady-state phonon-limited transport, ignoring high-frequency properties, despite their practical interest, and deferring a partial discussion of extrinsic effects (interactions with the substrate, impurity, defects, etc) to later sections.

The main interest in the intrinsic properties of electron transport in graphene finds its origin in the fact that it is still unclear whether improved transport characteristics can be obtained with better control of the quality of the material. Indeed, while the highest electron mobility reported so far is about $200\,000 \text{ cm}^2 \text{ V}^{-1} \text{ s}^{-1}$ [100, 101], electron–electron interactions have been claimed to be able to boost this value by about a factor of three (the Fermi velocity renormalized by many-body Coulomb effects being predicted to be as high as $3 \times 10^8 \text{ cm s}^{-1}$ [102]), values as high as $500\,000 \text{ cm}^2 \text{ V}^{-1} \text{ s}^{-1}$ have been inferred from experiments [103] and, finally, ‘colossal’ values, perhaps exceeding $10^6 \text{ cm}^2 \text{ V}^{-1} \text{ s}^{-1}$, have been suggested from DFT calculations [9]. Clearly, only a direct knowledge of the intrinsic electron–phonon coupling constants coupled to transport calculations can settle the issue. Here we shall briefly review the status of our knowledge and discuss some results obtained by employing empirical pseudopotentials, the rigid-ion approximation, and Monte Carlo simulations to assess where we stand. Admittedly, we cannot provide a final answer, but only a plausible picture.

Let us start with the simplest picture as is often done in the literature. At this simplest level, an analytic approximation to the band structure of graphene near the Dirac point is adopted. Therefore the electron energy dispersion is described by a linear form $E(\mathbf{K}) \approx \hbar v_F K$. The electron–phonon scattering rates are calculated using Fermi’s golden rule and the deformation-potential approximation [104] employing empirical acoustic, Δ_{ac} , and optical, Δ_{op} , deformation potentials. Finally, the Boltzmann transport equation is solved in its linearized form to extract the low-field mobility, or in its full form (usually employing Monte Carlo simulations) to obtain the high-field velocity–field characteristics. In such a picture the scattering rate with acoustic phonons is simplified by assuming scattering with the longitudinal modes only, so that the scattering rate for an electron in the lowest energy conduction band near the Dirac point is given by: [13, 17, 19–21]

$$\frac{1}{\tau_{\text{ac}}(\mathbf{K})} = \frac{k_B T \Delta_{\text{ac}}^2 E(\mathbf{K})}{\hbar^3 v_F^2 \rho_x v_l^2}, \quad (22)$$

where v_F is the Fermi velocity, v_l the longitudinal sound velocity ($\approx 2.1 \times 10^6 \text{ cm s}^{-1}$), ρ_x the graphene mass density ($7.6 \times 10^{-7} \text{ kg m}^{-2}$), and Δ_{ac} now plays the role of some ‘effective’ longitudinal acoustic deformation potential. Note that this equation expresses the scattering rate for both emission and absorption of acoustic phonons and it assumes elastic scattering and equipartition, assumptions which are valid at a temperature higher than the Bloch–Grüneisen temperature $T_{\text{BG}} = 2k_F v_l / k_B \approx 54\sqrt{n} \text{ K}$ (with n measured in units of 10^{12} cm^{-2}) [13]. By fitting the calculated mobility/velocity it is possible to extract a value for the acoustic deformation potential Δ_{ac} . Similarly, the scattering rate for electrons with optical phonons can be written as: [9, 13, 19–21]

$$\begin{aligned} \frac{1}{\tau_{\text{op}}(\mathbf{K})} &= \frac{\Delta_{\text{op}}^2}{\rho_x \omega_{\text{op}} \hbar^2 v_F^2} \\ &\times \{[E(\mathbf{K}) - \hbar \omega_{\text{op}}](N_{\text{op}} + 1) \Theta[E(\mathbf{K}) - \hbar \omega_{\text{op}}] \\ &+ [E(\mathbf{K}) + \hbar \omega_{\text{op}}]N_{\text{op}}\}, \end{aligned} \quad (23)$$

where $\Theta(x)$ is the Heavyside step function, ω_{op} the frequency of the optical phonons, N_{op} their Bose–Einstein population, and Δ_{op} the optical deformation potential. A similar expression holds for intervalley processes:

$$\begin{aligned} \frac{1}{\tau_{\text{iv}}(\mathbf{K})} &= \frac{g_{\text{iv}} \Delta_{\text{iv}}^2}{\rho_x \omega_{\text{iv}} \hbar^2 v_F^2} \\ &\times \{[E(\mathbf{K}) - \hbar \omega_{\text{iv}}](N_{\text{iv}} + 1) \Theta[E(\mathbf{K}) - \hbar \omega_{\text{iv}}] \\ &+ [E(\mathbf{K}) + \hbar \omega_{\text{iv}}]N_{\text{iv}}\}, \end{aligned} \quad (24)$$

where all symbols with subscript ‘iv’ have the same meaning as in (23), but are referred to intervalley phonons, and g_{iv} is the degeneracy of the final valleys. Similar expressions (albeit written in a different but equivalent form) have been given also by Akturk and Goldsman [16].

The problems preventing us from finding a consensus on the values of Δ_{ac} , Δ_{op} , and Δ_{iv} are due to several causes. First, the expressions given above lump transverse and longitudinal modes into a single ‘effective’ mode. However, this may not constitute the major problem, since the role of TA and TO seems to be recognized almost unanimously as very small. Yet, some uncertainty remains. Second, intervalley scattering is either accounted for or ignored. Again, this is a small concern, intervalley scattering being recognized as relatively weak because of the small overlap between electronic states at significantly different energies (the phonon energies being quite large) at the \mathbf{K} and \mathbf{K}' symmetry points. Third, often values obtained for one of the graphite-based structures (graphite, graphene, AGNR, or CNT) have been applied to another system, ignoring possible differences (as shown, for example, in the ‘pathological’ case of AGNRs in section 4.1 below). Fourth, different band structure models (mainly ETB [16, 22], but also DFT [9]) have been employed to fit theory to experiments. At the low electron energies that affect the electron mobility this should not be an issue (notwithstanding the electron–electron interactions discussed in [102]), but it may add to the uncertainty when dealing with high-field transport. Finally, and most importantly, (22) has been used in slightly but significantly different versions, depending on whether the squared overlap factor between initial and final electron states has been treated ‘exactly’ (as in full-band models [9, 22]), approximately [13], or ignored altogether [16]. In an approximate way, this squared overlap factor is often treated by including a factor of the form $(1 + \cos \theta)/2$ (where θ is the scattering angle) within the angular integral required to reach (22). This results in an expression twice as small [13]. As just mentioned, slightly more complicated expressions have been employed when accounting for the full-band overlap factors. For example, Sule and Knezevic [22] write:

$$\frac{1}{\tau_{\text{ac}}(\mathbf{K})} = \frac{k_B T \Delta_{\text{ac}}^2 K}{2\pi \hbar^2 v_F \rho_x v_l^2} \int_0^{2\pi} d\theta |I(\mathbf{K}, \mathbf{K}')|^2, \quad (25)$$

where $K' = K$, and:

$$\begin{aligned} \frac{1}{\tau_{\text{op}}(\mathbf{K})} &= \frac{\Delta_{\text{op}}^2}{4\pi \hbar v_F \rho_x \omega_{\text{op}}} \left(N_{\text{op}} + \frac{1}{2} \mp \frac{1}{2} \right) \\ &\times \left(K \mp \frac{\omega_{\text{op}}}{v_F} \right) \int_0^{2\pi} d\theta |I(\mathbf{K}, \mathbf{K}')|^2, \end{aligned} \quad (26)$$

where $K' = K \mp \omega_{\text{op}}/v_F$. In these expressions the factor $I(\mathbf{K}, \mathbf{K}')$ is the overlap of the periodic part of the initial and final Bloch functions:

$$I(\mathbf{K}, \mathbf{K}') = \int d\mathbf{r} u_{\mathbf{K}'}^*(\mathbf{r}) u_{\mathbf{K}}(\mathbf{r}), \quad (27)$$

where the functions $u_{\mathbf{K}}(\mathbf{r})$ are normalized to the cell volume. Sule and Knezevic [22] employ a tight-binding model to evaluate the overlap integral but, of course, different models chosen to treat the overlap factor yield different values for the fitted deformation potentials.

In addition to this ‘overlap-factor confusion’, a ‘momentum-relaxation-versus-scattering rate’ issue confuses the matter even more. Indeed, another factor of $1/2$ was obtained by Hwang and Das Sarma [13] when considering the momentum relaxation rate (required when computing the electron mobility, but not required when directly solving the Boltzmann equation), since the angular integral now contains the integrand [13, 14, 105] $(1 - \cos \theta)(1 + \cos \theta)/2 = (1 - \cos^2 \theta)/2$. This expression for the *momentum relaxation rate* has been employed by Borysenko *et al* [9] to fit their DFT-calculated *scattering rates* to (22), so that in extracting the effective Δ_{ac} they presumably introduced an additional factor of $\sqrt{2}$ in their final fitted value. Finally, Shishir *et al* [20, 21], employ an expression similar to (22), but with a factor of four in the numerator ((4) in [20] or (14) in [21]) due to an alleged spin and valley degeneracy of final states.

This situation, which results in a wide range of values that have been claimed to fit experimental data, is not too surprising considering the long-standing controversy regarding measured and calculated deformation potentials in graphene [106]. Widening for now our discussion to graphite-based systems, such as graphene, graphite, AGNRs, and CNTs, a value of Δ_{ac} of about 20 eV has been used by Suzuura *et al* [107], a value close to the equally large values of 19 eV [13, 43], 16.5 eV used by Shishir *et al* [20], or 16 eV, chosen by Fang and co-workers [23], by Betti *et al* [25] and by Bresciani *et al* [108] for AGNRs on the basis of work by Finkenstadt and co-workers [109] and on even much earlier publications on graphite [110, 111]. An even larger value of 29 eV has been employed for single-layer graphene by Bolotin *et al* [100], while, on the opposite side, a much smaller value of 4.5 eV has been adopted by Betti *et al* in a later publication also on AGNRs by the same group [26]. Other common intermediate values found in the literature are 7.4 eV [112], as calculated for CNTs from the Su–Schrieffer–Heeger model [113, 114]; 12 eV, employed by Vasko *et al* [115] and by Sule and Knezevic [22]; and 9 eV, as chosen by Pennington and Goldsman for CNTs [116], Akturk and Goldsman [16], and by Stauber and co-workers [117]. Also, Shishir and co-workers have employed a very small value of 4.75 eV in one of their publications [21], but this is actually equivalent to 9 eV ($4.75 \sqrt{4}$)—or even 12.7 eV ($4.75 \sqrt{8}$) when accounting for overlap-factor effects—in light of the discussion above. Finally, values ranging from 6.9 eV (for 100% H) to 20.84 eV (100% F) have been obtained from DFT for chemically modified graphene [15], depending on the chemical modification (H, F, or I). The

DFT work by Borysenko *et al* [9] yields an extremely small value of $4.5/\sqrt{2} \approx 3.2$ eV (when correcting for the additional factor of two included in the denominator of their fitting expression). Such a small value may be the result of the ‘deformable-ion’ static screening implicitly included in these calculations based on perturbation theory DFT, as discussed below. In addition, DFT (LDA/GGA) calculations have been shown to underestimate the strength of the electron–phonon coupling around the K-symmetry point, at least for optical phonons [98].

Similarly, reported values for Δ_{op} vary from a high 5×10^9 eV cm $^{-1}$ [22] to 2.7×10^9 eV cm $^{-1}$ [108], to 1.4×10^9 eV cm $^{-1}$ [23], and to lower values of 10^9 eV cm $^{-1}$, adopted by Shishir *et al* [20]. From fits to their DFT results Borysenko and co-workers [9] have found that a value of 10^9 eV cm $^{-1}$ applies to intravalley transitions assisted by optical phonons, while a value of 3.5×10^8 eV cm $^{-1}$ has been found for K–K’ intervalley transitions assisted by acoustic phonons. In a few cases the separate contributions of longitudinal and transverse modes have been isolated, such as for the LO and TO optical deformation potentials of 6.7 and 9.6×10^8 eV cm $^{-1}$ (LO and TO, respectively) [118], or $\Delta_{\text{ac}} \approx 0.87, 3.87$ and 4.56 eV for various exchange and ‘modulated hopping’ processes, yielding an equivalent effective $\Delta_{\text{ac}} \sim 6$ eV [119]. Finally, Lazzeri *et al*, in the context of the Kohn anomaly, have employed GW-corrected DFT to extract values of 7.9×10^8 eV cm $^{-1}$ for K–K intravalley processes assisted by E_{2g} phonons and 1.39×10^9 eV cm $^{-1}$ for K–K’ intervalley processes assisted by A'_1 phonons [98]. However, these last values have been calculated only for transitions between symmetry points and they cannot be easily compared to the deformation potentials appearing in (23), which are averaged over larger regions of the BZ and are therefore less affected by selection rules [99].

In an attempt to clarify the issue (but probably ending up confusing it even more), we now present calculations based on the carbon empirical pseudopotentials used in the previous section [8] and the rigid-ion approximation⁴ to calculate the intrinsic electron–phonon scattering rates in single-layer graphene. The main conclusion we reach from these calculations is that scattering with acoustic phonons represents the dominant contribution, resulting in a large—but not ‘colossal’—300 K electron mobility of about $200\,000$ cm 2 V $^{-1}$ s $^{-1}$, reproducing satisfactorily the saturated velocity measured by Dorgan *et al* [121], and exhibiting also a region of negative differential mobility at high fields. These scattering rates lead to an extracted effective acoustic deformation potential Δ_{ac} (lumping LA and TA into a single process) of 18 eV in intrinsic graphene when fitting the numerical results to (22), decreasing to about 15 eV at densities of about 3×10^{12} cm $^{-2}$. These numbers increase by a factor of $\sqrt{2}$ —to 25 and 22 eV, respectively—if fitted to (22) with an extra factor of two in the denominator to account for overlap-factor effects. Similarly, a value of

⁴ This approximation and its implementation using empirical pseudopotentials have such a long history that it is appropriate to refer the reader to the long list of references cited by Fischetti and Higman [120].

$\Delta_{\text{op}} \approx 6 \times 10^8 \text{ eV cm}^{-1}$ can be derived by fitting the much smaller total intravalley optical-phonon scattering rate to (23). The extracted value of Δ_{op} also decreases by about 35% at densities of the order of $3 \times 10^{12} \text{ cm}^{-2}$. Finally, K–K' intervalley processes assisted by both acoustic and optical phonons are very weak as a result of a small overlap integral, in agreement with what was found by Sule and Knezevic [22] employing ETB. However, transitions from the K-point to the region around the M symmetry point are significant at high electron energies, as shown below, and they result in a high-field negative differential mobility.

3.1. Electron–phonon Hamiltonian

In order to compute the electron–phonon scattering rates from empirical pseudopotentials, we start by writing the electron–phonon perturbation Hamiltonian due to a phonon of mode (or branch) η as:

$$\hat{H}_{\text{ep}}^{(\eta)}(t) = \int d\mathbf{r} \rho(\mathbf{r}, t) \delta V^{(\eta)}(\mathbf{r}, t), \quad (28)$$

where ρ is the electron density and $\delta V^{(\eta)}$ is the change of the electron potential energy (lattice (pseudo) potential) due to the presence of phonons of branch η . In second quantization this expression takes the form:

$$\begin{aligned} \hat{H}_{\text{ep}}^{(\eta)}(t) &= \int d\mathbf{r} \hat{\Psi}^\dagger(\mathbf{r}, t) \hat{\delta V}^{(\eta)}(\mathbf{r}, t) \hat{\Psi}(\mathbf{r}, t) \\ &= \int d\mathbf{r} \hat{\mathcal{H}}_{\text{ep}}(\mathbf{r}, t), \end{aligned} \quad (29)$$

where $\hat{\Psi}(\mathbf{r}, t)$ is the electron field operator, $\hat{\delta V}^{(\eta)}(\mathbf{r}, t)$ should be now be regarded as an operator, and we have defined the Hamiltonian density as $\hat{\mathcal{H}}_{\text{ep}}(\mathbf{r}, t)$. The ‘hats’ over these quantities denote operators acting on Fock space. As usual, we expand the electron field operator over Bloch states $\psi_k^{(n)}(\mathbf{r}, t)$ of the crystal momentum $\hbar\mathbf{k}$ in band n as:

$$\hat{\Psi}(\mathbf{r}, t) = \sum_{\mathbf{k}, n} \hat{c}_k^{(n)} \psi_k^{(n)}(\mathbf{r}, t), \quad (30)$$

where $\hat{c}_k^{(n)}$ is the annihilation operator.

As a general rule, we use lower-case bold characters for 3-vectors and upper-case bold characters for 2-vectors on the (x, y) plane of the graphene sheet. The z -axis is along the direction perpendicular to the sheet. Exceptions to this rule are the vectors \mathbf{G} of the reciprocal lattice of the supercell (since this is a universal notation), so \mathbf{G}_{\parallel} will denote their projection on the plane of the sheet. Also we will use the upper-case Greek letter Δ for the ionic displacement, which, even here, is a 3-vector.

Using a supercell of volume Ω_c ($=\Omega_{2D} L_c$ ($= (3/2)\sqrt{3} a_0^2 L_c$, where L_c is the extension of the supercell along the direction z perpendicular to the graphene sheet) to describe the electronic excitations, the change of the lattice potential can be written as:

$$\hat{\delta V}^{(\eta)}(\mathbf{r}, t) = \frac{1}{N_c \Omega_c} \sum_{l, \gamma} \nabla V^{(\gamma)}(\mathbf{r} - \mathbf{r}_l - \boldsymbol{\tau}_\gamma) \cdot \hat{\Delta}_{l, \gamma}^{(\eta)}(t), \quad (31)$$

where, consistently with the notation employed in section 2.6, the index l labels the N_c 3D (super)cells, γ labels the ion in each cell, $\hat{\Delta}_{l, \gamma}^{(\eta)}$ is the displacement of ion γ in cell l due to the presence of a phonon of mode η , $V^{(\gamma)}$ is the pseudopotential of ion γ , $\mathbf{r}_l = (\mathbf{R}_l, z_l)$ is the coordinate of each (super)cell, and $\boldsymbol{\tau}_\gamma$ is the coordinate of ion γ in each cell. Using the Fourier decomposition for the ionic (pseudo) potential,

$$V^{(\gamma)} = \sum_{\mathbf{k}} V_{\mathbf{k}}^{(\gamma)} e^{i\mathbf{k} \cdot (\mathbf{r} - \mathbf{r}_l - \boldsymbol{\tau}_\gamma)}, \quad (32)$$

and the expression for the ionic displacement:

$$\begin{aligned} \hat{\Delta}_{l, \gamma}^{(\eta)}(t) &= \sum_{\mathbf{Q}} \left(\frac{\hbar}{2\rho_x \omega_{\mathbf{Q}, \eta}} \right)^{1/2} \mathbf{e}_{\mathbf{Q}, \eta}^{(\gamma)} e^{i(\mathbf{Q} \cdot \mathbf{R}_l - \omega_{\mathbf{Q}, \eta} t)} \\ &\times (\hat{b}_{\mathbf{Q}, \eta} + \hat{b}_{\mathbf{Q}, \eta}^\dagger), \end{aligned} \quad (33)$$

where ρ_x is the mass density (per unit area) of the crystal, $\omega_{\mathbf{Q}, \eta}$ the frequency of a phonon of branch η with 2D wavevector \mathbf{Q} , $\mathbf{e}_{\mathbf{Q}, \eta}^{(\gamma)}$ is its polarization, and $\hat{b}_{\mathbf{Q}, \eta}$ and $\hat{b}_{\mathbf{Q}, \eta}^\dagger$ its annihilation and creation operators, (31) can be written as:

$$\begin{aligned} \hat{\delta V}^{(\eta)}(\mathbf{r}, t) &= \frac{1}{N_c \Omega_c} \sum_{l, \gamma} \sum_{\mathbf{k}} i\mathbf{k} V_{\mathbf{k}}^{(\gamma)} e^{i\mathbf{k} \cdot (\mathbf{r} - \mathbf{r}_l - \boldsymbol{\tau}_\gamma)} \\ &\cdot \sum_{\mathbf{Q}} \mathbf{e}_{\mathbf{Q}, \eta}^{(\gamma)} \left(\frac{\hbar}{2\rho_x \omega_{\mathbf{Q}, \eta}} \right)^{1/2} e^{i(\mathbf{Q} \cdot \mathbf{R}_l - \omega_{\mathbf{Q}, \eta} t)} (\hat{b}_{\mathbf{Q}, \eta} + \hat{b}_{\mathbf{Q}, \eta}^\dagger). \end{aligned} \quad (34)$$

Observing that:

$$\frac{1}{N_c} \sum_{\mathbf{k}} \sum_l e^{i(\mathbf{Q} - \mathbf{k}_{\parallel}) \cdot \mathbf{R}_l} e^{i\kappa_z z_l} = \sum_{\mathbf{k}} \sum_{\mathbf{G}} \delta_{\mathbf{k}, \mathbf{q} + \mathbf{G}}, \quad (35)$$

having set $\mathbf{q} = (\mathbf{Q}, 0)$, and indicated with \mathbf{k}_{\parallel} the projection of \mathbf{k} on the (x, y) plane of the graphene sheet and with κ_z its out-of-plane component, the Hamiltonian density can be written as:

$$\begin{aligned} \hat{\mathcal{H}}_{\text{ep}}^{(\eta)}(\mathbf{r}, t) &= \sum_{n, n'} \sum_{\mathbf{k}, \mathbf{k}'} \sum_{\mathbf{Q}, \mathbf{G}} i(\mathbf{q} + \mathbf{G}) \\ &\cdot \sum_{\gamma} \mathbf{e}_{\mathbf{Q}, \eta}^{(\gamma)} \frac{1}{\Omega_c} V_{\mathbf{q} + \mathbf{G}}^{(\gamma)} e^{i\mathbf{G} \cdot \boldsymbol{\tau}_\gamma} \\ &\times \left(\frac{\hbar}{2\rho_x \omega_{\mathbf{Q}, \eta}} \right)^{1/2} e^{i(\mathbf{q} + \mathbf{G}) \cdot \mathbf{r}} \\ &\times e^{i\omega_{\mathbf{Q}, \eta} t} \psi_{\mathbf{K}'}^{(n')*}(\mathbf{r}, t) \psi_{\mathbf{K}}^{(n)}(\mathbf{r}, t) \hat{c}_{\mathbf{K}', n'}^\dagger (\hat{b}_{\mathbf{Q}, \eta} + \hat{b}_{\mathbf{Q}, \eta}^\dagger) \hat{c}_{\mathbf{K}, n}. \end{aligned} \quad (36)$$

Note that we have written $\hat{c}_{\mathbf{k}, n}$ as $\hat{c}_{\mathbf{K}, n}$ and $\psi_{\mathbf{K}}^{(n)}(\mathbf{r}, t)$ as $\psi_{\mathbf{K}}^{(n)}(\mathbf{r}, t)$, since at the energies of interest, all well below the vacuum level, the Bloch functions depend only on the in-plane components \mathbf{K} of the wavevector and we can consider only states with $k_z = 0$ without loss of generality. Note also that in (36) we have absorbed a phase factor $e^{i\mathbf{q} \cdot \boldsymbol{\tau}_\gamma}$ into the polarization vector $\mathbf{e}_{\mathbf{Q}, \eta}^{(\gamma)}$, as it follows from the definition of the dynamical matrix (20). Since $\boldsymbol{\tau}_\gamma$ is on the plane of the sheet ($z = 0$), for monatomic structures (so that $V^{(\gamma)}$ does not depend on γ) and absorbing the normalization to the cell

volume and the form factor inside $V^{(\gamma)}$ itself, we can rewrite this expression as:

$$\begin{aligned} \hat{\mathcal{H}}_{\text{ep}}^{(\eta)}(\mathbf{r}, t) = & \sum_{n,n'} \sum_{\mathbf{k}, \mathbf{k}'} \sum_{\mathbf{Q}, \mathbf{G}} i(\mathbf{q} + \mathbf{G}'') V_{\mathbf{q}+\mathbf{G}} \cdot \sum_{\gamma} \mathbf{e}_{\mathbf{Q}, \eta}^{(\gamma)} e^{i\mathbf{G}_\parallel \cdot \mathbf{r}_\gamma} \\ & \times \left(\frac{\hbar}{2\rho_x \omega_{\mathbf{Q}, \eta}} \right)^{1/2} e^{i(\mathbf{q} + \mathbf{G}) \cdot \mathbf{r}} e^{i\omega_{\mathbf{Q}, \eta} t} \\ & \times \psi_{\mathbf{K}'}^{(n')*}(\mathbf{r}, t) \psi_{\mathbf{K}}^{(n)}(\mathbf{r}, t) \hat{c}_{\mathbf{K}', n'}^\dagger (\hat{b}_{\mathbf{Q}, \eta}^\dagger + \hat{b}_{\mathbf{Q}, \eta}) \hat{c}_{\mathbf{K}, n}. \end{aligned} \quad (37)$$

Note that coupling between electrons and the out-of-plane modes ZA and ZO vanishes identically at first order. For these out-of-plane modes $\mathbf{e}_{\mathbf{Q}, \eta}^{(\gamma)}$ has a nonzero component only along z , so that $\mathbf{Q} \cdot \mathbf{e}_{\mathbf{Q}, \eta}^{(\gamma)} = 0$ and the terms involving the \mathbf{G} vectors will give a vanishing contribution when summed.

3.2. Electron–phonon matrix elements

The calculation of the matrix element, $\langle \mathbf{K}' n' | \hat{\mathcal{H}}_{\text{ep}}^{(\eta)} | \mathbf{K} n \rangle$, can be performed by employing the real-space form (36) of the Hamiltonian density and performing a real-space integration. In this case the only non-vanishing matrix elements will be:

$$\begin{aligned} \langle \mathbf{K}' n' | \hat{\mathcal{H}}_{\text{ep}}^{(\eta)} | \mathbf{K} n \rangle = & \sum_{\mathbf{G}} \mathcal{D}_{\mathbf{K}' - \mathbf{K}, \mathbf{G}}^{(\eta)} \\ & \times \int d\mathbf{r} \psi_{\mathbf{K}'}^{(n')*}(\mathbf{r}) e^{i(\mathbf{q} + \mathbf{G}) \cdot \mathbf{r}} \psi_{\mathbf{K}}^{(n)}(\mathbf{r}), \end{aligned} \quad (38)$$

where now $\mathbf{q} = (\mathbf{K}' - \mathbf{K}, 0)$. For simplicity, here and in the following, we shall not write explicitly the phonon states and operators that result in the Bose–Einstein occupation numbers when assuming phonons at thermal equilibrium. Using (37), the ‘deformation potential’ $\mathcal{D}_{\mathbf{Q}, \mathbf{G}}^{(\eta)}$ appearing above has been defined as:

$$\mathcal{D}_{\mathbf{Q}, \mathbf{G}}^{(\eta)} = i(\mathbf{q} + \mathbf{G}) \cdot \sum_{\gamma} \mathbf{e}_{\mathbf{Q}, \eta}^{(\gamma)} V_{\mathbf{q} + \mathbf{G}}^{(\gamma)} e^{i\mathbf{G} \cdot \mathbf{r}_\gamma} \mathcal{A}_{\mathbf{Q}, \eta}, \quad (39)$$

with

$$\mathcal{A}_{\mathbf{Q}, \eta}^2 = \left(\frac{\hbar}{2\rho_x \omega_{\mathbf{Q}, \eta}} \right) \left\{ \frac{N_{\mathbf{Q}, \eta}}{1 + N_{\mathbf{Q}, \eta}} \right\}. \quad (40)$$

In this expression $N_{\mathbf{Q}, \eta}$ is the occupation number of phonons of wavevector \mathbf{Q} and branch η and the upper (lower) symbol within curly bracket should be taken for absorption (emission) processes. Expressing the Bloch states using (2), (38) takes the form:

$$\begin{aligned} \langle \mathbf{K}' n' | \hat{\mathcal{H}}_{\text{ep}}^{(\eta)} | \mathbf{K} n \rangle = & \frac{1}{N_c \Omega_c} \sum_{\mathbf{G}' \mathbf{G}''} \sum_{\mathbf{q}} \mathcal{D}_{\mathbf{Q}, \mathbf{G}''}^{(\eta)} \\ & \times \int d\mathbf{R} e^{i(K - K' + \mathbf{G}_\parallel - \mathbf{G}'_\parallel + \mathbf{Q} + \mathbf{G}''_\parallel) \cdot \mathbf{R}} \\ & \times \int dz e^{i(G_z - G'_z + G''_z) z} u_{\mathbf{K}', \mathbf{G}'}^{(n')*} u_{\mathbf{K}, \mathbf{G}}^{(n)}. \end{aligned} \quad (41)$$

Performing the spatial integration this expression reduces to:

$$\langle \mathbf{K}' n' | \hat{\mathcal{H}}_{\text{ep}}^{(\eta)} | \mathbf{K} n \rangle = \sum_{\mathbf{G}, \mathbf{G}'} \mathcal{D}_{\mathbf{K}' - \mathbf{K}, \mathbf{G}' - \mathbf{G}}^{(\eta)} u_{\mathbf{K}', \mathbf{G}'}^{(n')*} u_{\mathbf{K}, \mathbf{G}}^{(n)}. \quad (42)$$

We can rewrite this expression as:

$$\langle \mathbf{K}' n' | \hat{\mathcal{H}}_{\text{ep}}^{(\eta)} | \mathbf{K} n \rangle = \sum_{\mathbf{G}, \mathbf{G}'} \mathcal{D}_{\mathbf{K}' - \mathbf{K}, \mathbf{G}'}^{(\eta)} u_{\mathbf{K}', \mathbf{G}'}^{(n')*} u_{\mathbf{K}, \mathbf{G}}^{(n)}, \quad (43)$$

a form in which the presence of \mathbf{G}' in the last term reminds us of *Umklapp* processes.

A commonly made simplification consists in considering only *Normal* processes, so that one can approximate (43) as:

$$\langle \mathbf{K}' n' | \hat{\mathcal{H}}_{\text{ep}}^{(\eta)} | \mathbf{K} n \rangle \approx \mathcal{D}_{\mathbf{K}' - \mathbf{K}, 0}^{(\eta)} \sum_{\mathbf{G}} u_{\mathbf{K}', \mathbf{G}}^{(n')*} u_{\mathbf{K}, \mathbf{G}}^{(n)}, \quad (44)$$

in which the first term plays the role of a deformation potential $\sim |\mathbf{K}' - \mathbf{K}| \Delta^{(\eta)}$ (expressed as $\Delta_{\text{ac}} Q$ in the notation of (22)) and the second term plays the role of a simple overlap integral between the ‘rigid ion wavefunctions’ in each cell (the term $I(\mathbf{K}, \mathbf{K}')$ in (25) above).

The double sum over \mathbf{G} vectors appearing in (43) is computationally troublesome, since their number is of the order of 10^3 -to- 10^4 , resulting in a sum of up to 10^8 terms per each pair of initial and final states. However, a reasonable approximation embraced here is based on the observation that the atomic pseudopotentials $V^{(\gamma)}(q)$ decay quickly with increasing q . Thus, only a few (relatively speaking!) terms will contribute to the sum in (43) and it is reasonable to consider only *Normal* in-plane processes by setting $\mathbf{G}_\parallel = 0$ in (43), but retaining the sum over G_z in the ‘deformation potential’ $\mathcal{D}_{\mathbf{K}' - \mathbf{K}, \mathbf{G}}^{(\eta)}$ appearing in (43):

$$\langle \mathbf{K}' n' | \hat{\mathcal{H}}_{\text{ep}}^{(\eta)} | \mathbf{K} n \rangle \approx \sum_{G_z} \mathcal{D}_{\mathbf{K}' - \mathbf{K}, G_\parallel = 0, G_z}^{(\eta)} \sum_{\mathbf{G}} u_{\mathbf{K}', \mathbf{G}}^{(n')*} u_{\mathbf{K}, \mathbf{G}}^{(n)}, \quad (45)$$

an approximation which we shall call ‘in-plane no-*Umklapp*’. As we have just remarked, this appears to be a reasonable approximation, certainly more accurate than (44), but we do not have any strong argument to quantify its accuracy beyond a few successful spot-check comparisons we have made for the matrix elements at selected \mathbf{K} , \mathbf{K}' , n , and n' obtained using the ‘exact’ but numerically intensive expression (43) and the approximate but more agile form (45). Figure 9 shows the matrix elements (screened as discussed below) between the wavevector \mathbf{K}_i at the symmetry-point K and wavevectors $\mathbf{K}_i + \mathbf{Q}$ as functions of the phonon wavevector \mathbf{Q} in the first BZ calculated using (45). The strong anisotropy indicates that wavefunction-overlap and phonon-polarization factors (controlled by symmetry considerations) and screening effects make it very difficult to define a single average deformation potential. Note that all intervalley transitions between the symmetry point K and \mathbf{K}' are relatively weak, while the largest matrix elements appear to be LA-processes connecting the symmetry point K to a region around the symmetry point M (the red region along the K–K’ line towards \mathbf{K}')—an observation that we shall discuss below. Note that throughout our analysis we have treated scattering with acoustic phonons as an inelastic process, and we have explicitly retained the exact (as opposite to the high- T limit) Bose occupation number for both optical and acoustic phonons. Therefore our study is in principle valid at temperatures both lower and higher than the Bloch–Grüneisen temperature. In practice, though, we shall consider the regime $T > T_{\text{BG}}$.

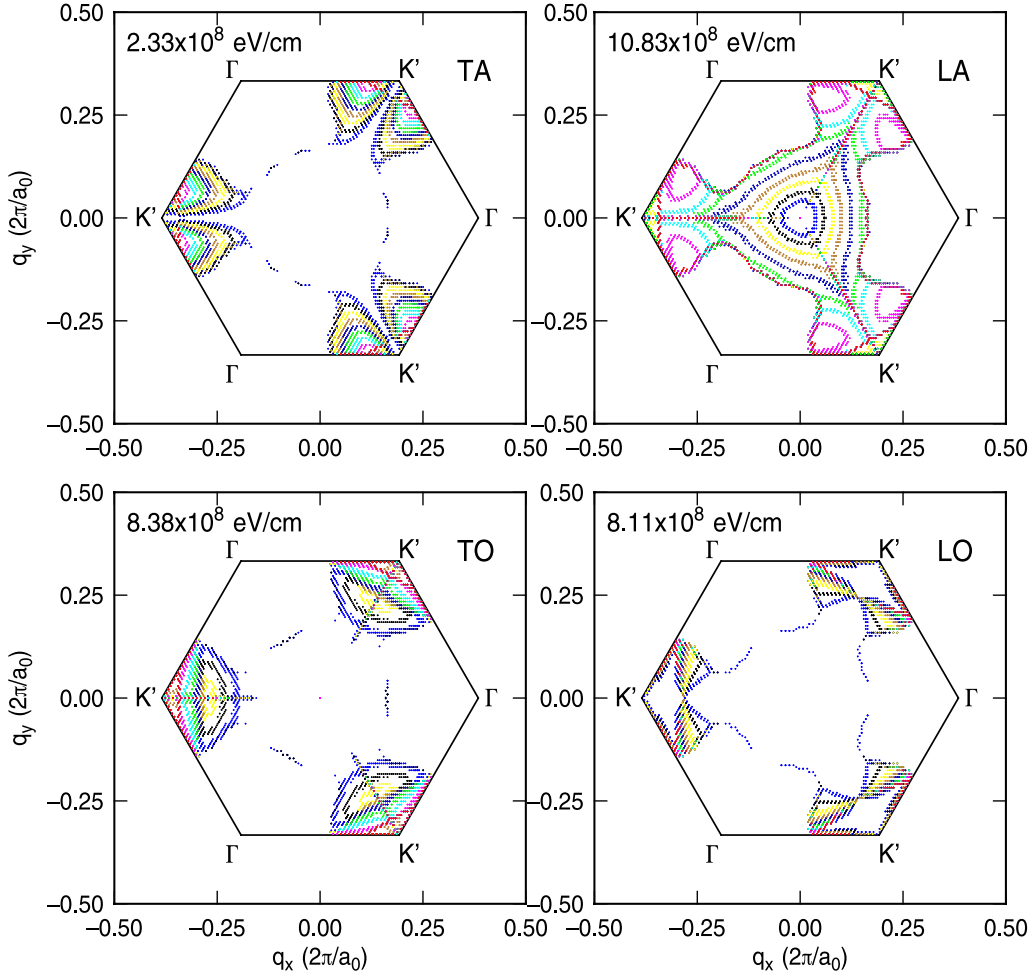


Figure 9. Contour lines in a linear scale for the ‘deformation potential’, i.e., for the quantity $|\langle \mathbf{K}'n' | \hat{H}_{\text{ep}}^{(\eta)} | \mathbf{K}n \rangle|$ given by (45) screened as in (46). The deformation potential is shown here as a function of phonon wavevector $\mathbf{Q} = \mathbf{K}' - \mathbf{K}$ in the first Brillouin zone for an initial electron state at the symmetry point K. The initial and final electron states are both assumed to be in the lowest energy conduction band. The symmetry labels denote the locations of the final electron states in the BZ. The numbers denote the maximum value of the deformation potentials (different for each mode) and the colour scale ranges (in descending order from the indicated maximum value to zero) from red, to purple, green, cyan, brown, ochre, yellow, black, and to dark blue through nine contours. Note that all intervalley transitions between the symmetry points K and K' are relatively weak, while the largest matrix elements appear to be LA-processes connecting the symmetry point K to a region around the symmetry point M (the red region along the K-K' line towards K').

3.3. Dielectric screening

In calculating the strength of the electron–phonon coupling it is generally assumed that the valence electrons respond adiabatically (Born–Oppenheimer) to the displacement of the ions. The validity of the adiabatic approximation is based on the (collective) fast response of the valence electrons, whose plasma frequency is much larger than the phonon frequency, and either on the large dynamic polarizability of single-particle excitations (electron–hole pairs) at the Fermi surface (as in metals) or on their inability to follow the ionic motion (as in materials with a gap larger than the phonon frequency such as semiconductors and insulators). Semimetallic intrinsic graphene, instead, finds itself somewhere between these two limiting cases: since it lacks a gap, phonons can trigger a single-particle response at the Fermi level—unlike the lack of response of gapped dielectrics; but, because of the vanishing density of states at

the Fermi energy, these excitations respond ‘sluggishly’ on a timescale comparable to that of the ionic motion—unlike the almost instantaneous response of metals. For these reasons the validity of the adiabatic Born–Oppenheimer approximation in graphene has been questioned in [122, 123] based on the experimental observation of a stiffening of the Raman G peak. We have already seen that these unique dielectric properties of graphene manifest themselves also in the presence of Kohn anomalies in the phonon spectrum [96–99], a result of the weak (as compared to metals) dielectric screening due to intra- and intervalley processes.

We have discussed here two pseudopotential-based methods to evaluate the electron–phonon coupling: (1) the Quantum-Espresso-based DFT perturbation-theory approach followed not only by Borysenko *et al* for graphene [9], but also by Piscanec *et al* [96] and by Lazzeri *et al* [124] for CNTs, by Lazzeri *et al* in the context of the Kohn anomalies [97, 98], as well as the DFT evaluation of

the deformation potential of AGNRs discussed below (see section 4.1), and (2) the rigid-ion method presented above. These two methods are based implicitly on two different approximations of the dielectric electronic response: the DFT-based approaches assume a full adiabatic (*static*) screening of the displaced atomic potential by employing a change of the atomic pseudopotential $\delta V^{(\eta)}$ (the Kohn–Sham derivative of the potential in this case)—appearing in (28) and (29)—which is re-calculated self-consistently for the displaced-ion configuration. In contrast, within the rigid-ion approximation the valence electrons are assumed to follow rigidly the ionic displacement without any ‘deformable-ion’ rearrangement of the valence charge. Clearly, neither approach is strictly correct, since only a time-dependent analysis can account for the small electronic polarizability of graphene.

In doped or gated graphene, the screening effect of free carriers adds to the complication. The role played by free carriers in screening the nonpolar electron–phonon interaction has been amply discussed and debated in the past decades in the context of bulk semiconductors [125, 126], of two-dimensional electron gases in inversion layers [127] and heterostructures [128, 129], and of one-dimensional quantum-well wires [130]. In general, a simple Thomas–Fermi model has been found to be inadequate in most situations, and the full dynamic treatment of dielectric screening (often treated in the random-phase-approximation, RPA) has been deemed necessary. As we have just seen, accounting for the dynamic response is particularly important in graphene both because electrons at the Fermi energy can respond to excitations of any frequency, albeit partially, and also because, as a consequence of the small mass of carbon atoms, zone-edge optical and acoustic phonons oscillate at a high frequency.

Given this state of affairs, the evaluation of how valence electrons and free carriers affect the strength of the electron–phonon coupling appears to be a daunting (and controversial) task. Here we ignore modifications of the phonon frequency due to the Kohn anomalies and free-carrier screening of acoustic phonons [131]. However, we attempt to correct for the instantaneous but rigid (and so incomplete) response implicitly assumed in our rigid-ion calculations and, quantitatively more important, for free-carrier screening in doped (or gated) graphene. We do so by accounting for the *dynamic* dielectric screening of the variation of the ionic (pseudo) potential $\delta V^{(\eta)}$ appearing in (28) and (29) by using the zero-temperature (approximately valid in degenerate conditions) Wunsch’s screening model [131], equivalent to the expressions give by Hwang and Das Sarma [132]. Therefore we modify the electron–phonon matrix elements computed above as follows:

$$\langle \mathbf{K}' n' | \hat{H}_{\text{ep}}^{(\eta)} | \mathbf{K} n \rangle \rightarrow \frac{\langle \mathbf{K}' n' | \hat{H}_{\text{ep}}^{(\eta)} | \mathbf{K} n \rangle}{1 - [e^2/(2\kappa_0 Q)] \Pi_{\text{RPA}}(Q, \omega_{Q\eta})}. \quad (46)$$

Having already accounted for the (rigid-ion) screening effects of the valence electrons, κ_0 must be understood as the vacuum dielectric constant. Moreover in this expression $Q = |\mathbf{K} - \mathbf{K}'|$ and the dynamic RPA of the polarizability of graphene is given

by:

$$\Pi_{\text{RPA}}(Q, \omega) = \frac{\Pi(Q, \omega)}{1 - [e^2/(2\kappa_0 Q)] \Pi(Q, \omega)}, \quad (47)$$

with

$$\Pi(Q, \omega) = -i\pi \frac{F(Q, \omega)}{\hbar^2 v_F^2} + \Delta P^{(1)}(Q, \omega). \quad (48)$$

As noted in [131], the singularity at $\omega = v_F Q$ appearing in $\Pi(Q, \omega)$ is removed in $\Pi_{\text{RPA}}(Q, \omega)$, but at the expense of a singularity along the dispersion of the plasmons. The first term represents the zero-density contribution and

$$\begin{aligned} \Delta P^{(1)}(Q, \omega) = & -\frac{gE_F}{2\pi\hbar^2 v_F^2} + \frac{F(Q, \omega)}{\hbar^2 v_F^2} \\ & \times \left\{ G\left(\frac{\hbar\omega + 2E_F}{\hbar v_F Q}\right) - \Theta\left(\frac{2E_F - \hbar\omega}{\hbar v_F Q} - 1\right) \right. \\ & \times \left[G\left(\frac{2E_F - \hbar\omega}{\hbar v_F Q}\right) - i\pi \right] - \Theta\left(\frac{\hbar\omega - 2E_F}{\hbar v_F Q} + 1\right) \\ & \left. \times G\left(\frac{\hbar\omega - 2E_F}{\hbar v_F Q}\right) \right\} \end{aligned} \quad (49)$$

is the contribution at nonzero density ($E_F \neq 0$). The functions $F(Q, \omega)$ and $G(x)$ are defined by Wunsch and co-workers [131] as:

$$F(Q, \omega) = \frac{g}{16\pi} \frac{\hbar v_F^2 Q^2}{\sqrt{\omega^2 - v_F^2 Q^2}}, \quad (50)$$

$$G(x) = x\sqrt{x^2 - 1} - \ln\left(x + \sqrt{x^2 - 1}\right), \quad (51)$$

where E_F is the Fermi level measured from the Dirac point, $g = g_v g_s$ is the product of the spin and valley degeneracy. For intrinsic (undoped and un-gated) graphene, $\Delta P^{(1)}(Q, \omega) = 0$ and only the first interband term in (48) survives—a term that Hwang and Das Sarma [132] have shown to yield an ‘effective background dielectric constant’ in the static case ($\omega = 0$) and Wunsch *et al* have shown to result in a renormalization of the acoustic phonons’ frequency and in their increased damping. The term $\Delta P^{(1)}(Q, \omega)$ results from the presence of free carriers and causes a weakening of the electron–phonon coupling with increasing density, especially for the interactions with acoustic phonons. As if the picture were not already sufficiently complicated, we should mention one more concern: the approach we have followed is based on the RPA, but some concerns that have been raised about its validity in graphene [133], at least when using the ‘chiral’ (massless Dirac or Weyl) Hamiltonian often employed to describe single-layer graphene.

3.4. Electron–phonon scattering rates

Using the matrix element just discussed and Fermi’s golden rule, the first-order rate in which a 2D electron of crystal momentum $\hbar\mathbf{K}$ in band n will emit or absorb a phonon from branch η will be:

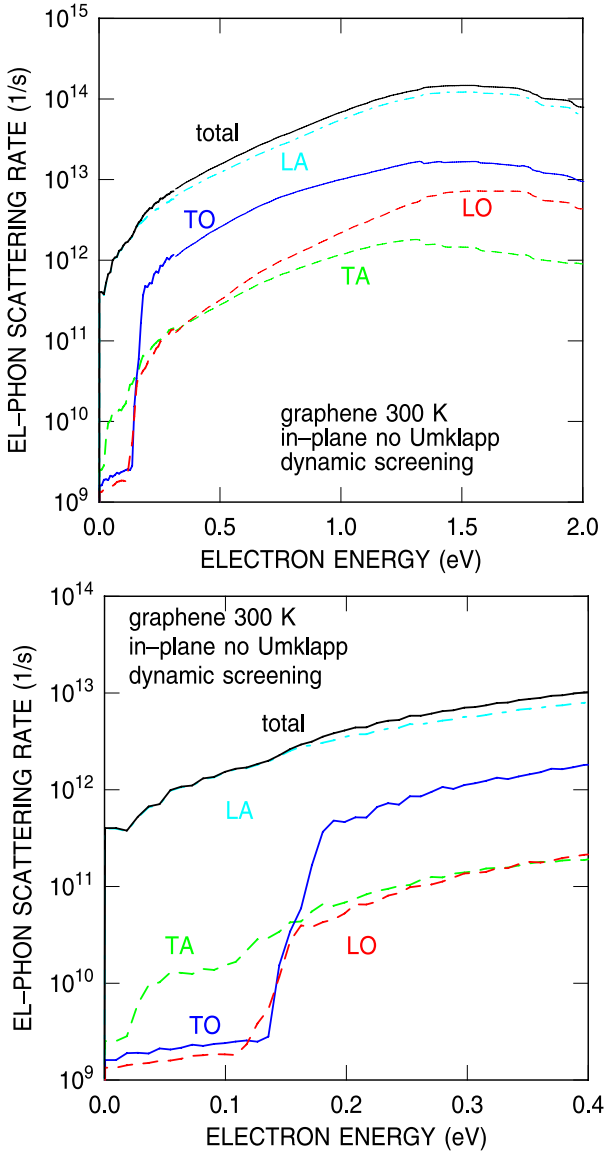


Figure 10. Top: calculated total electron–phonon scattering rates in graphene at 300 K using the ‘in-plane no-Umklapp’ approximation, (45) and the dynamic screening model by Wunsch *et al* [131]. Bottom: as in the top frame, but expanding the low-energy region.

$$\frac{1}{\tau_n^{(\eta)}(\mathbf{K})} = \frac{2\pi}{\hbar} \int \frac{d\mathbf{K}'}{(2\pi)^2} \left| \sum_{\mathbf{G}, \mathbf{G}'} \mathcal{D}_{\mathbf{K}' - \mathbf{K}, \mathbf{G}' - \mathbf{G}}^{(\eta)} u_{\mathbf{K}', \mathbf{G}'}^{(n')*} u_{\mathbf{K}, \mathbf{G}}^{(n)} \right|^2 \times \delta(E_n(\mathbf{K}) - E_n(\mathbf{K}') \mp \hbar\omega_{\mathbf{K} - \mathbf{K}', \eta}), \quad (52)$$

where the upper (lower) sign in the energy-conserving delta corresponds to absorption (emission) processes. Note that here we have used the ‘exact’ form of the matrix element, (43), although in practice we have employed the approximate expression (45). To compute it numerically, we first discretize the 2D BZ with squares centred at points \mathbf{K}_j , and write (52) as:

$$\frac{1}{\tau_n^{(\eta)}(\mathbf{K})} \approx \frac{2\pi}{\hbar} \sum'_{jn'} \left| \sum_{\mathbf{G}, \mathbf{G}'} \mathcal{D}_{\mathbf{K}_j - \mathbf{K}, \mathbf{G}' - \mathbf{G}}^{(\eta)} u_{\mathbf{K}_j, \mathbf{G}'}^{(n')*} u_{\mathbf{K}, \mathbf{G}}^{(n)} \right|^2 \rho_{jn'}. \quad (53)$$

In this equation $\rho_{jn'}$ is the density of states at the final energy in band n' in the mesh element j calculated using a simple modification of the Gilat–Rabenheimer scheme [134] to two-dimensional mesh elements [53]. The ‘primed’ sum indicates that only mesh elements containing the desired final energy should be included in the sum.

For the results shown in the following figures we have employed three different meshes in \mathbf{k} -space: a ‘coarse’ mesh employing 40×40 rectangular elements covering the rectangular section of the BZ, including the (triangular) irreducible wedge of the 2D Brillouin Zone and a similar triangle completing the rectangle; a ‘fine’ mesh of 40×40 rectangular elements covering a similar section of linear dimensions five times smaller around the K-symmetry point; a ‘superfine’ mesh covering the same section, but with 80×80 elements. The use of such extremely fine meshes was found necessary to resolve accurately the low-energy regions around the K and K’ symmetry points. Even so, some numerical artefacts will be evident at the lowest energy shown below. For the tabulation and interpolation of the phonon dispersion a mesh of 300×520 rectangular elements covering the same section has been used.

Figure 10 shows the scattering rates calculated using this approximation and screened as in (46) at a lattice temperature of 300 K for intrinsic (that is, undoped, un-gated, zero-density) graphene. We have used the phonon energies and polarization vectors calculated with the Born–von Kármán method described in section 2.6 above. Note that, opposite to what has been found using DFT [9], we find that scattering with LA modes dominates and the scattering rates are comparable to most empirical models used previously, not suggesting any ‘colossal’ electron mobility. Indeed, by fitting these results to the analytic expressions given by (22) and (23), we see that by lumping all processes into a single longitudinal acoustic mode and a single intervalley optical mode, we obtain values for the effective acoustic and optical deformation potentials of 18 eV and 6×10^8 eV cm $^{-1}$, respectively (see figure 11). This last value, when multiplied by a factor of $\sqrt{2}$ to account for the effect of the overlap factor not included in the expression (23) employed for its extraction, compares quite well with the DFT results by Lazzeri *et al* [98] (8.5×10^8 eV cm $^{-1}$ from the EP-rigid-ion versus 7.9×10^8 eV cm $^{-1}$ from GW-corrected DFT). In contrast, K–K’ intervalley processes appear weak, as discussed in section 3.5 below. However, we should stress once more an issue already mentioned before: since zone-edge models cannot be unambiguously identified as optical or acoustic, what we have labelled as ‘LA’ in figure 10 and as ‘acoustic’ in figure 11 may include contributions from optical components of the zone-edge modes. Finally, the effect of screening at various electron densities is shown in figure 12.

3.5. Electron mobility and drift velocity

We have already discussed at the beginning of this section that our main purpose is to assess whether the intrinsic phonon-limited electron mobility has already been observed (at about $200\,000$ cm 2 V $^{-1}$ s $^{-1}$ [100, 101]) or, instead,

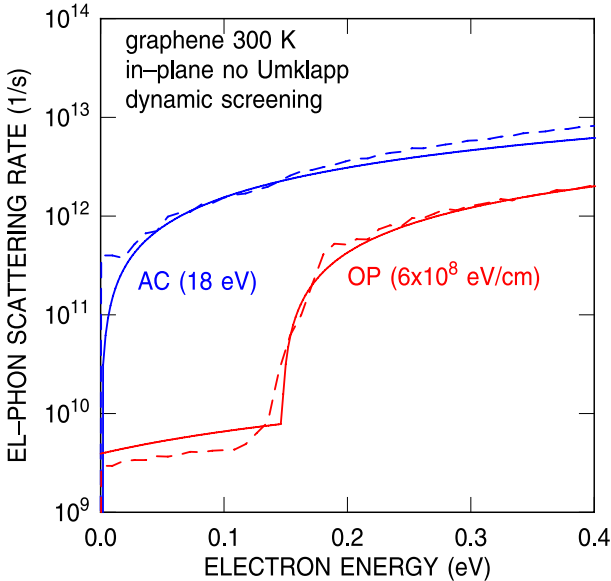


Figure 11. Total electron/acoustic-phonon and electron/optical-phonon scattering rates calculated using the analytic expressions (22) and (23), fitted to the screened rigid-ion results shown in the previous figure. The empirical deformation potentials so obtained can be compared with those employed in the literature.

additional improvements of the graphene growth/deposition processes may yield even more spectacular results, with a mobility exceeding $500\,000 \text{ cm}^2 \text{ V}^{-1} \text{ s}^{-1}$, as suggested by Elias *et al* [102] and Mayorov and co-workers [101], or even exceeding $10^6 \text{ cm}^2 \text{ V}^{-1} \text{ s}^{-1}$, as suggested by the DFT results of Borysenko *et al* [9]. Similar questions can be asked about electron transport at high fields, since the small scattering rates calculated in [9] suggest a drift velocity v_d as high as $\approx 5.5 \times 10^7 \text{ cm s}^{-1}$ at fields of 250 V cm^{-1} at 300 K. In contrast, most theoretical transport studies reported so far suggest much smaller velocities. Even more intriguing, several—but not all—of these studies show the onset of a negative differential mobility (NDM) at sufficiently high fields. Clearly, the vastly different choices made for the deformation potentials Δ_{ac} , Δ_{op} , and Δ_{iv} , discussed before, as well as different choices for the band structure model, phonon dispersion, and overlap factors employed unsurprisingly lead to vastly different results, the common observation being the decreasing electron drift velocity with increasing carrier density. For example, Akturk and Goldsman [16], using an ETB model, find a relatively low saturated velocity ($v_{d,s} \approx 6\text{-}9 \times 10^6 \text{ cm s}^{-1}$), saturating at fields of about 100 kV cm^{-1} , with a slight NDM only at higher fields [16]. Later studies by Chauhan and co-workers [17] show no NDM, with a velocity saturating at about $4 \times 10^7 \text{ cm s}^{-1}$ for a density $5.26 \times 10^{12} \text{ cm}^{-2}$. In contrast, depending on the deformation potentials employed, Shishir *et al* find little if any NDM, and then only at low densities [18], or a strong NDM at most densities [20], with v_d saturating at $4.5 \times 10^7 \text{ cm s}^{-1}$ above 5 kV cm^{-1} , but no NDM at densities larger than about $2 \times 10^{12} \text{ cm}^{-2}$. The onset of NDM in [9] cannot be seen, since Borysenko *et al* show a very large and monotonically increasing drift velocity up to fields of about

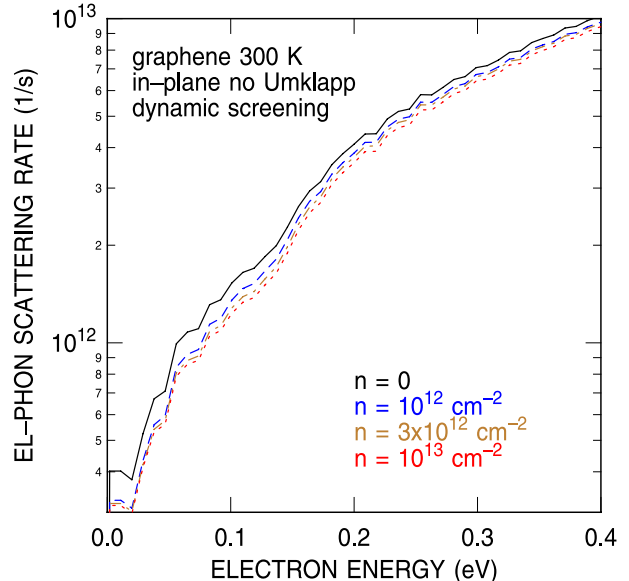


Figure 12. Comparison of the total electron–phonon scattering rates calculated at the indicated electron densities.

250 kV cm^{-1} , as noted above. Interestingly, a similar situation can be found also in the case of the electron drift velocity in AGNRs—NDM having been reported in [135], but not by Amin and co-workers [136].

Experiments performed so far can help only partially. First, suspended graphene of almost-ideal quality is needed. But an even more vexing problem is the strong self-heating observed at electric high fields [121, 137]. The best results we are aware of are indeed those by the group at the University of Illinois at Urbana-Champaign [121], obtained for graphene on SiO_2 . Scattering with charged impurities in the substrate and with interfacial modes (to be discussed below in section 5.1) are Coulomb processes whose strength decreases rather quickly with increasing electron energy, so one may expect that the high-field behaviour of the drift velocity versus field characteristics should not depend strongly on the presence of these scattering mechanisms, while the low-field behaviour will obviously be strongly affected. Other possibly ‘unknown’ scattering mechanisms due to deviations from ideality of the samples may of course be at work, but this is what we have available at present. Dorgan *et al* [121] find that at a nominal temperature of 80 K the sample heats to about 280 K under measurement at about 10 kV cm^{-1} . Driving the samples to fields as high as 20 kV cm^{-1} (beyond which the sample becomes ‘unstable’ [138, 139]), they find that the drift velocity seems to saturate at about $2.5 \times 10^7 \text{ cm s}^{-1}$ in intrinsic samples, with just a hint of NDM perhaps seen at higher carrier densities [121].

We have performed full Monte Carlo simulation to calculate both the electron mobility (obtained from the field-dependent transverse and longitudinal diffusion constant [140]) and the high-field velocity–field characteristics using the EP band structure and rigid-ion electron–phonon scattering rates obtained above. In order to obtain the longitudinal/transverse mobility, $\mu_{L,T}$, from the diffusion

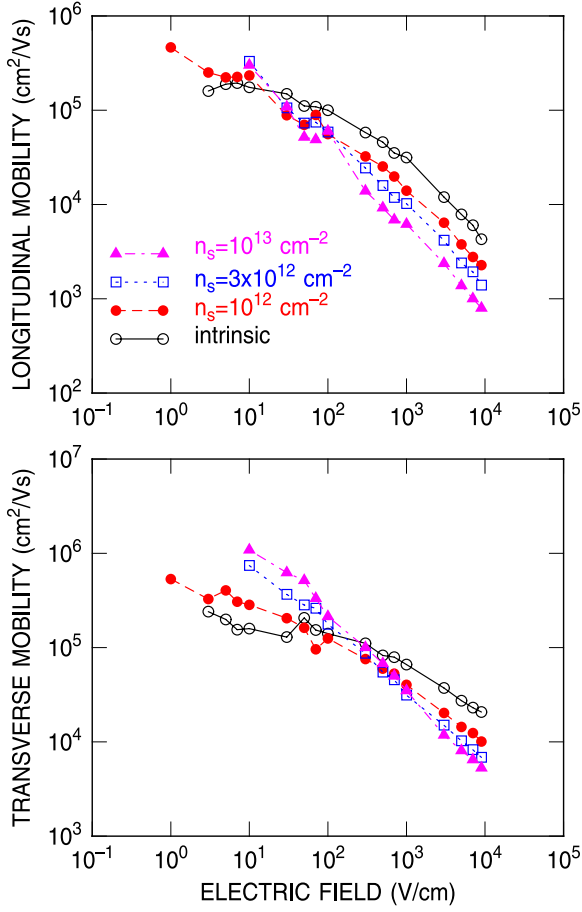


Figure 13. Longitudinal (top) and transverse (bottom) electron mobility in graphene at 300 K as a function of electric field along the [10] direction, calculated using the Monte Carlo method. The various curves are parametrized by the electron density.

constant, $D_{L,T}$, we have employed an extension of the Einstein relation [141], starting from the general expression:

$$\mu = \frac{e}{n} \frac{dn}{dE_F} D. \quad (54)$$

Using a linear approximation $E(k) = \hbar v_F k$ for the electron dispersion at low energy, accounting for the valley and spin degeneracy,

$$\begin{aligned} n &= \frac{2}{\pi} \left(\frac{k_B T}{\hbar v_F} \right)^2 \int_0^\infty d\eta \frac{\eta}{1 + \exp(\eta - \eta_F)} \\ &= -\frac{2}{\pi} \left(\frac{k_B T}{\hbar v_F} \right)^2 Li_2[\exp(\eta_F)], \end{aligned} \quad (55)$$

where $\eta_F = E_F/(k_B T)$ is the Fermi energy in thermal units and Li_2 is the Spence (or ‘dilogarithmic’) function. Also:

$$\frac{dn}{dE_F} = \frac{2}{\pi} \frac{k_B T}{(\hbar v_F)^2} \int_0^\infty d\eta \eta \frac{\exp(\eta - \eta_F)}{[1 + \exp(\eta - \eta_F)]^2}, \quad (56)$$

so that, finally,

$$\begin{aligned} \mu &= \frac{e}{k_B T} D \int_0^\infty d\eta \eta \frac{\exp(\eta - \eta_F)}{[1 + \exp(\eta - \eta_F)]^2} \\ &\times \left(\int_0^\infty d\eta \frac{\eta}{1 + \exp(\eta - \eta_F)} \right)^{-1}. \end{aligned} \quad (57)$$

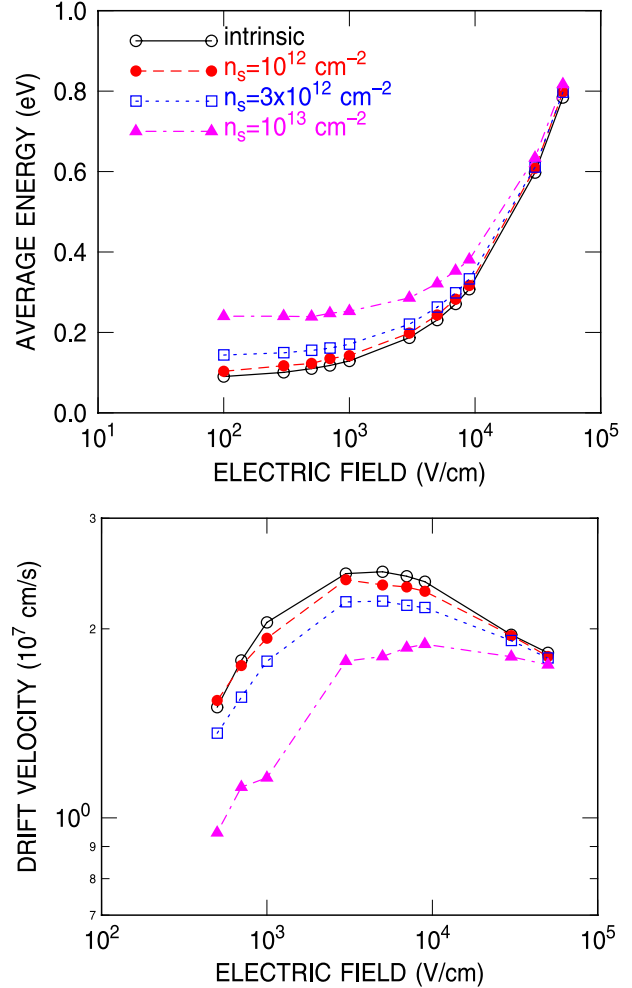


Figure 14. Average electron energy (top) and drift velocity (bottom) in graphene at 300 K as a function of electric field along the [10] direction, calculated using the Monte Carlo method. The various curves are parametrized by the electron density.

Although this expression is correct only when the electrons populate the low-energy region of the conduction band and the linear approximation for $E(k)$ holds, we have also employed it to extract the mobility even at fields higher than the Ohmic regime. So, while the computed $D_{L,T}$ is correct, our high-field results for the mobility should be interpreted only qualitatively.

Figure 13 shows the longitudinal and transverse mobility as a function of the electric field, parametrized by the density, while figure 14 shows the average electron energy and drift velocity. The electric field has been applied along the [1, 0] direction, which, in our choice of coordinates, corresponds to the Γ -M direction in reciprocal space. Note in figure 13 a room-temperature low-field longitudinal electron mobility of about $200\,000 \text{ cm}^2 \text{ V}^{-1} \text{ s}^{-1}$ in intrinsic suspended graphene. At zero field, the mobility increases to about $600\,000 \text{ cm}^2 \text{ V}^{-1} \text{ s}^{-1}$ as the electron density increases to 10^{12} cm^{-2} , an effect mainly due to dielectric screening, since momentum is relaxed mostly by low-frequency longitudinal acoustic phonons which are efficiently screened statically. This trend is reversed as soon as even small fields

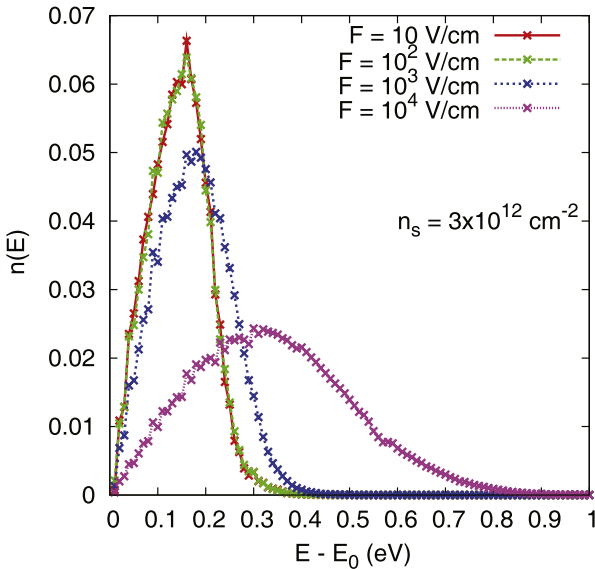


Figure 15. Calculated electron energy distribution function at 300 K for various values of the electric field, as obtained from Monte Carlo simulations including only electron–phonon scattering.

($\sim 10 \text{ V cm}^{-1}$) are applied, the mobility decreasing quickly with increasing field and density. This is the result of the fact that carrier heating makes the electrons probe the larger momentum relaxation rates due to intervalley processes assisted by large-energy zone-edge phonons, processes which are left essentially unaffected by weak dynamic screening. A similar behaviour is observed for the transverse mobility (bottom frame of figure 13), although at higher values.

Regarding the electron drift velocity (figure 14), note the peak 300 K value of about $2.5 \times 10^7 \text{ cm s}^{-1}$ at a field of 20 kV cm^{-1} . Note also the onset of NDM for fields above $3\text{--}5 \text{ kV cm}^{-1}$ at low densities—but this NDM almost disappears at densities of about 10^{13} cm^{-2} . The NDM is caused by a reduction of the electron velocity as the electrons gain energy and populate the ‘flatter’ regions of the BZ around the M symmetry point (see figure 1). At even larger electric fields, some electrons transfer to the Γ valley occurs, possibly via the M symmetry point, since our EP band structure shows a relatively small energetic separation, $\approx 2.5 \text{ eV}$, between the energy at M and the energy at Γ .

Figure 15 shows the electron energy distributions calculated for various values of the electric field, while figure 16 shows the wavevector distribution of the phonons of all branches emitted and absorbed by the electrons. Similar results for the electron drift velocity, obtained using a hydrodynamic model, have been reported by Serov *et al* [142] using $\Delta_{ac} = 19 \text{ eV}$ (equivalent to 25 eV when accounting for the wavefunction-overlap factor), $\Delta_{op} = 6 \times 10^8 \text{ eV cm}^{-1}$ and accounting also for scattering with charged impurities and interfacial optical modes. Therefore it appears that the use of the rigid-ion approximation and of the empirical pseudopotentials of [8] provides a picture in satisfactory agreement with available experimental data. In particular, scattering with LA phonons is the dominant mechanism for energy and momentum loss because of the relatively large value of the effective deformation potential, $\Delta_{ac} \approx 18 \text{ eV}$.

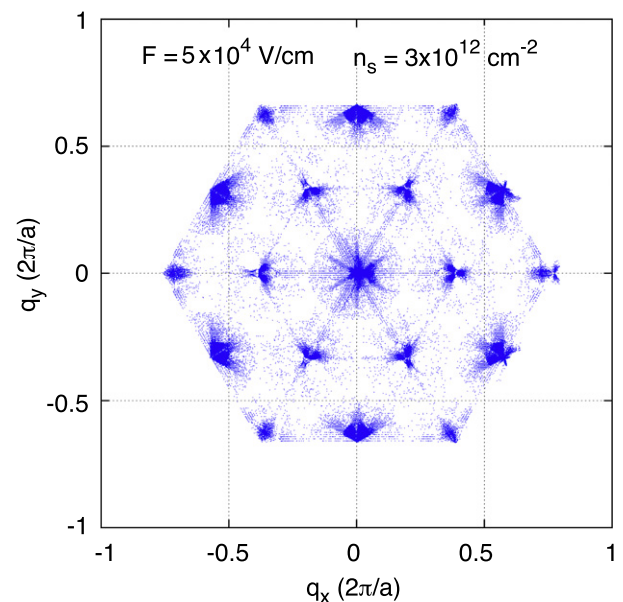
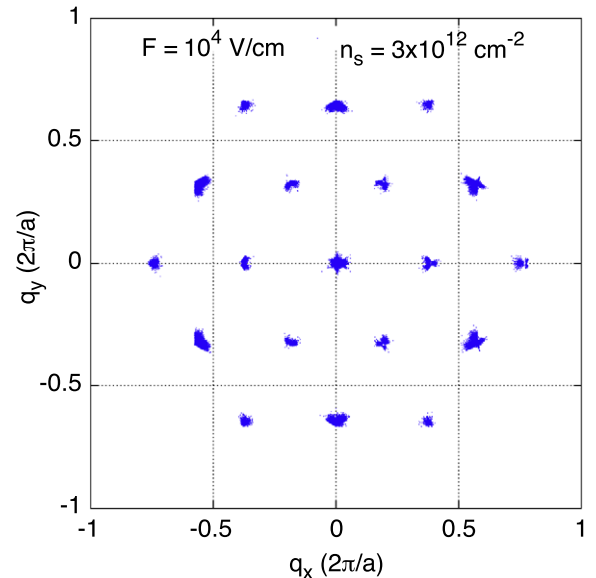


Figure 16. Momentum distribution of emitted and absorbed phonons (all branches) in the first and second Brillouin zones of graphene for a value of the electric field only slightly above (10^4 V cm^{-1} , top frame) and significantly above ($5 \times 10^4 \text{ V cm}^{-1}$, bottom frame) the threshold of NDM. Points at the zone-centre ($Q = 0$) assist intravalley transitions of electrons populating both the K and the K' symmetry points. K-phonons mostly identify K–K’ intervalley processes (resulting in the observed 6-fold symmetry to be compared to the 3-fold symmetry seen in figure 9). Also visible are ‘intervalley’ K–K transitions (‘Umklapp’ processes). At the higher field the increasing number of phonons along the Γ –K line assist an increasing number of transitions from K or K' to regions around the M symmetry point, processes which are mainly responsible for the NDM.

4. Electron transport in armchair-edge graphene nanoribbons

The need to open a gap of width several $k_B T$ for nanoelectronics applications, coupled to the fact that sufficiently narrow AGNRs exhibit a gap of such a magnitude,

renders extremely interesting the investigation of AGNRs for nanoelectronics applications. Therefore it is important to obtain information about the intrinsic phonon-limited electron mobility in these structures as well. Additional scattering processes important in AGNRs, mainly with line-edge roughness, will be discussed in section 4.1.

4.1. Electron–phonon interaction and electron mobility

The electron mobility in AGNRs has been investigated extensively before (see for example [12, 23–29, 83, 135, 143, 144]), but, as in the case of graphene sheets, the choice made for the band structure, the phonon dispersion, and the deformation potentials leads to a wide range of results. An almost general consensus has emerged, confirming that scattering with longitudinal acoustic phonons constitutes the dominant scattering mechanism, as we have seen in the case of graphene sheets. Therefore, of notable interest are recent publications in which DFT has been used to calculate the longitudinal acoustic deformation potential needed to calculate the electron mobility in AGNRs [30–32]. Interestingly, and perhaps not surprisingly, the claromatic properties of AGNRs are reflected not only in the ‘peculiar bandgap structure of graphene nanoribbons’ (to quote Ezawa’s expression [65]) but also in the deformation potential.

In principle, simple considerations based on the effective mass may lead us to predict a claromatic dependence of the electron mobility in AGNRs: since the electron effective mass is roughly proportional to the (direct) bandgap and since, in turn, the electron mobility is inversely proportional to the effective mass, one could anticipate a claromatic behaviour of the electron mobility exactly opposite to the behaviour of the bandgap, i.e., $\mu_{3p+2} > \mu_{3p} > \mu_{3p+1}$. However, the recent DFT calculations we have just mentioned—performed within the effective-mass approximation with width-dependent deformation potentials and ignoring overlap-factor effects—have led Long *et al* [30] to predict the unexpected trend $\mu_{3p} > \mu_{3p+2} \gtrsim \mu_{3p+1}$. This behaviour was attributed mainly to a claromatic dependence of the longitudinal acoustic deformation potential, $\Delta_{ac,3p+1} \gtrsim \Delta_{ac,3p+2} > \Delta_{ac,3p}$. In the same spirit, but with qualitatively slightly different results, Wang *et al* [32] have reported the trend $\Delta_{ac,3p+2} \gtrsim \Delta_{ac,3p+1} > \Delta_{ac,3p}$.

Here we follow the lead of these studies, expanding them to include the claromatic variation not only of the deformation potential (computed using DFT), but also of the effective mass (accounted for in a much more general way employing the full EP band structure of AGNRs). We also account for a more accurate approximation of the electron–phonon matrix elements accounting for the overlap integral between initial and final electronic states. We should note that the effect of localized (or ‘confined’) AGNR phonons [145] has not been taken into account.

For the DFT simulations, we have used the Quantum Espresso package [60], employing the Rappe–Rabe–Kaxiras–Joannopoulos ultrasoft pseudopotentials and, as in the previous VASP simulations described above, adopting the PBE exchange–correlation functional in the GGA. We have

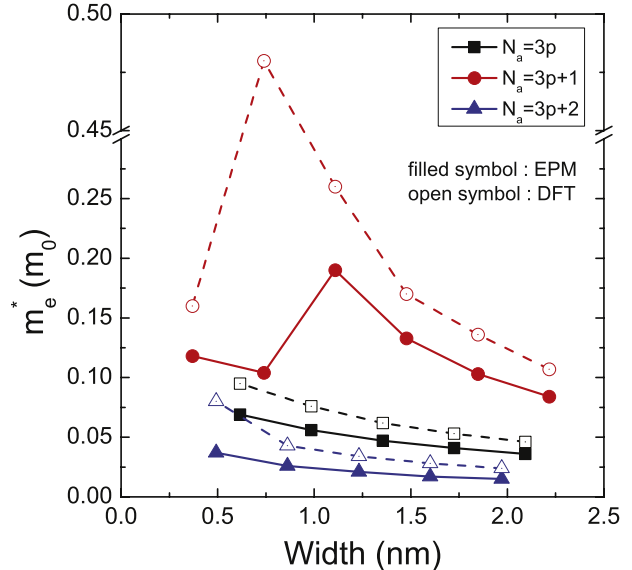


Figure 17. Calculated electron effective mass at the conduction band minimum at $k_x = 0$ for AGNRs using both EP (solid symbols) and DFT (open symbols).

used a plane-wave basis expansion and a kinetic energy cutoff of 80 Ryd and a Monkhorst–Pack grid of $16 \times 1 \times 1$ for the integration over the BZ. Atomic relaxation was performed using a quasi-Newton algorithm, with a convergence threshold of 10^{-5} au for the forces.

In figure 17 we compare the EP and DFT results for the electron effective mass at the conduction band minimum (CBM) (located in these structures at the $k_x = 0$) for AGNRs as a function of ribbon width. The effective masses are obtained by fitting the electron dispersion at the CBM to a parabolic approximation. As expected, the claromaticity of the effective mass is the same as the bandgap for both EP and DFT, but the mass obtained using DFT is slightly larger than EP calculations for all three groups for AGNRs. This result is somewhat surprising, since the lower gap usually obtained from DFT implies a smaller mass. However, in the narrow ribbons we consider here quantum confinement effects play a major role in determining the gap, and the DFT-calculated gap is similar or even larger than the EP-calculated gap (see figure 5). Note the abrupt change of the effective mass of $N_a = 3p + 1$ AGNRs, which is caused by the crossing of conduction bands as the ribbons width increases. Since both EPs and DFT yield comparable results, we employ the EP wavefunctions in computing the mobility using the Kubo–Greenwood formalism described below.

The low-field mobility along the transport direction (x -direction) of the ribbon can be written as:

$$\mu_{xx} = \frac{1}{N_L} \sum_l n_l \mu_{xx,l}, \quad (58)$$

where l represents the specific conduction subband (15 subbands from the CBM are used), n_l is the electron density in each band, and the quantity N_L represents the total electron

line density. The mobility $\mu_{xx,l}$ in band l is given as:

$$\begin{aligned} \mu_{xx,l} &= \frac{e}{k_B T \pi n_l} \\ &\times \int dk_x v_l^2(k_x) \tau_{\text{tot},l}(k_x) f_0[E_l(k_x)] \\ &\times \{1 - f_0[E_l(k_x)]\}, \end{aligned} \quad (59)$$

where k_x is the electron wavenumber along the axial direction of the ribbon, $v_l(k_x) = (1/\hbar)dE_l(k_x)/dk_x$ is the electron group velocity in band l , $E_l(k_x)$ is the dispersion in band l , and $f_0(E)$ is the electron Fermi–Dirac distribution function at equilibrium. The total electron–phonon momentum relaxation rate can be written as:

$$\frac{1}{\tau_{\text{tot},l}(k_x)} = \frac{1}{\tau_{\text{ac},l}(k_x)} + \frac{1}{\tau_{\text{op(ab)},l}(k_x)} + \frac{1}{\tau_{\text{op(em)},l}(k_x)}, \quad (60)$$

where the momentum relaxation rates for acoustic (ac) and optical (op) modes are computed using the deformation potential approximation:

$$\begin{aligned} \frac{1}{\tau_{\text{ac(op)},l}(k_x)} &= \frac{2\pi}{\hbar} |V_{\text{ac(op)}}|^2 \\ &\times \sum_{l'} \int \frac{dk'_x}{2\pi} \mathcal{I}_{l,l'}(k_x, k'_x) \delta[E_l(k_x) - E_{l'}(k'_x)], \end{aligned} \quad (61)$$

where $|V_{\text{ac(op)}}|^2$ represents the matrix elements for scattering with acoustic(optical) phonons and $\mathcal{I}_{l,l'}(k_x, k'_x)$ is the ‘form factor’ explicitly obtained from the EP wavefunctions:

$$\mathcal{I}_{l,l'}(k_x, k'_x) = \int d\mathbf{R} |\zeta_{l,k_x}^*(\mathbf{R})|^2 |\zeta_{l',k'_x}(\mathbf{R})|^2, \quad (62)$$

where $\zeta_{l,k_x}(\mathbf{R})$ is the two-dimensional envelope wavefunction averaged over the length of a unit cell:

$$\zeta_{l,k_x}(\mathbf{R}) = \frac{1}{A_c^{1/2}} \sum_{\mathbf{G}_\perp} u_{k_x, G_x=0, \mathbf{G}_\perp}^{(l)} e^{i\mathbf{G}_\perp \cdot \mathbf{R}}, \quad (63)$$

where A_c is the area of the cell on the two-dimensional plane perpendicular to the axial direction of the ribbon, \mathbf{R} is the coordinate on this plane, and \mathbf{G}_\perp denotes the projection of the reciprocal-lattice vectors \mathbf{G} on the cross-sectional (y, z) plane of the ribbon. The use of the expression (63) for the cell-averaged wavefunctions follows from having retained only the terms $G_x = 0$ to reach expression (61). This is analogous to the in-plane no-*Umklapp* approximation made in (45) and we shall refer to this approximation as the ‘in-line no-*Umklapp*’ approximation. Thus, the conservation of longitudinal crystal momentum implicitly assumed in (61) is $\hbar k_x - \hbar k'_x = \hbar q_x$. Finally, the form $\mathcal{I}_{l,l'}(k_x, k'_x)$ for the form factor has been obtained in a standard way by performing the integration over the perpendicular component $\mathbf{Q}_\perp = (q_y, q_z)$ of the phonon wavevector, assuming \mathbf{q} -independent matrix elements. Indeed, for the matrix elements $|V_{\text{ac(op)}}|^2$ we have employed the following forms: for optical phonons, consistent with (23):

$$|V_{\text{op}}|^2 = \frac{D_{\text{op}}^2 \hbar}{2\rho_g \omega_{\text{op}}} \begin{cases} N_{\text{op}} & (\text{absorption}) \\ N_{\text{op}} + 1 & (\text{emission}), \end{cases} \quad (64)$$

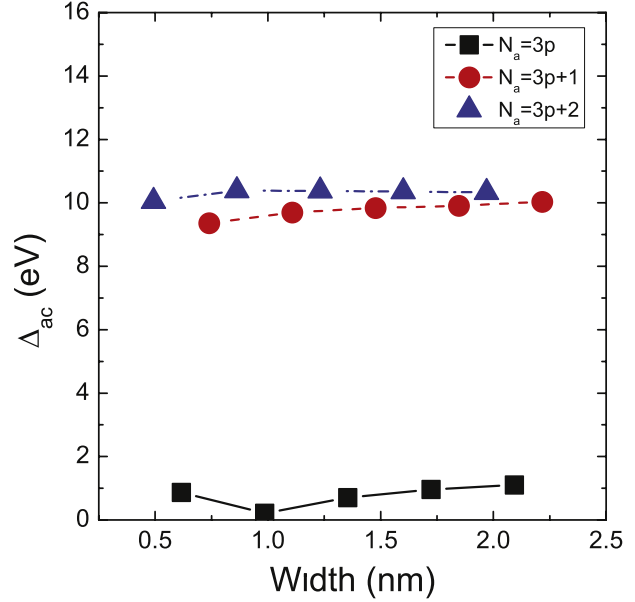


Figure 18. Acoustic deformation potential Δ_{ac} as a function of ribbon width calculated from DFT.

where N_{op} is the Bose–Einstein occupation number of dispersionless optical phonons of energy $\hbar\omega_{\text{op}}$ chosen to take the value of 0.175 eV as a BZ-average obtained from DFT and from the Born–von Kármán results shown in figure 8, and we have adopted for D_{op} the value of 5×10^8 eV cm⁻¹, similar to what is found in bulk graphene. Finally, $\rho_g = 2.33 \times 10^{-3}$ kg cm⁻³ is the mass density of graphite. Note that the wavefunctions (63) are normalized over the entire area of the supercell A_c while their support extends only over the cross-section of the ribbon. Therefore, despite the apparent dependence on ρ_g^{-1} , the squared matrix element in (61) depends on ρ_L^{-1} , the inverse linear mass density of the ribbon.

For acoustic phonons, we have assumed the ‘usual’ momentum-independent matrix element for either emission or adsorption: (see (22)):

$$|V_{\text{ac}}|^2 = \frac{\Delta_{\text{ac}}^2 k_B T}{2\rho_g v_l^2}, \quad (65)$$

where Δ_{ac} is the longitudinal acoustic deformation potential. To calculate this quantity for a given AGNR using DFT we follow the approach given in [30, 32]. We apply a small amount of uniaxial strain along the length of each ribbon, let the systems relax, and then compute the deformation potential as the change of the CBM as a function of strain, ϵ :

$$\Delta_{\text{ac}} = \frac{\delta(E_{\text{CBM}} - eV_{\text{vac}})}{\delta\epsilon}, \quad (66)$$

where the shift of the CBM is referenced to the energy of the vacuum level, eV_{vac} , and four values of strain are applied, $\epsilon = -1.0\%, -0.5\%, 0.5\%$ and 1% . Figure 18 shows the calculated deformation potentials Δ_{ac} as a function of ribbon width. Note that in computing the electron mobility we have left these deformation potentials ‘unscreened’, contrary to the case of

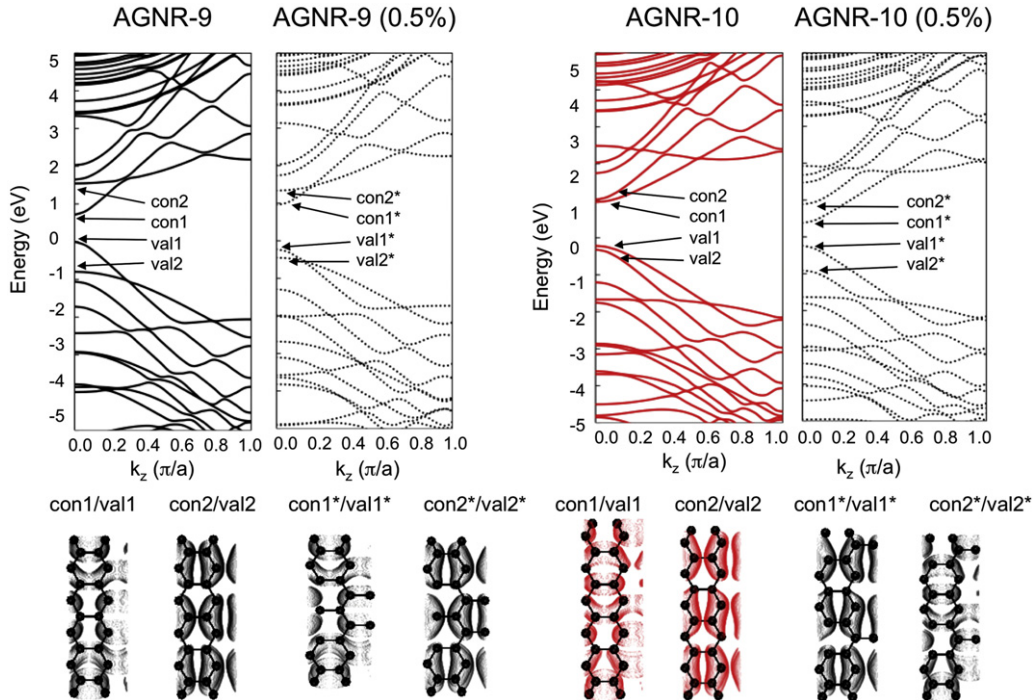


Figure 19. Calculated band structure and electron charge density at $k_x = 0$ for the top two valence bands/bottom two conduction bands computed with DFT for a 9-AGNR ($3p$) and a 10-AGNR ($3p + 1$), with and without strain. The electron charge density plots for the $3p + 2$ AGNRs are essentially the same as for the $3p$ ribbons.

graphene. This is due to the fact that some form of static screening is included when calculating Δ_{ac} from DFT and the presence of a gap in AGNRs renders screening negligible at low line densities. At higher densities screening effects may be accounted for by following or extending the approaches described in [146] for the general case of a one-dimensional electron gas, [147], for the specific case of AGNRs, or [148, 149] for cylindrical nanowires.

As reported in previous studies [30, 32], the deformation potentials also have a claromatic dependence, where $\Delta_{ac,3p+2} \gtrsim \Delta_{ac,3p+1} > \Delta_{ac,3p}$, which is different from the trend observed for the bandgap. In addition, applying a small amount of uniaxial strain (where the meaning of ‘small’ depends on the bandgap of the unstrained ribbon [150], but holds true in these simulations) the bandgap changes linearly, and for a positive strain increases for the $3p$ and $3p+2$ ribbons and decreases for the $3p+1$ ribbons. It is interesting to note that previous studies also report that applying a larger strain results in oscillations of the bandgap, which are ‘out of phase’ for the $3p+1$ ribbons compared to the $3p$ and $3p+2$ ribbons. The change of the bandgap with strain can be understood by examining the electron charge density at $k_x = 0$ (CBM) of the first two conduction bands and valence bands, as shown in figure 19 for the 9-AGNR, and 10-AGNR with and without strain. As can be seen in figure 19, for the $3p$ (and also the $3p+2$, although it is not shown) ribbons, the shape of the edges sets up a charge density of the bottom (top) of the conduction (valence) band that is parallel to the ribbon axis. When the ribbon is strained these bands will increase in energy, since the strain acts to increase the distance between the atoms in the parallel direction. The reverse occurs for the second lowest

(highest) conduction (valence) bands in which the charge density is primarily perpendicular to the ribbon’s edges. For the $3p+1$ ribbons, the parallel and perpendicular charge density are nearly degenerate in energy, due to the asymmetry (chirality) of the carbon atoms at the edges of the ribbon. In this case, the change in bandgap is strongly governed by the change in the second lowest (highest) conduction (valence) band because of the strain, and therefore the gap decreases. These considerations based on the claromaticity of the ribbons and the importance of the edges explain why the deformation potential Δ_{ac} obtained here differs from the value found for an ideal graphene sheet.

Using the deformation potentials explicitly obtained from DFT and the electronic band structures from EP, we calculate the low-field electron mobility at a given electron line density N_L and temperature $T = 300$ K. Figure 20(a) shows the total momentum relaxation rate as a function of the electron energy, referenced to the CBM at $N_L = 5 \times 10^5 \text{ cm}^{-1}$, and (b) shows the low-field mobility as a function of the line density for 8-AGNR, 9-AGNR and 10-AGNR. The claromatic dependence of the mobility as a function of the ribbon width is shown in figure 21(a), where the phonon-limited mobility ranges from $\sim 10^3$ to $\sim 10^6$ with the claromaticity of $\mu_{3p} > \mu_{3p+1} > \mu_{3p+2}$. Obviously, we see that the claromaticity of the deformation potential dominates the picture—although comparing the $3p+1$ to the $3p+2$ ribbons we see evidence of some competing effects due to overlap factors, and especially due to variations of the effective mass, since $\mu_{3p+2} > \mu_{3p+1}$ despite the fact that $\Delta_{ac,3p+2} > \Delta_{ac,3p+1}$. In general, these effective-mass and overlap-factor effects result in a difference of the mobility between the $3p+2$ - and $3p+1$ -wide ribbons

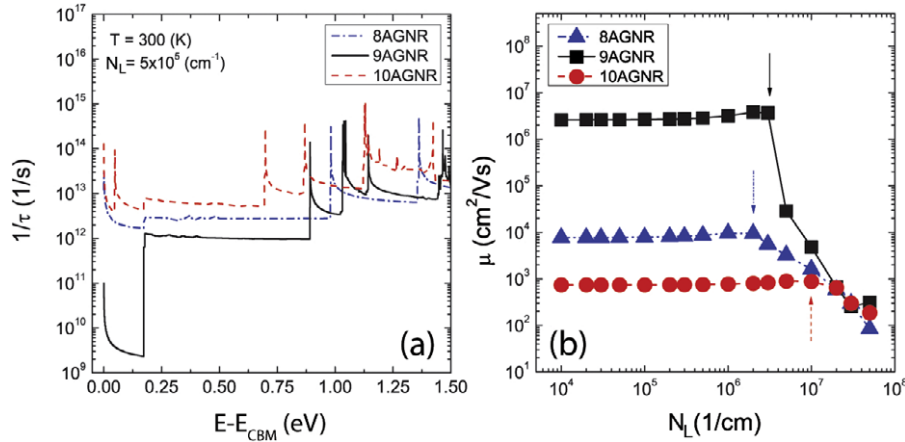


Figure 20. (a) Calculated total momentum relaxation rate as a function of electron kinetic energy measured from the bottom of the conduction band. (b) Low-field mobility versus electron line density for an 8-, 9-, and 10-AGNR.

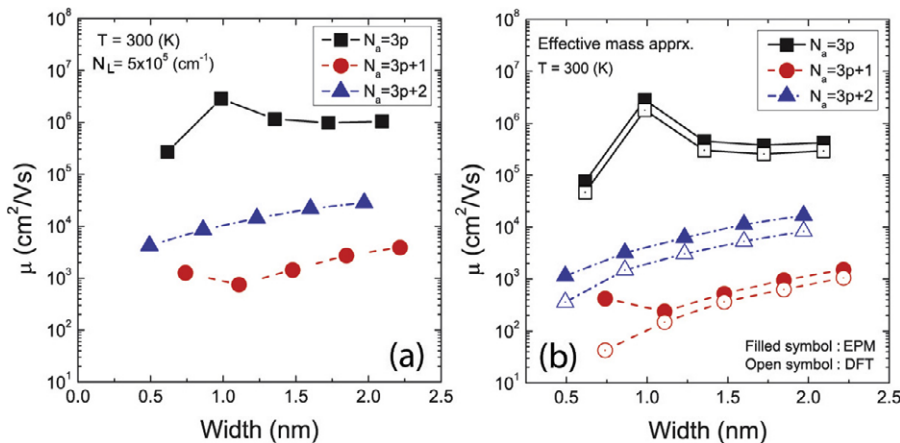


Figure 21. Phonon-limited electron mobility using (a) the Kubo–Greenwood formula with full-band structure and (b) the effective mass approximation with effective masses calculated from EP (solid symbols) and DFT (open symbols).

of roughly one order of magnitude, even though the difference of the deformation potential is small (figure 18) and would suggest the opposite trend.

Finally, in figure 21(b) we show the electron mobility calculated using the simple effective mass approximation following [30–32]. In addition to the same qualitative trend, note that the mobility using the effective masses from EP (solid symbols) is slightly higher than the masses from DFT (open symbols) because of the slightly smaller masses obtained from the EP, as shown in figure 17(b).

Note that throughout this discussion we have implicitly ignored the role played by scattering with optical phonons. Indeed, even in $3p$ -wide ribbons they do not affect the mobility: the large energy of LO and TO modes strongly limits absorption processes, because of their small Bose–Einstein occupation (which is assumed to be minimally perturbed away from equilibrium in these calculations), and also emission processes, since thermal electrons are unable to emit large-energy excitations.

The overall conclusion we reach is that ideal $3p$ -wide ribbons could potentially exhibit an electron mobility comparable to intrinsic graphene. Less impressive is the

mobility in $3p + 1$ and $3p + 2$ AGNRs. Thus, the control of the ribbon width is of paramount importance even when considering only the phonon-limited mobility. Section 4.2 will strengthen this conclusion, although on the basis of different considerations.

4.2. Line-edge roughness scattering

The satisfactory phonon-limited electron mobility in AGNRs shown in the previous section reinforces our interest in these structures. However, one main problem we point out in this section originates from the need to maintain ideally straight edges (and, as discussed in section 2.5, potentially the type of functional groups terminating the edges, although the effect this has on scattering will not be discussed here). How crucial this constraint is may be simply illustrated by the following consideration: interface/surface roughness in inversion layers, thin semiconductor bodies or nanowires or line-edge roughness in ribbons is usually phenomenologically described as the perturbation caused by the change of the energy of the n th subband, ΔE_n , with a randomly changing thickness, diameter, or width of the structure. Thus, electrons

in subband n will see a randomly varying ‘scattering potential’ dE_n/dw , where dw represents the change of the thickness, diameter, or width of the structure. The elastic scattering rate corresponding to this perturbation can be calculated by assuming a random variation of w with some power spectrum Δ_q , where q is the Fourier variable in 2D (for thick bodies) or in 1D (for NWs and AGNRs); this spectrum is commonly parametrized by a correlation length Λ and a root-mean-square (rms) ‘step height’ Δ . The resulting squared matrix element, $|M_{\text{SR},\text{LER};q}|^2$ for a transition from a state k to a state $k' = k + q$ (which represent the initial and final k -states in 2D or 1D reciprocal space) is of the form:

$$|M_{\text{SR},\text{LER};k-k'}|^2 = \Delta_{k-k'}^2 \left| \frac{dE_n}{dw} \right|^2. \quad (67)$$

This phenomenological description actually represents correctly the Prange–Nee [151, 152] contribution to roughness scattering in the particular case of intra-subband processes, while Coulomb-related effects, often a significant contribution [148, 153], are ignored by this simple picture. The important point to note here is that in thick bodies and nanowires the variation of the bandgap (and so of E_n) with changing thickness or diameter is ‘smooth’. In this case, dE_n/dw will take values of the order of 0.1 eV nm^{-1} or less. In contrast, the claromatic variation of the gap of AGNRs, shown in figure 5, results in values of the order of 1 eV nm^{-1} , or more, for dE_n/dw . In turn, this implies that the LER scattering rates in AGNRs will be two to three orders of magnitude larger. Actually, they will be so large as to imply a breakdown of perturbation theory. As already remarked by Gallagher *et al* [154], although in the context of disorder induced by charged impurities, in a rough AGNR electrons will ‘puddle’ in lower-bandgap sections with the formation of quantum dots and transport may only occur via temperature-activated hopping (or tunnelling) among these dots. In other words, the Bloch functions one usually employs to apply the machinery of perturbation theory are not connected perturbatively to these localized states [33]. Therefore, our use of perturbation theory should be regarded as a means to understand the basic physics, but quantitative estimates of the carrier mobility in rough AGNRs require additional information about thermally-activated processes that are beyond the scope of this work.

The effect of line-edge roughness (LER) in AGNRs has been studied extensively before. Studies based on analytic approximations of the band structure (and so, to the variation of the AGNR bandgap with ribbon width), provide qualitative estimates and capture the basic physics of electron transport but, unfortunately, cannot capture the claromatic behaviour of figure 5 [23, 108, 155, 156], since these models are usually based on p_z -only, nearest-neighbour-only ETB. How crucial this is has also been pointed out by Zhao *et al* [76], who have stressed the need to account for at least third nearest-neighbour interactions (so capturing the Clar resonant behaviour) in order to account correctly for LER scattering. The chemical reconstruction of the ribbon edges and its effect on transport has also been studied by Du Bois *et al* [157].

The approach we employ here, following [33], goes beyond the original pioneering approach proposed by Ando (see [1]) by using empirical pseudopotentials to calculate the change of the atomic potential in a cell due to either a shift of the structure in the width direction of the AGNR (representing correlated roughness corresponding to snaking ribbons) or to the addition/removal of atomic lines at the edges, as required to treat uncorrelated or anti-correlated roughness. We consider the case of AGNRs with their axis along the x direction, cross-section on the (y, z) plane, and width W along the y -axis fixed by the number N_a of atomic lines.

In our first approach (for correlated roughness only) we describe the roughness by a shift of the atoms along the y direction by an amount $-\Delta_x$, varying along the length of the ribbon described by its Fourier decomposition:

$$\Delta_x = \sum_q \Delta_q e^{iqx}. \quad (68)$$

We shall assume for its power spectrum $\langle |\Delta_q|^2 \rangle$ the exponential form:

$$\begin{aligned} \langle \Delta_x \Delta_0 \rangle &= \Delta^2 e^{-|x|/(\sqrt{2}\Lambda)} \rightarrow \langle |\Delta_q|^2 \rangle \\ &= \sqrt{2}\Delta^2 \Lambda (1 + q^2 \Lambda^2 / 2)^{-1}. \end{aligned} \quad (69)$$

The displacement of the atoms modifies the potential as follows:

$$\begin{aligned} V^{(\text{lat})}(\mathbf{r}) &= \sum_{\alpha} V^{(\alpha)}(\mathbf{r} - \mathbf{r}_{\alpha}) \\ &= \sum_{\alpha} \sum_{\mathbf{G}} V_{\mathbf{G}}^{(\alpha)} e^{i\mathbf{G} \cdot (\mathbf{r} - \mathbf{r}_{\alpha})} \\ &= \sum_{\mathbf{G}} V_{\mathbf{G}}^{(\text{lat})} e^{i\mathbf{G} \cdot \mathbf{r}} \\ &\rightarrow V^{(\text{lat})}(\mathbf{r} + \hat{\mathbf{y}}\Delta_x) \\ &= \sum_{\mathbf{G}} e^{i\mathbf{G}_y \Delta_x} V_{\mathbf{G}}^{(\text{lat})} e^{i\mathbf{G} \cdot \mathbf{r}} \\ &\approx \sum_{\mathbf{G}} (1 + iG_y \Delta_x) V_{\mathbf{G}}^{(\text{lat})} e^{i\mathbf{G} \cdot \mathbf{r}} \\ &= \sum_{\mathbf{G}} V_{\mathbf{G}}^{(\text{lat})} e^{i\mathbf{G} \cdot \mathbf{r}} \\ &\quad + i \sum_{q\mathbf{G}} \Delta_q V_{\mathbf{G}}^{(\text{lat})} G_y e^{i(\mathbf{G} \cdot \mathbf{r} + qx)}, \end{aligned} \quad (70)$$

to first order in the atomic displacement, so that the perturbation Hamiltonian caused by the edge roughness can be expressed as:

$$H^{(\text{LER})}(\mathbf{r}) = i \sum_{q\mathbf{G}} \Delta_q V_{\mathbf{G}}^{(\text{lat})} G_y e^{i(\mathbf{G} \cdot \mathbf{r} + qx)}. \quad (71)$$

Defining the wavefunctions:

$$\xi_{n,G_x,k_x}(\mathbf{R}) = \frac{1}{A_c^{1/2}} \sum_{\mathbf{G}_{\perp}} u_{k_x,\mathbf{G}}^{(n)} e^{i\mathbf{G}_{\perp} \cdot \mathbf{R}}, \quad (72)$$

the matrix element associated with a transition from a state in band n and wavenumber k_x to a state in band n' and

wavenumber k'_x can be written as:

$$\begin{aligned} V_{k_x, k'_x, n, n'}^{(\text{LER})} &= i \sum_{G_x G'_x G''_x} \sum_{\mathbf{G}_\perp} G_y \Delta_{k_x - k'_x + G_x - G'_x + G''_x} V_{G''_x, \mathbf{G}_\perp}^{(\text{lat})} \\ &\times \int d\mathbf{R} \xi_{n', k'_x, G'_x}^*(\mathbf{R}) e^{i\mathbf{G}_\perp \cdot \mathbf{R}} \xi_{n, k_x, G_x}(\mathbf{R}). \end{aligned} \quad (73)$$

With the usual reshuffling of the dummy summation wavevectors we can rewrite this expression in the more convenient form:

$$\begin{aligned} V_{k_x, k'_x, n, n'}^{(\text{LER})} &= i \sum_{G_x G'_x G''_x} \sum_{\mathbf{G}_\perp} G_y \Delta_{k_x - k'_x + G'_x} V_{G''_x, \mathbf{G}_\perp}^{(\text{lat})} \\ &\times \int d\mathbf{R} \xi_{n', k'_x, G_x - G'_x + G''_x}^*(\mathbf{R}) e^{i\mathbf{G}_\perp \cdot \mathbf{R}} \xi_{n, k_x, G_x}(\mathbf{R}) \\ &= i \sum_{G_x G'_x G''_x} \sum_{\mathbf{G}_\perp G''_\perp} G_y \Delta_{k_x - k'_x + G'_x} V_{\mathbf{G}}^{(\text{lat})} \\ &\times u_{k'_x, G_x - G'_x + G''_x, \mathbf{G}_\perp + G''_\perp}^{(n')*} u_{k_x, G'_x}^{(n)} \\ &= \sum_{G'_x} \Delta_{k_x - k'_x + G'_x} \Gamma_{k_x, k'_x, n, n'; G'_x}^{(\text{GPN})}. \end{aligned} \quad (74)$$

Recognizing the fast decay of Δ_q with increasing q we can ignore *Umklapp* terms with $G'_x \neq 0$, so that the matrix element simplifies to (renaming $\mathbf{G}'' \rightarrow \mathbf{G}'$):

$$\begin{aligned} V_{k_x, k'_x, n, n'}^{(\text{LER})} &\approx i \Delta_{k_x - k'_x} \sum_{G_x G'_x} \sum_{\mathbf{G}_\perp} G_y V_{G'_x, \mathbf{G}_\perp}^{(\text{lat})} \\ &\times \int d\mathbf{R} \xi_{n', k'_x, G_x + G'_x}^*(\mathbf{R}) e^{i\mathbf{G}_\perp \cdot \mathbf{R}} \xi_{n, k_x, G_x}(\mathbf{R}) \\ &= i \Delta_{k_x - k'_x} \sum_{\mathbf{G} \mathbf{G}'} G_y V_{\mathbf{G}}^{(\text{lat})} u_{\mathbf{G} + \mathbf{G}', k'_x}^{(n')*} u_{\mathbf{G}', k_x}^{(n)} \\ &= \Delta_{k_x - k'_x} \Gamma_{k_x, k'_x, n, n'; 0}^{(\text{GPN})}, \end{aligned} \quad (75)$$

where $\Gamma_{k_x, k'_x, n, n'; 0}^{(\text{GPN})}$ represents a ‘generalized Prange–Nee’ matrix element. Using the wavefunctions ξ_{n, k_x} defined by (63) we reach an approximate form convenient for numerical evaluation:

$$\begin{aligned} V_{k_x, k'_x, n, n'}^{(\text{LER})} &\approx i \Delta_{k_x - k'_x} \sum_{\mathbf{G}_\perp} G_y V_{G_x = 0, \mathbf{G}_\perp}^{(\text{lat})} \\ &\times \int d\mathbf{R} \xi_{n', k'_x}^*(\mathbf{R}) e^{i\mathbf{G}_\perp \cdot \mathbf{R}} \xi_{n, k_x}(\mathbf{R}) \\ &= i \Delta_{k_x - k'_x} \sum_{\mathbf{G}_\perp} G_y V_{\mathbf{G}}^{(\text{lat})} \tilde{\mathcal{I}}_{k_x, k'_x, n, n'}(\mathbf{G}_\perp), \end{aligned} \quad (76)$$

having used in the last step the expression for the overlap factor:

$$\tilde{\mathcal{I}}_{k_x, k'_x, n, n'}(\mathbf{Q}) = \int d\mathbf{R} \xi_{n', k'_x}^*(\mathbf{R}) e^{i\mathbf{Q} \cdot \mathbf{R}} \xi_{n, k_x}(\mathbf{R}). \quad (77)$$

Note that in simpler models which ignore Bloch-functions effects [23, 156] the reciprocal-lattice vectors disappear and the scattering rate for edge-roughness-induced processes vanishes for inter-subband transitions, since, whenever only one final state $k'_x = -k_x$ is assumed to exist, $\tilde{\mathcal{I}}_{k_x, -k_x, n, n'}(0) = \delta_{n, n'}$.

The expression above, (76), represents the case of roughness correlated at both edges. Such a correlated

roughness (representing a ‘snaking’ ribbon with constant width) can induce only a moderate mode-mixing, but no intra-subband transitions. Therefore we should consider the more interesting case of anti-correlated and uncorrelated edge roughness. These cases can be treated by explicitly adding or removing atomic lines, as demanded by the fact that the addition or the deletion of an atomic line in an AGNR can have a dramatically different effect in view of the claromatic dependence of the AGNR bandgap (see figure 5). This claromaticity also makes us expect a ‘noisy’ width-dependence, since for each different ribbon a change of width will cause a dramatically different change of the subband energy. More importantly, questions should be raised about the validity of the perturbation theory (the Born and independent-collisions approximation) we are employing, since large matrix elements will imply scattering lengths shorter than the electronic wavelength even in the presence of ‘dilute’ roughness. As we shall see from the large magnitude of the matrix elements, a correct approach—already mentioned above—would have to rely on the calculation of the transmission probability across a ribbon of varying width, as done by Tseng *et al* [83], by Betti and co-workers [25], and others [108, 158–163] and, even in the context of GNR-based FETs, by Luisier and Klimeck [164]. Therefore, our results should be interpreted as providing a qualitative trend and clearly indicating most definitely that LER scattering plays a huge role in controlling electronic transport in AGNRs, but their quantitative correctness—and especially their applicability to transport calculations—should be questioned.

Therefore, in the second approach we have anticipated (of adding/removing atomic lines in order to deal with anti- and uncorrelated roughness) we consider the change of the lattice (pseudo) potential caused by removing (–) or adding (+) only a single line of C atoms (and terminating H atoms) from the ‘left’ and ‘right’ edges (where ‘left’ and ‘right’ edges have been defined in section 2.4), obtaining scattering potentials $\langle \Delta V^{(\text{left}, \pm)}(\mathbf{R}) \rangle$ and $\langle \Delta V^{(\text{right}, \pm)}(\mathbf{R}) \rangle$ of the form:

$$\begin{aligned} \langle \Delta V^{(\text{left/right}, \pm)}(\mathbf{R}) \rangle &= \sum_{\mathbf{G}_\perp} e^{i\mathbf{G}_\perp \cdot \mathbf{R}} \\ &\times \left[\sum_{\alpha} e^{-i\mathbf{G}_\perp \cdot \mathbf{r}_\alpha} V_{G_x=0, \mathbf{G}_\perp}^{(\alpha)} - \sum_{\alpha'} e^{-i\mathbf{G}_\perp \cdot \mathbf{r}_{\alpha'}} V_{G_x=0, \mathbf{G}_\perp}^{(\alpha')} \right]. \end{aligned} \quad (78)$$

The notation $\langle \dots \rangle$ denotes the average over the length of the unit cell along the ‘axial’ direction x , since we have considered only the $G_x = 0$ terms assuming $\Lambda \gg 3a_0$. This amounts to assuming that the roughness has a correlation length much longer than the length of a unit cell along the axial direction. Therefore we can view this expression as the lattice average of the perturbation Hamiltonian caused by this change of the lattice potential:

$$\begin{aligned} H^{(\text{LER})}(\mathbf{r}) &= \sum_{\mathbf{G} \mathbf{Q}} e^{i(\mathbf{G} \cdot \mathbf{r} + \mathbf{Q} \cdot \mathbf{R})} \\ &\times \left[\sum_{\alpha} e^{-i\mathbf{G} \cdot \mathbf{r}_\alpha} V_{\mathbf{G}}^{(\alpha)} - \sum_{\alpha'} e^{-i\mathbf{G} \cdot \mathbf{r}_{\alpha'}} V_{\mathbf{G}}^{(\alpha')} \right]. \end{aligned} \quad (79)$$

In these equations the index α runs over the atoms added (that is, the H atom in the new positions) and the index α' runs over the atoms deleted from the structure (i.e., the C atom removed together with the H atom saturating its dangling bond). The expression given by (78) can be viewed as caused by a sideward shift $\Delta = a_0/\sqrt{3}$ of the left or right edge.

We ignore the case of abrupt variations of the AGNR-width by more than a single atomic line at each edge, since these would correspond to (hopefully) unrealistically large values of $\langle |\Delta_{q=0}|^2 \rangle^{1/2}$. Thus, the matrix element associated with the roughness at the two edges can be written as:

$$\begin{aligned} |V_{k'_x, k_x, n', n}^{(\text{LER})(c)}|^2 &= \frac{1}{4} \langle |\Delta_{k_x - k'_x}|^2 \rangle \\ &\times \left\{ \left| \mathcal{I}_{k'_x, k_x, n', n}^{(\text{LER}, \text{left}, +)} + \mathcal{I}_{k'_x, k_x, n', n}^{(\text{LER}, \text{right}, -)} \right|^2 \right. \\ &\quad \left. + \left| \mathcal{I}_{k'_x, k_x, n', n}^{(\text{LER}, \text{left}, -)} + \mathcal{I}_{k'_x, k_x, n', n}^{(\text{LER}, \text{right}, +)} \right|^2 \right\}, \end{aligned} \quad (80)$$

for correlated roughness, since adding/removing atoms to/from one edge and removing/adding atoms from/to the other edge is equivalent to shifting the ribbon rigidly along the y direction. Similarly,

$$\begin{aligned} |V_{k'_x, k_x, n', n}^{(\text{LER})(ac)}|^2 &= \frac{1}{4} \langle |\Delta_{k_x - k'_x}|^2 \rangle \\ &\times \left\{ \left| \mathcal{I}_{k'_x, k_x, n', n}^{(\text{LER}, \text{left}, +)} + \mathcal{I}_{k'_x, k_x, n', n}^{(\text{LER}, \text{right}, +)} \right|^2 \right. \\ &\quad \left. + \left| \mathcal{I}_{k'_x, k_x, n', n}^{(\text{LER}, \text{left}, -)} + \mathcal{I}_{k'_x, k_x, n', n}^{(\text{LER}, \text{right}, -)} \right|^2 \right\}, \end{aligned} \quad (81)$$

is the squared matrix element associated with anti-correlated roughness, since this expression corresponds to the simultaneous addition/removal of atoms to/from both edges. Finally,

$$\begin{aligned} |V_{k'_x, k_x, n', n}^{(\text{LER})(uc)}|^2 &= \frac{1}{4} \left\{ \langle |\Delta_{k_x - k'_x}^{(\text{left})}|^2 \rangle \left[\left| \mathcal{I}_{k'_x, k_x, n', n}^{(\text{LER}, \text{left}, +)} \right|^2 + \left| \mathcal{I}_{k'_x, k_x, n', n}^{(\text{LER}, \text{left}, -)} \right|^2 \right] \right. \\ &\quad \left. + \langle |\Delta_{k_x - k'_x}^{(\text{right})}|^2 \rangle \left[\left| \mathcal{I}_{k'_x, k_x, n', n}^{(\text{LER}, \text{right}, +)} \right|^2 + \left| \mathcal{I}_{k'_x, k_x, n', n}^{(\text{LER}, \text{right}, -)} \right|^2 \right] \right\}, \end{aligned} \quad (82)$$

is the squared matrix element for uncorrelated roughness since it expresses the effect of uncorrelated additions and removal of atoms to/from each edge with different roughness power-spectra at each edge. In these expressions the form factors $\mathcal{I}_{k'_x, k_x, n', n}^{(\text{LER}, \text{left}, \pm)}$ and $\mathcal{I}_{k'_x, k_x, n', n}^{(\text{LER}, \text{right}, \pm)}$ represent integrals of the form

$$\mathcal{I}_{k'_x, k_x, n', n}^{(\text{LER}, l/r, \pm)} = \int d\mathbf{R} \zeta_{n', k'_x}^*(\mathbf{R}) \frac{d\langle V^{(l/r, \pm)}(\mathbf{R}) \rangle}{dy} \zeta_{n, k_x}(\mathbf{R}) \quad (83)$$

where the perturbation potentials $d\langle V^{(l/r, \pm)}(\mathbf{R}) \rangle/dy$ are given by the difference pseudopotentials obtained by inserting (+) or deleting (-) an atomic layer at the left (l) or right (r) edge, respectively. Here $d\langle V^{(\text{left})}(\mathbf{R}) \rangle/dy = [2/\sqrt{3}a_0]\Delta V^{(\text{left})}(\mathbf{R})$ and $d\langle V^{(\text{right})}(\mathbf{R}) \rangle/dy = [2/\sqrt{3}a_0]\Delta V^{(\text{right})}(\mathbf{R})$ are the ‘left’ and ‘right’ edge roughness potentials normalized to the

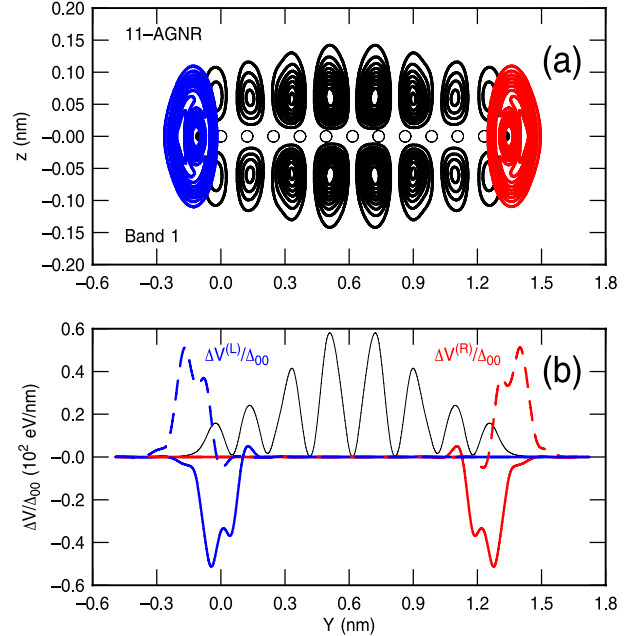


Figure 22. (a) Contour plot of the cell-averaged squared ground-state conduction band wavefunction (thin black lines) and LER scattering potentials due to the insertion of an atomic line at the left (thick blue lines) and right (thick red contours) edges for an 11-AGNR. Open circles underneath the contour lines represent C atoms, solid circles (partially hidden by the contours of the LER potential) H atoms. (b) The same quantities plotted in the top frame, but now averaged over the thickness of the ribbon. In this case, both scattering potentials due to the insertion (solid lines) or deletion (dashed lines) of an atomic line have been plotted. (Adapted with permission from [33], Copyright (2011) by the American Institute of Physics.)

displacement amplitude $\sqrt{3}a_0/2$ from which they have been calculated. These potentials, as well the ground-state conduction band wavefunctions at $k_x = 0$, are shown in figure 22.

Figure 23 shows the squared matrix element as a function of ribbon width for the case of uncorrelated roughness. If we ignore the effect of claromaticity, for wide AGNRs we expect a W^{-4} dependence, since in a simple analytical approximation the dispersion of the ribbons can be expressed as:

$$E_n(k_x) \approx \hbar v_F \sqrt{k_n^2 + k_x^2}, \quad (84)$$

where k_n is the quantized wavenumber along the width of the ribbon for band n given by $\eta n\pi/W$, where η is a number of the order of unity which varies depending on the model chosen [2, 23, 108, 156]. If additional effects (to be discussed momentarily) are ignored, in analogy with Sasaki’s expression, (67), we expect for the matrix element due to line-edge roughness:

$$V_{0,0}^{(\text{LER})(uc)} \approx \frac{dE_n(k_x = 0)}{dW} \approx -\frac{\eta \hbar v_F \pi n}{W^2}, \quad (85)$$

hence the W^{-4} dependence for the squared matrix element. This is indeed observed for the (2, 2) transitions (figure 23(b)) for $N_a = 3p$ AGNRs at the largest W we have considered, but it does not appear to be a general feature as a result of the

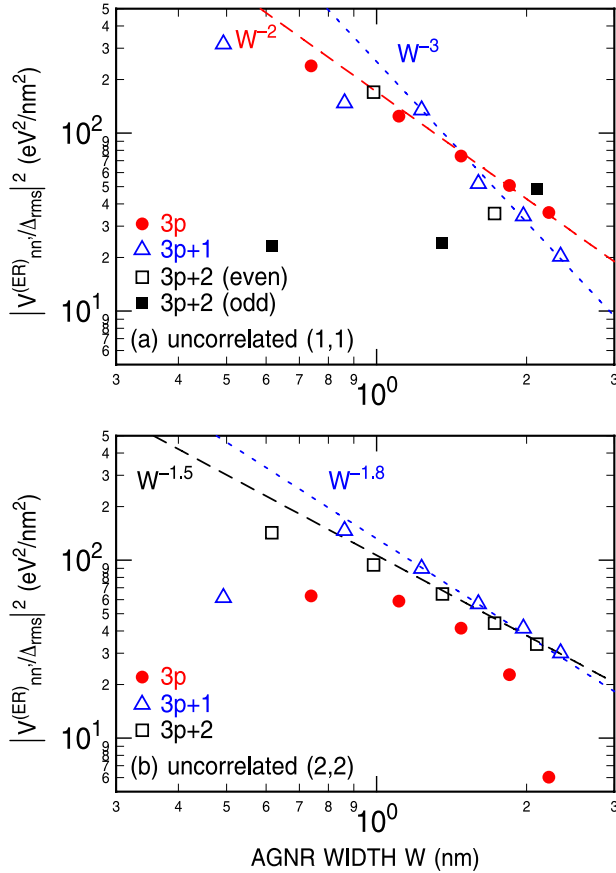


Figure 23. Squared magnitude of the generalized Prange-Nee edge-roughness matrix element at the zone-centre in the case of uncorrelated roughness for intraband transitions within the first (sub)band (labelled (1, 1), top frame) and for intraband transitions within the second subband (labelled (2, 2), bottom frame). Note the strong claromatic dependence clearly seen—especially in the bottom frame—in the ‘quasi-periodic’ oscillation of the matrix element as we cycle through $3p$ -, $(3p + 1)$ -, and $(3p + 2)$ -wide AGNRs. For the (1, 1) matrix element, a much different power-law dependence is observed for each different claromatic type of the ribbons. An explanation for the anomalously small (1, 1) matrix elements obtained for narrowest odd $(3p + 2)$ -AGNRs is given in [33]. (Reproduced with permission from [33], Copyright (2011) by the American Institute of Physics.)

claromaticity of the AGNR bandgap not being captured by the simple model described by (84).

Note in figure 23 the claromaticity observed especially at small W and the magnitude of the squared matrix element, about two orders of magnitude larger than the magnitude (of the order of 1 eV nm^{-1} for $W = 1 \text{ nm}$) expected from (85). As discussed in the opening paragraph of this section, both features can be understood from the claromatic behaviour of AGNRs (figure 5). This effect has not been considered in previous mobility studies based on a ‘smooth’ analytic band structure and associated roughness models [23, 156], but is obviously implicitly present in atomistic simulations [25, 76, 108, 143, 164, 165], and may explain the low electron mobility observed experimentally in narrow ribbons [29, 166], much lower than in large graphene sheets [167]. Thus, perfect control of the nanoribbon width—with whatever process

one may envision, such as bottom-up synthesis [168] or chemically ‘unzipping’ CNTs [169, 170]—will be necessary in order to obtain AGNRs with good transport properties, at least in the diffusive (long GNRs) regime. How crucial our observations really are in practice is still hard to assess, since our discussion is valid only in the diffusive regime. In the quasi-ballistic regime the quantum approaches presented in [25, 83, 108, 158–163] should be used, since electronic transport in rough (or disordered) GNRs may be affected by various confinement effects depending on the electron coherence length [167], by Anderson localization [160, 162], as also discussed in the review articles by Cresti *et al* [171], Mucciolo and Lowenkopf [3] or by transport among quantum dots formed by lithographically-induced LER [172] or induced by nearby charged impurities [4, 173, 174]. Finally, while we have considered free-standing ribbons, we should keep in mind possible interactions with the substrate which may give raise to strong effects related to remote coupling with polar substrate phonons [34, 24], as discussed in section 5 in the case of supported graphene.

Finally, the numerical evaluation of the LER scattering rate can be performed using a 1D discretization:

$$\frac{1}{\tau_n^{(\text{LER})}(k_x)} = \frac{2\pi}{\hbar} \sum'_{jn'} \frac{1}{2\pi} \left| \frac{dE_{n'j}}{dk_x} \right|^{-1} \left| V_{k_{nj}, k_x, n', n}^{(\text{LER})} \right|^2, \quad (86)$$

and similarly for the velocity relaxation rate,

$$\frac{1}{\tau_{nv}^{(\text{LER})}(k_x)} = \frac{2\pi}{\hbar} \sum'_{jn'} \frac{1}{2\pi} \left| \frac{dE_{n'j}}{dk_x} \right|^{-1} \times \left| V_{k_{nj}, k_x, n', n}^{(\text{LER})} \right|^2 \left[1 - \frac{v_{n'j}}{v_n(k_x)} \right]. \quad (87)$$

This requires a discretization of the 1D BZ into segments of length Δk_x , labelled by an integer j centred around the wavenumber k_{nj} with central energy E_{nj} given by the dispersion $E_n(k_{nj})$ in band n . We denote the central derivative $dE_n(k_{nj})/dk_{nj}$ by dE_{nj}/dk_x and group velocity by $v_{nj} = dE_{nj}/dk_x/\hbar$. As indicated before, the ‘primed’ sum means that only energy-conserving segments (i.e., such that $E_{n'j} - (dE_{n'j}/dk_x)\Delta k_x/2 \leq E_n(k_x) < E_{n'j} + (dE_{n'j}/dk_x)\Delta k_x/2$) should be considered. Note that in the sum appearing in (86) the initial state itself must be excluded, since this process amounts to a first-order self-energy renormalization of the electron dispersion. Also, the ‘microscopic’ velocity relaxation rate defined by (87)—different from the relaxation rate used when performing mobility calculations—may take negative values in the presence of strong forward inter-subband scattering to states with larger group velocity. This reflects the fact that the electron momentum along the transport direction may increase as a result of forward inelastic absorption processes over a limited range of electron kinetic energy. This is a frequent occurrence for 1D processes with matrix elements decreasing with increasing wavenumber transfer, which is the case here because of the dependence of $\langle |\Delta_q|^2 \rangle$ on q . This indeed happens in AGNRs at large electron kinetic energies.

Figure 24 shows the large magnitude of the Prange–Nee component of the LER scattering rates (top) and velocity

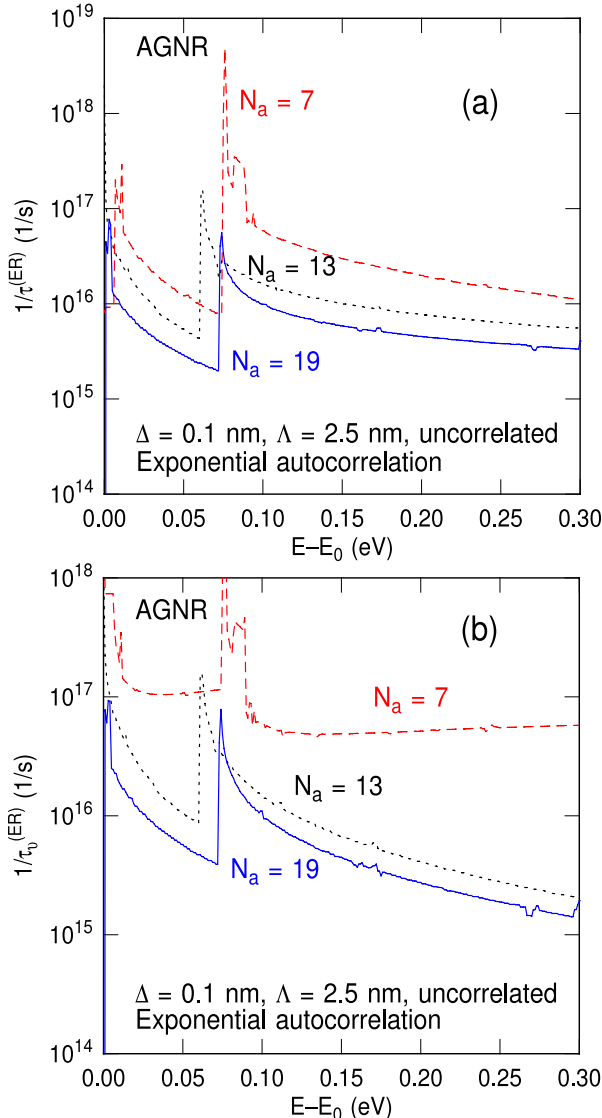


Figure 24. (a) Line-edge roughness scattering rate (Prange-Nee component only) as a function of electron energy (measured from the bottom of the conduction band) in three H-terminated armchair-edge GNRs with widths given by $N_a = 3p + 1$ atomic lines ($N_a = 7, 13$, and 19). A total number of six subbands has been employed, together with an exponential autocorrelation. Note the very large scattering rates originating from the chirality-dependence of the gap shown in figure 5. (b) As in the top frame, but showing the velocity relaxation time. Note that for the 7-AGNR at large energies the relaxation rate increases as a result of inter-subband scattering to the lower-velocity, higher-density of states second subband. Scattering and relaxation rates so large obviously have implications on the electron mobility of narrow AGNRs, but their magnitude points to the failure of perturbation theory (Born approximation) and, more appropriately, of the existence of extended Bloch states in narrow AGNRs with rough edges. (Reproduced with permission from [33], Copyright (2011) by the American Institute of Physics.)

relaxation rates (bottom) in 7-, 13-, and 19-AGNRs. The magnitude of these rates hints at a failure of perturbation theory, as mentioned above and amply discussed in [53]. Nevertheless, if we were willing to take these quantitative results seriously, from the magnitude of the rates shown

in this figure we could crudely estimate an LER-limited electron mobility $\mu^{\text{(LER)}}$ in narrow AGNRs of the order of $1 \text{ cm}^2 \text{ V}^{-1} \text{ s}^{-1}$, or even less, assuming naïvely $\mu^{\text{(LER)}} \sim e\tau_v^{\text{(LER)}}/m^*$, $m^* \sim 0.1 \text{ m}$ being the effective mass in the lowest energy band of AGNRs with widths in the range 2 to 3 nm. This is in rough qualitative agreement with recent experimental observations [29] and is consistent with the conclusion drawn by Gallagher *et al* [154]. So, while clearly the numerical values shown in figure 24 cannot be taken seriously, nevertheless they stress the dramatic importance of edge disorder in AGNRs [108, 172–174], with the likely implication that transport in narrow and rough AGNRs does not occur via extended states. What is most worrisome is the fact that the ‘slower’ width-dependence shown in figure 23 for any claromaticity, if maintained at widths larger than what we can numerically afford, implies that LER scattering may remain very strong—stronger than in NWs or thin films of similar dimensions and roughness—in wider ribbons. Indeed, while a higher mobility ($100\text{--}500 \text{ cm}^2 \text{ V}^{-1} \text{ s}^{-1}$) has been measured in ribbons of width larger than about 20 nm [175], at low temperatures the higher-mobility samples exhibited a thermally-activated conductivity, suggesting the existence of localization in ‘puddles’ (although in this case probably induced by charged impurities in the substrate).

5. Additional scattering processes in supported graphene

An additional consideration regarding real applications of graphene, such as graphene field-effect transistors (GFETs), is that the graphene sheet is physically supported by an insulating polar substrate such as SiO_2 . However, the carrier mobility is reduced by an order of magnitude, from $\sim 10^5$ to $10^4 \text{ cm}^2 \text{ V}^{-1} \text{ s}^{-1}$ [100], as a result of additional external scattering mechanisms introduced by the substrate. This reduction in carrier mobility is further exacerbated in top-gated structures in which a thin layer of a high- κ polar dielectric, such as HfO_2 or Al_2O_3 , is deposited on the graphene sheet [176–180]. The external scattering sources are commonly believed to be charge traps, surface roughness, and remote polar optical phonons. In particular, the latter poses a significant problem for electron transport at high temperature. This issue has been extensively investigated in the past [34, 35, 37]. Here we follow [38–40], differing from previous work mainly in the way full dynamic screening effects are accounted for, which follows similar work on the Si/high- κ -insulator MOS structures of [181].

5.1. Remote-phonon scattering

In metal-oxide insulators such as SiO_2 and HfO_2 , the polarizability of the ionic metal-oxide bond typically dominates the dielectric response of the material. Associated with the ionicity of the bonds are bulk dipoles, which generate on the substrate surface a fringing electric field that can interact with charged particles in close proximity at multiple characteristic frequencies. The characteristic frequency of these dipoles is usually determined by the

harmonic motion of the ionic bonds, i.e. the bulk longitudinal optical phonons, as well as the electrodynamic boundary condition at the insulator–vacuum interface. The resultant surface polar excitations can exchange energy and momentum with nearby electrons.

The remote interaction of low-energy electrons with these polar optical phonons, sometimes also known as Fuchs–Kliewer (FK) surface optical (SO) phonons [182], near the surface of the insulator was first studied by Wang and Mahan [183] in their analysis of inelastic electron scattering by surface excitations in photoemission studies. This idea, also known in the literature as remote-phonon scattering, was later applied by Hess and Vogl [184], and then by Moore and Ferry [185], to the problem of electron mobility degradation by remote-phonon scattering in Si inversion layers near the Si–SiO₂ interface in Si MOSFETs. Fischetti and co-workers [181] later studied the effects of remote-phonon scattering in MOS structures and found that high- κ oxide layers have a significant effect on carrier mobility in Si and Ge. They found that, in degenerate semiconductors, the collective dynamical charge density response of the carriers (plasmons) couples with the motion of the SO phonons, forming hybrid interfacial plasmon–phonon (IPP) excitations. This plasmonic coupling naturally leads to the phenomenon of dynamic screening/anti-screening of the interaction of the SO phonons with individual carriers. The method was later extended by Xiu to study remote-phonon scattering in Si nanowires [186].

In supported graphene, the graphene–substrate gap size is very small, typically around 0.3–0.4 nm [187]. Given that the electrons are more or less localized within the graphene sheet, they interact very strongly with the SO phonons. Thus, remote scattering by the insulator surface excitations is believed to be one of the primary mechanisms for mobility degradation, especially at high temperatures, in graphene and the related carbon nanotubes. Experiments involving current saturation behaviour imply that this saturation is largely determined by remote-phonon scattering [188]. The subject of remote-phonon scattering in graphene and carbon nanotubes has also been broached in the recent past. Rotkin and co-workers studied remote phonon-mediated heat dissipation and low-field mobility in carbon nanotubes [35, 36], Fratini and Guinea computed the upper bounds to mobility in graphene imposed by remote phonons [34], while Scharf *et al* have investigated the effect of remote-phonon scattering on the optical conductivity of graphene [6].

The basic approach used in the aforementioned theoretical studies [34–36] ignores the coupling between the collective response of the carriers and the SO phonons. In the seminal work on remote-phonon scattering in graphene by Fratini and Guinea [34], it was pointed out that the scattering rates with bare SO phonons yields a remote-phonon-limited mobility that was too low compared to experimental results. To remedy this flaw, an empirical Thomas–Fermi screening factor is sometimes used to weaken the electron–phonon coupling coefficient [34, 189]. This approach is somewhat ad hoc and predicts that the remote-phonon-limited mobility decreases with carrier density, a result contradicted by

the experimental data of Zou and co-workers [190], who estimated that the remote-phonon-limited mobility increases in HfO₂-capped graphene with electron density. As we shall see later, this contradiction indicates a flaw in the screening model. Therefore, to understand the screening phenomenon, it is necessary to consider the charge density response of the graphene to the electric field created by the SO phonons.

In the absence of any induced charge, the dispersion of the SO phonons is determined from the roots of the secular equation $\epsilon_0 + \epsilon_{\text{ox}}(\omega) = 0$, which we obtain by matching the electric field and displacement across the substrate–vacuum interface. Here ϵ_0 is the permittivity of vacuum, while $\epsilon_{\text{ox}}(\omega)$ is the frequency-dependent dielectric function of the substrate. It is assumed that the dielectric function of the oxide can be written in the generalized Lyddane–Sachs–Teller form [181], i.e.

$$\epsilon_{\text{ox}}(\omega) = \epsilon_{\text{ox}}(\infty) \frac{(\omega^2 - \omega_{\text{LO}1}^2)(\omega^2 - \omega_{\text{LO}2}^2)}{(\omega^2 - \omega_{\text{TO}1}^2)(\omega^2 - \omega_{\text{TO}2}^2)}, \quad (88)$$

where $\omega_{\text{LO}i}$ and $\omega_{\text{TO}i}$ are respectively the longitudinal and transverse optical phonon frequency for $i = 1$ and 2 assuming that two dominant TO modes are present. Hence, the roots of the secular equation are $\omega_{\text{SO}1}$ and $\omega_{\text{SO}2}$. For example, $\omega_{\text{SO}1}$ and $\omega_{\text{SO}2}$ in SiO₂ are around 60 and 147 meV, respectively.

However, the fringing electric field from the SO phonons also couples electromagnetically to doped graphene, inducing a charge density (optical) response. Thus, it is also necessary to take into account the electric displacement discontinuity created by the induced charge in the graphene sheet. This alters the dispersion, and the secular equation becomes:

$$[\epsilon_0 + \epsilon_{\text{ox}}(\omega)] \left[1 - (1 - e^{-2Qd}) \frac{e^2 \Pi(Q, \omega)}{2\epsilon_0 Q} \right] - \frac{e^2 \Pi(Q, \omega)}{Q} e^{-2Qd} = 0, \quad (89)$$

where $\Pi(Q, \omega)$ is the dynamic polarizability charge and d is the size of the substrate–graphene gap. Note that, in the $d \rightarrow \infty$ limit, the secular equation becomes:

$$[\epsilon_0 + \epsilon_{\text{ox}}(\omega)] \left[1 - \frac{e^2 \Pi(Q, \omega)}{2\epsilon_0 Q} \right] = 0. \quad (90)$$

The first factor yields the dispersion of the isolated SO phonons ($\omega_{\text{SO}1}$ and $\omega_{\text{SO}2}$), while the second factor determines the graphene plasmon dispersion [$\omega_{\text{pl}}(Q)$], as expected. As a result of the coupling of the SO phonons with the polarization charge, which can be interpreted as the hybridization of the SO phonons with graphene plasmons, the resulting excitation energy acquires a wavevector (Q) dependence. We term these surface excitations ‘interfacial plasmon–phonon’ (IPP) modes. For each wavevector Q , there are three excitation frequencies ($\omega_Q^{(1)}$, $\omega_Q^{(2)}$ and $\omega_Q^{(3)}$) in supported SLG; in double-gated SLG, there are five IPP branches from the hybridization of the two SO phonon branches in the substrate oxide, two from the gate oxide and one from the graphene plasmons [40].

Apart from modifying the dispersion of the surface excitations, the hybridization also modifies the coupling of

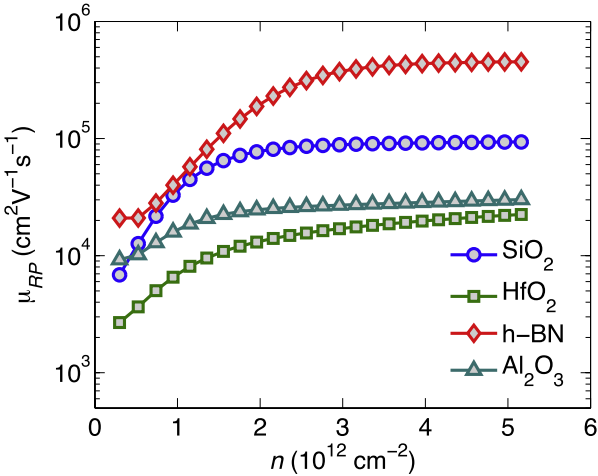


Figure 25. Calculated remote-phonon-limited electron mobility in graphene supported by SiO₂, HfO₂, h-BN, and Al₂O₃. A vacuum gap $d = 0.35$ nm between the graphene sheet and the insulating substrate has been assumed in all cases. The degradation of the mobility with increasing substrate dielectric constant is evident. (Reproduced from [39], Copyright (2012) by The American Physical Society.)

the surface excitations with single electrons. Here we avoid the rather involved derivation of the electron–IPP coupling coefficient—a derivation that can be found in [38–40]—and give only a qualitative description of the change. When plasmons are ignored, the electron–IPP coupling coefficient is derived from the quantization of the energy of the evanescent electric field at the vacuum–substrate interface. When plasmons are taken into account, the induced polarization charge modifies the electric field and hence alters the electron–IPP coupling. The change in the electron–IPP coupling depends on the frequencies of the uncoupled plasmon and SO phonons. When $\omega_{\text{pl}} < \omega_{\text{SO1}}$ at small Q , the electron–IPP coupling is enhanced, an effect that can be interpreted as dynamical *anti-screening* of the SO phonons; conversely, when $\omega_{\text{pl}} > \omega_{\text{SO1}}$ at large Q , the electron–IPP coupling is weakened or *screened*. The phenomenon of dynamical screening and anti-screening of the electron–IPP coupling and its dependence on the frequencies of the uncoupled plasmon and SO phonons is a feature not found in more phenomenological models [34] which assume that all SO phonon modes are screened (or weakened). In contrast to our interfacial plasmon–phonon theory, the phenomenological model assumes the screening of the SO phonons diverges in the long-wavelength limit ($Q \rightarrow 0$). This would have implications for the dependence of the electron mobility on carrier density.

We have computed the remote-phonon-limited mobility μ_{RP} for different substrates: SiO₂, HfO₂, h-BN, and Al₂O₃, assuming a vacuum gap of 0.35 nm between the graphene sheet and the substrate. Scattering only with the phonon component of the IPPs has been considered by calculating the phonon-content of each mode [38, 39], since scattering with the plasmon component does not directly dissipate momentum. The electrical conductivity is given by the

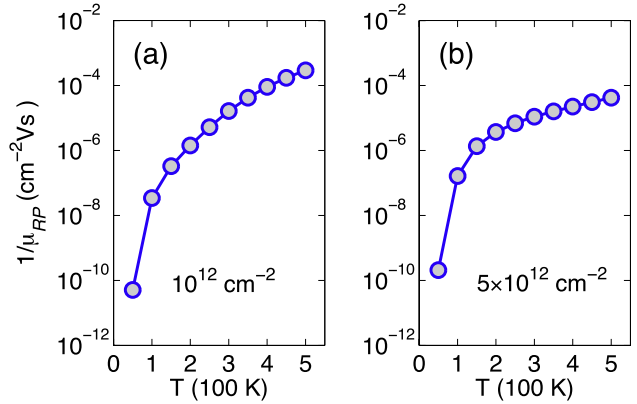


Figure 26. Temperature dependence of the inverse remote-phonon-limited mobility, $1/\mu_{\text{RP}}$, for electron sheet densities of $n = 10^{12} \text{ cm}^{-2}$ (a) and $n = 5 \times 10^{12} \text{ cm}^{-2}$ (b) for graphene on a SiO₂ substrate. (Reproduced from [39], Copyright (2012) by The American Physical Society.)

expression:

$$\sigma_{\text{RP}} = \frac{g_s g_v e^2}{4\pi\hbar k_B T^2} \int_0^\infty dE f(E - E_F) \times [1 - f(E - E_F)] \tau_{\text{RP}}(E) E, \quad (91)$$

where τ_{RP} is the remote-phonon-limited momentum relaxation time. The mobility μ_{RP} is simply taken to be the ratio of the conductivity and the charge density (n), i.e. $\mu_{\text{RP}} = \sigma_{\text{RP}}/(en)$. We plot μ_{RP} as a function of n in figure 25. At low n , μ_{RP} decreases as n becomes smaller, because proportionally more long wavelength, anti-screened remote phonons scatter the electrons. At high n , μ_{RP} is either a constant or weakly dependent on n , since most of the remote phonons are dynamically screened.

Figure 26 shows the plot of the inverse remote-phonon-limited mobility $1/\mu_{\text{RP}}$ for SiO₂ at $n = 10^{12}$ and $5 \times 10^{12} \text{ cm}^{-2}$ from $T = 50$ to 500 K. As expected, μ_{RP} increases rapidly as the temperature decreases, because the population of the IPP modes decreases with temperature. We also find that the increase in μ_{RP} with decreasing T is larger at $n = 10^{12} \text{ cm}^{-2}$. This is because at smaller n , there is a greater proportion of interband transitions via the scattering of electrons by weakly screened remote phonons. The momentum relaxation rate from interband transitions is significantly greater than that from intraband processes. At lower T , there are fewer states in the valence band available for interband transitions, as a result of more Pauli blocking. Therefore, the reduction in carrier scattering is due to the lower phonon population as well as the reduced availability of valence band states.

Our model also predicts a different dependence on carrier density. Figure 27 shows the remote-phonon-limited mobility with different screening models for (a) Al₂O₃ and (b) SiO₂. We compare μ_{RP} for no screening, static screening and dynamic screening. In the model without any screening, μ_{RP} is significantly lower because the unscreened remote phonons scatter the electrons more effectively. Another feature of the model is that μ_{RP} decreases with carrier density, scaling as

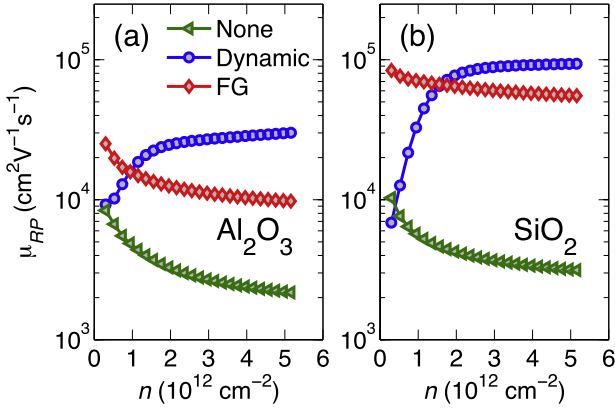


Figure 27. The remote-phonon-limited mobility computed using different screening models: no screening (triangles), dynamic (circles), and the approximation employed by Fratini and Guinea [34] (diamonds). The cases of graphene supported by Al_2O_3 (a) and SiO_2 (b) are illustrated. (Reproduced from [39], Copyright (2012) by The American Physical Society.)

$\mu_{RP} \propto n^{-\frac{1}{2}}$. When static screening is included, μ_{RP} is higher because the coupling with electrons is weaker. However, despite the inclusion of static screening, μ_{RP} decreases with n , as in the case without screening. This is because in the static screening model long-wavelength remote-phonon modes are more strongly screened than the short wavelength modes. In contrast, when we use the dynamic screening model, μ_{RP} increases with n , and is almost constant at large n . At small n , scattering by long-wavelength remote-phonon modes dominates. Unlike the static screening model, the long-wavelength modes in the IPP model are more weakly screened than shorter wavelength modes and interact more strongly with the electrons. Thus, as n increases, scattering by more strongly screened shorter wavelength modes dominates, and the mobility increases.

5.2. Charged-impurity scattering in supported and top-gated graphene

Another major source of remote scattering for electrons in graphene is constituted by charged impurities in the substrate. These can be due to adsorbates, such as water and/or photoresist and poly(methyl methacrylate) (PMMA) residues [191], or dangling bonds. Long-range scattering by screened charged impurities in monolayer graphene was first described by Ando [192], who found that the charged impurity-limited conductivity scales linearly with charge carrier density. Adam and co-workers also formulated a similar model of impurity-limited conductivity [45, 46]. This theory was directly verified by Chen *et al* [44] in low-temperature, electrical conductance measurements in UHV. Careful measurements of the electron mobility in graphene by Morozov *et al* [101] also suggest that charged-impurity scattering is the dominant limiting factor in carrier transport, even at room-temperature. A similar conclusion was reached by Hwang, Adam and Das Sarma in their theoretical analysis of experimental data [42].

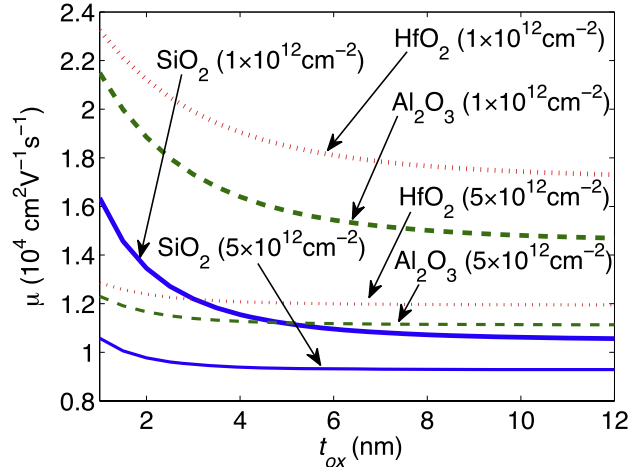


Figure 28. Dependence of the calculated impurity-limited electron mobility on top gate dielectric thickness for SiO_2 , Al_2O_3 , and HfO_2 at a carrier density $n = 10^{12}$ and 5×10^{12} cm\$^{-2}\$. (Reproduced from [47], Copyright (2012) by The American Physical Society.)

Given that long-range scattering by charged impurities is mediated by Coulomb interactions, it appears that the scattering can be modulated by modifying the dielectric environment around the graphene. Since the graphene electrons are confined to a plane of atomic thickness, the effective permittivity and impurity-limited mobility can be increased by overlaying the graphene with a high-\$\kappa\$ liquid [193, 194] or a solid such as ice [195].

In more realistic graphene-based transistor structures, the graphene is encased between a Si/SiO₂ substrate and a high-\$\kappa\$ gate insulator such as HfO₂ [190] or Al₂O₃ [179] of finite thickness, which offers better local electrostatic control and is necessary for the large-scale integration of graphene. Fallahazad *et al* [196, 197] found that as the gate insulator becomes thinner, the carrier mobility increases. This mobility improvement cannot be explained by the simple models of Ando [192] and Adam *et al* [45, 46]. Taking into account the more complicated layered geometry and the image charge the dependence of the carrier mobility on gate insulator thickness, we obtain the general expression for the Fourier transform of the scattering potential ϕ_Q^{scr} [47]:

$$\phi_Q^{\text{scr}} = \frac{e^2 G_Q}{1 - e^2 G_Q \Pi(Q)}, \quad (92)$$

where G_Q is the Fourier transform of the Green's function of the Poisson equation and $\Pi(Q)$ is the density-density response function (static polarizability). In the isotropic case, we have $G_Q = 1/2\epsilon Q$, where ϵ is the effective permittivity, and recover the expression by Ando:

$$\phi_Q^{\text{scr}} = \frac{e^2}{\epsilon(Q + Q_s)}, \quad (93)$$

where Q_s is the inverse screening length, given by $Q_s = e^2 E_F / (\epsilon \pi \hbar^2 v_F^2)$. Given the scattering potential, it is straightforward to calculate the impurity-limited carrier mobility.

In figure 28, we plot the dependence of the impurity-limited carrier mobility on the gate insulator thickness (t_{ox})

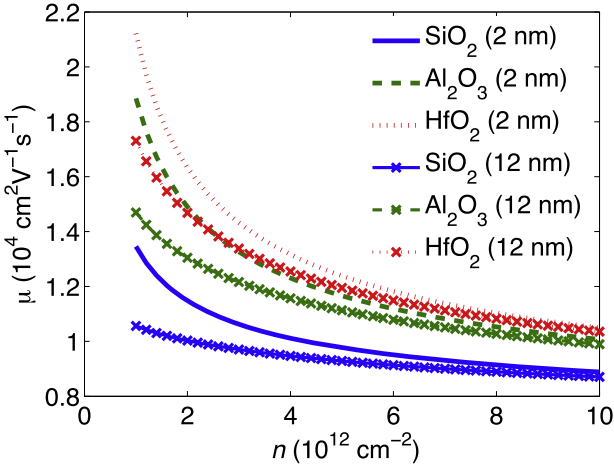


Figure 29. Dependence of the calculated impurity-limited electron mobility on carrier density. The mobility decreases with carrier density and the extent of the decrease is greater with smaller dielectric thickness. (Reproduced from [47], Copyright (2012) by The American Physical Society.)

for SiO_2 ($\kappa = 3.9$), Al_2O_3 ($\kappa = 12.5$), and HfO_2 ($\kappa = 22$) at $n = 10^{12}$ and $5 \times 10^{12} \text{ cm}^{-2}$, assuming an impurity concentration of $n_{\text{imp}} = 5 \times 10^{11} \text{ cm}^{-2}$. In general, the impurity-limited mobility μ is largest for HfO_2 and smallest for SiO_2 , because the former has the largest permittivity and screens the impurity charge most effectively. At small t_{ox} , screening by the metal layer becomes more important, since the image charge of the impurity is closer to the graphene sheet and reduces the effective scattering strength of the impurity. Thus, in figure 28, μ increases as t_{ox} decreases.

Comparing the trends in figure 28 for $n = 10^{12} \text{ cm}^{-2}$ and $n = 5 \times 10^{12} \text{ cm}^{-2}$, we find that the change in μ with respect to t_{ox} is larger for $n = 10^{12} \text{ cm}^{-2}$. This implies that screening by the gate insulator is more effective at low carrier densities. We also plot μ as a function of n for $t_{\text{ox}} = 2$ and 12 nm in figure 29. At large n , the dependence of μ on the gate insulator thickness is small. As n decreases, screening from the polarization charge diminishes and screening from the metal layer becomes more important. Hence, μ rises more rapidly as n decreases for $t_{\text{ox}} = 2 \text{ nm}$ than for $t_{\text{ox}} = 12 \text{ nm}$.

We conclude by presenting the overall effects of the ‘extrinsic’ scattering processes discussed in this and in the previous section. In figure 30 we show the total electron mobility as a function of top-oxide thickness for different carrier densities, calculated accounting for both remote-phonon scattering with the top and bottom dielectrics and impurity scattering assuming an impurity density of $5 \times 10^{11} \text{ cm}^{-2}$. The bottom insulator is always assumed to be SiO_2 and scattering with graphene bulk phonons is ignored, since its effect on transport is negligible compared to the effect of these extrinsic scattering processes (IPPs and impurity). The treatment of scattering with the IPPs present in this double-insulator geometry is quite laborious, since the various optical modes of the bottom and top insulators couple with graphene plasmons and among themselves, giving rise to five IPP modes [41]. In the figure note how, at

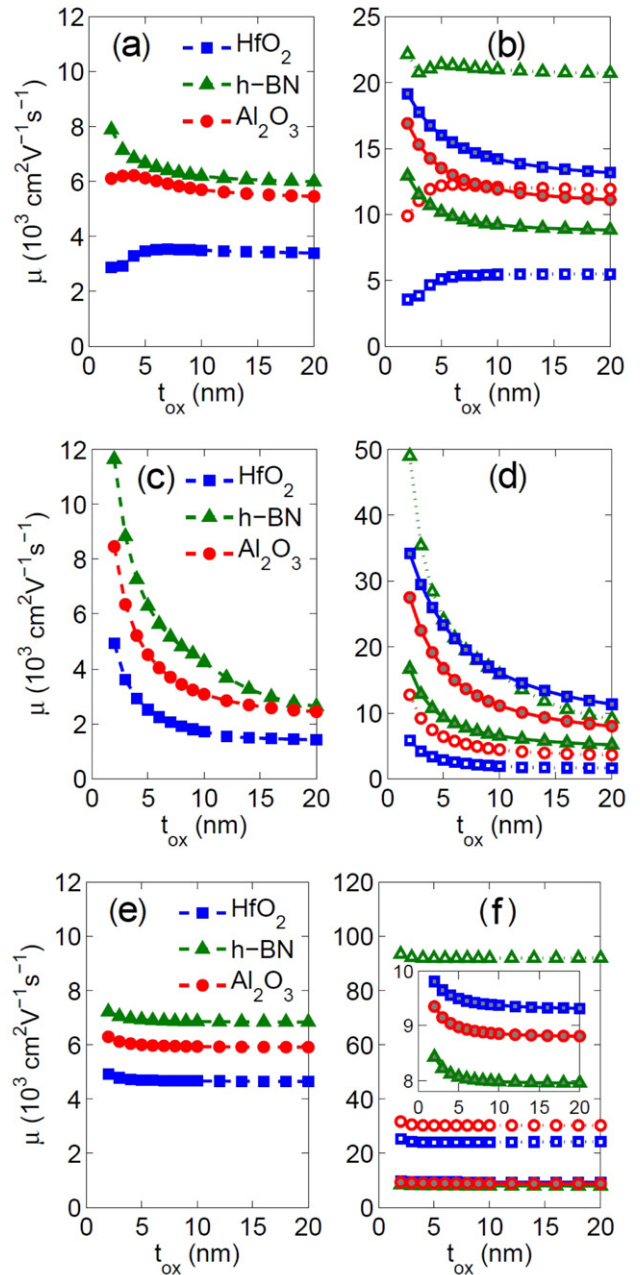


Figure 30. Dependence of the calculated total (left) and impurity-limited (solid symbols, right) and remote-phonon-limited (open symbols, right) electron mobility on top gate dielectric thickness for h-BN, Al_2O_3 , and HfO_2 . The impurity density is assumed to be SiO_2 . The inset in the bottom-right frame shows a magnified plot of the impurity-limited mobility. (Reproduced with permission from [41], Copyright (2013) by the American Institute of Physics.)

small carrier densities (10^{11} cm^{-2} , figures 30(a) and (b)), remote-phonon scattering dominates since the coupling to plasmons is weak and charged-impurity scattering is screened by the image charges in the gate metal. Hence the strong dependence on the thickness of the top insulator. At a density of 10^{12} cm^{-2} (figures 30(c) and (d)) coupling to plasmons becomes more important and the IPP-limited mobility for the higher- κ insulators (HfO_2 and Al_2O_3) actually decreases for

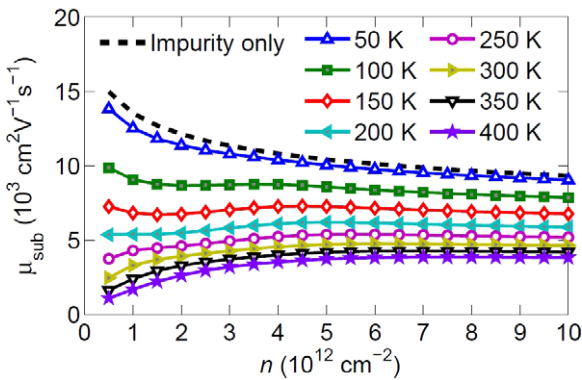


Figure 31. Dependence of the calculated total (charged-impurity and remote-phonon-limited) electron mobility on carrier density at several temperatures. The insulator is assumed to be a 100 nm-thick HfO_2 layer, the substrate SiO_2 , and the impurity density is assumed to be $5 \times 10^{11} \text{ cm}^{-2}$. The temperature dependence becomes weaker at higher carrier densities. (Reproduced with permission from [41], Copyright (2013) by the American Institute of Physics.)

a small top-oxide thickness, since the proximity of the gate metal weakens the dynamic screening of the remote-phonon potential. The total mobility, however, still decreases for a large top-oxide thickness, since remote-phonon scattering dominates. Not so at a large carrier density (10^{13} cm^{-2} , figures 30(e) and (f)), since charge-impurity scattering now becomes the dominant momentum relaxation process.

Finally, the dependence of the total electron mobility on carrier density for a 100 nm-thick HfO_2 top insulator at various temperatures is shown in figure 31 assuming again an impurity density of $5 \times 10^{11} \text{ cm}^{-2}$. A large thickness of the top oxide has been chosen in order to avoid the complicating issue of additional screening due to the image charges in the gate. Note that the total mobility at 50 K is very close to the impurity-limited mobility, showing that charged-impurity scattering dominates. But as the temperature increases, so does the contribution of the remote-phonon-limited mobility.

We should note that these results have been obtained using the low-temperature approximation for the dielectric function. This is expected to be a satisfactory approximation for graphene, especially in the strongly degenerate limit of high densities, but weaker screening of the impurity potential and a smaller polarizability of the image charges in the dielectrics may affect our results at high temperatures [198].

6. Conclusions

This partial review cannot provide a definite answer to the main question we have raised at the beginning of section 3, namely, whether or not the present graphene growth techniques have allowed us to observe the ultimate (and perhaps at present experimentally elusive) electronic-transport performance of single-layer graphene. Too many uncertainties remain in the measurement and calculation of the strength of the electron–phonon interaction. Yet, we have seen how a moderate consensus begins to emerge and we have shown that the use of the ‘judiciously calibrated’

empirical pseudopotentials yields a picture which is in approximate agreement with the properties observed so far regarding the low-field electron mobility and high-field saturated velocity. In addition, the combined use of DFT and EPs permits an almost ‘parameter free’ description of additional transport-related phenomena, such as the electron mobility in graphene supported by polar insulators—limited by remote-phonon and charged-impurity scattering—and in AGNRs—presumably strongly affected by line-edge roughness. These latter observations point to the increasing reliability of *ab initio* studies even when applied to electronic transport, a development we have stressed in our opening section. Moreover, within the narrow ‘VLSI focus’ of this review, they point out the well-known fact that significant obstacles remain before graphene could be employed in main-stream nanoelectronics logic applications: not only does manufacturing large-area high-quality graphene sheets remain elusive at present, but also intrinsic physical processes—remote-phonon scattering and LER—limit the performance of supported graphene and AGNRs, respectively. Yet, at the limit of device scaling we may face a situation in which we do not have a choice, since scaling the thickness of semiconductor bodies (or diameter of nanowire-based devices) may prevent us from keeping electrons confined in channels [199]. Thus, ‘intrinsically’ 2D materials such as graphene or transition-metal dichalcogenides—in which electrons are confined by ionic potentials rather than band-discontinuities—may offer the only solution.

Acknowledgments

We are grateful to Professor Eric Pop, to Vicent Dorgan and Andrey Serov for many constructive discussions, and to Dr William G Vandenberghe for having critically read the manuscript. Portions of this work have been financially supported by the South West Academy of Nanotechnology (SWAN), Task 4.3 Theme 2400.011.

References

- [1] Ando T, Fowler A B and Stern F 1982 *Rev. Mod. Phys.* **54** 437
- [2] Castro Neto A H, Guinea F, Peres N M R, Novoselov K S and Geim A K 2009 *Rev. Mod. Phys.* **81** 109
- [3] Mucciolo E R and Lewenkopf C H 2010 *J. Phys.: Condens. Matter* **22** 273201
- [4] Molitor F, Güttinger J, Stampfer C, Dröscher S, Jacobsen A, Ihn T and Ensslin K 2011 Electronic properties of graphene nanostructures *J. Phys.: Condens. Matter* **23** 243201
- [5] Yuan S, Roldán R, De Raedt H and Katsnelson M L 2011 *Phys. Rev. B* **84** 195418
- [6] Scharf B, Perebeinos V, Fabian J and Avouris P 2013 *Phys. Rev. B* **87** 035414
- [7] Geim A K and Novoselov K S 2007 *Nature Mater.* **6** 183
- [8] Kurokawa Y, Nomura S, Takemori T and Aoyagi Y 2000 *Phys. Rev. B* **61** 12616
- [9] Borysenko K M, Mullen J T, Barry E A, Paul S, Semenov Y G, Zavada J M, Buongiorno Nardelli M and Kim K W 2010 *Phys. Rev. B* **81** 121412

- [10] Aboud S J, Saraniti M, Goodnick S M and Fischetti M V 2012 *Proc. Int. Workshop on Computational Electronics* p 93
- [11] Park C H, Giustino F, Cohen M L and Louie S G 2008 *Nano Lett.* **8** 4229
- [12] Kitayama T, Minari H and Mori N 2009 *J. Phys.: Conf. Ser.* **193** 012112
- [13] Hwang E H and Das Sarma S 2008 *Phys. Rev. B* **77** 115449
- [14] Das Sarma S, Adam S, Hwang E H and Rossi E 2011 *Rev. Mod. Phys.* **83** 407
- [15] Bruzzone S and Fiori G 2011 *Appl. Phys. Lett.* **99** 222108
- [16] Akturk A and Goldsman N 2008 *J. Appl. Phys.* **103** 053702
- [17] Chauhan J and Guo J 2009 *Appl. Phys. Lett.* **95** 023120
- [18] Shishir R S, Ferry D K and Goodnick S M 2009 *J. Phys.: Conf. Ser.* **193** 012118
- [19] Shishir R S and Ferry D K 2009 *J. Phys.: Condens. Matter* **21** 232204
- [20] Shishir R S and Ferry D K 2009 *J. Phys.: Condens. Matter* **21** 344201
- [21] Shishir R S, Chen F, Xia J, Tao N J and Ferry D K 2009 *J. Comput. Electron.* **8** 43
- [22] Sule N and Knezevic I 2012 *J. Appl. Phys.* **112** 053702
- [23] Fang T, Konar A, Xing H and Jena D 2008 *Phys. Rev. B* **78** 205403
- [24] Bresciani M, Paussa A, Palestri P, Esseni D and Selmi L 2010 *Int. Electron Device Mtg. Tech. Dig.* vol 2010, pp 32.1.1–4
- [25] Betti A, Fiori G, Iannaccone G and Mao Y 2009 *Int. Electron Device Mtg. Tech. Dig.* vol 2009, p 897
- [26] Betti A, Fiori G and Iannaccone G 2010 *Int. Electron Device Mtg. Tech. Dig.* vol 2010 pp 32.2.1–4
- [27] Betti A, Fiori G and Iannaccone G 2011 *IEEE Trans. Electron Devices* **58** 691
- [28] Wakabayashi K, Takane Y, Yamamoto M and Sigrist M 2009 *New J. Phys.* **11** 095016
- [29] Sinitzkii A, Fursina A A, Kosynkin D V, Higginbotham A L, Natelson D and Tour J M 2009 *Appl. Phys. Lett.* **95** 253108
- [30] Long M Q, Tang L, Wang D, Wang L and Shuai Z 2009 *J. Am. Chem. Soc.* **131** 17728
- [31] Wang G 2012 *Chem. Phys. Lett.* **533** 74
- [32] Wang J, Zhao R, Yang M, Liu Z and Liu Z 2013 *J. Chem. Phys.* **138** 084701
- [33] Fischetti M V and Narayanan S 2011 *J. Appl. Phys.* **110** 083713
- [34] Fratini S and Guinea F 2008 *Phys. Rev. B* **77** 195415
- [35] Perebeinos V, Rotkin S, Petrov A and Avouris P 2009 *Nano Lett.* **9** 312
- [36] Rotkin S, Perebeinos V, Petrov A and Avouris P 2009 *Nano Lett.* **9** 1850
- [37] Konar A, Fang T and Jena D 2010 *Phys. Rev. B* **82** 115452
- [38] Ong Z-Y and Fischetti M V 2012 *Phys. Rev. B* **86** 165422
- [39] Ong Z-Y and Fischetti M V 2012 *Phys. Rev. B* **86** 199904
- [40] Ong Z-Y and Fischetti M V 2013 *Phys. Rev. B* **88** 045405
- [41] Ong Z-Y and Fischetti M V 2013 *Appl. Phys. Lett.* **102** 183506
- [42] Hwang E H, Adam S and Das Sarma S 2007 *Phys. Rev. Lett.* **98** 186806
- [43] Chen J, Jang C, Xiao S, Ishigami M and Fuhrer M S 2008 *Nature Nanotechnol.* **3** 206
- [44] Chen J, Jang C, Adam S, Fuhrer M S, Williams E D and Ishigami M 2008 *Nature Phys.* **4** 377
- [45] Adam S, Hwang E H, Galitski V M and Das Sarma S 2007 *Proc. Natl Acad. Sci.* **104** 18392
- [46] Adam S, Hwang E H, Rossi E and Das Sarma S 2009 *Solid State Commun.* **149** 1072
- [47] Ong Z-Y and Fischetti M V 2012 *Phys. Rev. B* **86** 121409
- [48] Car R and Parrinello M 1985 *Phys. Rev. Lett.* **55** 2471
- [49] Koskinen P, Malola S and Hakkinen H 2008 *Phys. Rev. Lett.* **101** 115502
- [50] Li Y, Zhou Z, Shen P and Chen Z 2009 *J. Phys. Chem. C* **113** 15043
- [51] Peng X and Velasquez S 2011 *Appl. Phys. Lett.* **98** 023112
- [52] Wang L W, Kim J and Zunger A 1999 *Phys. Rev. B* **58** 5678
- [53] Fischetti M V, Fu Bo, Narayanan S and Kim J 2011 *Nano-Electronic Devices: Semiclassical and Quantum Transport Modeling* ed D Vasileska and S M Goodnick (New York: Springer) pp 183–247
- [54] Saslow W, Bergstresser T K and Cohen M L 1966 *Phys. Rev. Lett.* **16** 354
- [55] Hemstreet L H Jr, Fong C Y and Cohen M L 1970 *Phys. Rev. B* **2** 2054
- [56] Dresselhaus G, Dresselhaus M S and Mavroides J G 1966 *Carbon* **4** 433
- [57] Ajiki M and Ando T 1993 *Japan. J. Appl. Phys.* **62** 1255
- [58] Reich S, Thomsen C and Ordejón P 2002 *Phys. Rev. B* **65** 155411
- [59] Khoshnevisan B and Tabatabaeian Z S 2008 *Appl. Phys. A* **92** 371
- [60] Giannozzi P et al 2009 *J. Phys.: Condens. Matter* **21** 395502 (www.quantum-espresso.org)
- [61] Trevisanutto P E, Giorgetti C, Reining L, Ladisa M and Olevano V 2008 *Phys. Rev. Lett.* **101** 226405
- [62] Clar E 1972 *The Aromatic Sextet* (New York: Wiley)
- [63] Wassman T, Seitsonen A P, Saitta A M, Lazzeri M and Mauri F 2010 *J. Am. Chem. Soc.* **132** 3440
- [64] Ezawa M 2006 *Phys. Rev. B* **73** 045432
- [65] Ezawa M 2007 *Phys. Status Solidi c* **4** 489
- [66] Balaban A and Klein D J 2009 *J. Phys. Chem. C* **113** 19123
- [67] Tersoff J and Hamann D R 1983 *Phys. Rev. Lett.* **50** 1998
- [68] Tersoff J and Hamann D R 1985 *Phys. Rev. B* **31** 805
- [69] Kresse G and Hafner J 1995 *Phys. Rev. B* **47** 558
- [70] Kresse G 1993 *Thesis* Technische Universität Wien
- [71] Kresse G and Furthmüller J 1996 *Comput. Mater. Sci.* **6** 15
- [72] Kresse G and Furthmüller J 1996 *Phys. Rev. B* **54** 11169
- [73] Fujita M, Wakabayashi K, Nakada K and Kusakabe K 1996 *J. Phys. Soc. Japan* **65** 1920
- [74] Brey L and Fertig H A 2006 *Phys. Rev. B* **73** 235411
- [75] Sasaki K-I, Murakami S and Saito R 2006 *J. Phys. Soc. Japan* **75** 074713
- [76] Zhao P and Guo J 2009 *J. Appl. Phys.* **105** 034503
- [77] Son Y-W, Cohen M L and Louie S G 2006 *Phys. Rev. Lett.* **97** 216803
- [78] Barone V, Hod O and Scuseria G 2006 *Nano Lett.* **6** 2748
- [79] Yang L, Park C-H, Son Y-W, Cohen M L and Louie S G 2007 *Phys. Rev. Lett.* **99** 186801
- [80] Sevincli H, Topsakal M and Ciraci S 2008 *Phys. Rev. B* **78** 245402
- [81] Li X, Wang X, Zhang L, Lee S-W and Dai H J 2008 *Science* **319** 1229
- [82] Querlioz D, Apertet Y, Valenkin A, Huet K, Bournel A, Galdin-Retailleau S and Dollfus P 2008 *Appl. Phys. Lett.* **92** 042108
- [83] Tseng F, Unluer D, Holcomb K, Stan M R and Ghosh A W 2009 *Appl. Phys. Lett.* **94** 223112
- [84] Reuter K and Scheffler M 2001 *Phys. Rev. B* **65** 035406
- [85] Chase J M W (ed) 1998 *NIST-JANAF Thermochemical Tables* 4th edn (Washington, DC: American Chemical Society)
- [86] Wassman T, Seitsonen A P, Saitta A M, Lazzeri M and Mauri F 2008 *Phys. Rev. Lett.* **101** 096402
- [87] Lu Y H, Wu R Q, Shen L, Yang M, Sha Z D, Cai Y Q, He P M and Feng Y P 2009 *Appl. Phys. Lett.* **94** 122111
- [88] Vanin M, Gath J, Thygesen K S and Jacobsen K W 2010 *Phys. Rev. B* **82** 195411
- [89] Seitsonen A P, Saitta A M, Wassman T, Lazzeri M and Mauri F 2010 *Phys. Rev. B* **82** 115425

- [90] Saito R, Dresselhaus G and Dresselhaus M S 1998 *Physical Properties of Carbon Nanotubes* (London: Imperial College Press)
- [91] Al-Jishi R and Dresselhaus G 1982 *Phys. Rev. B* **26** 4514
- [92] Maradudin A A, Montroll E W and Weiss G H 1971 *Solid State Physics, Supplement 3* (New York: Academic)
- [93] Zimmermann J, Pavone P and Cuniberti G 2008 *Phys. Rev. B* **78** 045410
- [94] Dubay O and Kresse G 2005 *Phys. Rev. B* **67** 35401
- [95] Baroni S, de Gironcoli S and Del Corso A 2001 *Rev. Mod. Phys.* **73** 515
- [96] Piscanec S, Lazzeri M, Mauri F, Ferrari A C and Robertson J 2004 *Phys. Rev. Lett.* **93** 185503
- [97] Lazzeri M and Mauri F 2007 *Phys. Rev. Lett.* **97** 266407
- [98] Lazzeri M, Attaccalite C, Wirtz L and Mauri F 2008 *Phys. Rev. B* **78** 081406
- [99] Milošević I, Dobardžić E, Mohr M, Thomsen C and Damjanović M 2010 *Phys. Rev. B* **81** 233410
- [100] Bolotin K, Sikes K, Jiang Z, Klima M, Fudenberg G, Hone J, Kim P and Stormer H 2008 *Solid State Commun.* **146** 351
- [101] Morozov S V, Novoselov K S, Katsnelson M I, Schedin F, Elias D C, Jaszczak J A and Geim A K 2008 *Phys. Rev. Lett.* **100** 016602
- [102] Elias D C *et al* 2011 *Nature Phys. Lett.* **7** 701
- [103] Mayorov A S *et al* 2011 *Nano Lett.* **11** 2396
- [104] Bardeen J and Shockley W 1950 *Phys. Rev.* **80** 72
- [105] Zhu W, Perebeinos V, Freitag M and Avouris P 2009 *Phys. Rev. B* **80** 235402
- [106] Siegel D A, Hwang C G, Fedoroiv A V and Lanzara A 2012 *New J. Phys.* **14** 095006
- [107] Suzuura H and Ando T 2002 *Phys. Rev. B* **65** 235412
- [108] Bresciani M, Palestri P, Esseni D and Selmi L 2009 *Proc. 2009 European Solid State Device Research Conf. (ESSDERC)* pp 480–3
- [109] Finkenstadt D, Pennington G and Mehl M J 2007 *Phys. Rev. B* **76** 121405
- [110] Ono S and Sugihara K 1966 *J. Phys. Soc. Japan* **21** 861
- [111] Sugihara K 1983 *Phys. Rev. B* **28** 2157
- [112] Perebeinos V, Tersoff J and Avouris P 2005 *Phys. Rev. Lett.* **94** 086802
- [113] Su W P, Schrieffer J R and Heeger A J 1979 *Phys. Rev. Lett.* **42** 1698
- [114] Su W P, Schrieffer J R and Heeger A J 1980 *Phys. Rev. B* **22** 2099
- [115] Vasko F T and Ryzhii V 2007 *Phys. Rev. B* **76** 233404
- [116] Pennington G and Goldsman N 2003 *Phys. Rev. B* **68** 045426
- [117] Stauber T, Peres N M R and Guinea F 2007 *Phys. Rev. B* **76** 205423
- [118] Lazzeri M, Piscanec S, Mauri F, Ferrari A C and Robertson J 2005 *Phys. Rev. Lett.* **95** 236802
- [119] Woods L M and Mahan G D 2000 *Phys. Rev. B* **61** 10651
- [120] Fischetti M V and Higman J M 1991 *Monte Carlo Device Simulation: Full Band and Beyond* ed K Hess (Norwell, MA: Kluwer Academic) pp 123–60
- [121] Dorgan V, Bae M H and Pop E 2010 *Appl. Phys. Lett.* **97** 082112
- [122] Pisana S, Lazzeri M, Casiraghi C, Novoselov K S, Geim A K, Ferrari A C and Mauri F 2007 *Nature Mater.* **6** 198
- [123] Charlier J C, Eklund P C, Zhu J and Ferrari A C 2007 *Carbon Nanotubes: Advanced Topics in the Synthesis, Structure, Properties and Applications* (Berlin: Springer) pp 673–709
- [124] Lazzeri M, Piscanec S, Mauri F, Ferrari A C and Robertson J 2006 *Phys. Rev. B* **73** 155426
- [125] Ziman M J 1960 *Electrons and Phonons* (Oxford: Clarendon)
- [126] Boguslawski P and Mycielski J 1977 *J. Phys. C: Solid State Phys.* **10** 2413
- [127] Fischetti M V and Laux S E 1993 *Phys. Rev. B* **48** 2244
- [128] Price P J 1985 *Phys. Rev. B* **32** 2643
- [129] Walukiewicz W, Ruda H E, Lagowski J and Gatos H C 1985 *Phys. Rev. B* **32** 2645
- [130] Tanatar B 1994 *J. Phys.: Condens. Matter* **5** 2203
- [131] Wunsch B, Stauber T, Sols F and Guinea F 2006 *New J. Phys.* **8** 318
- [132] Wang E H and Das Sarma S 2007 *Phys. Rev. B* **75** 205418
- [133] Mischenko E G 2007 *Phys. Rev. Lett.* **98** 216801
- [134] Gilat G and Raubenheimer L J 1966 *Phys. Rev.* **144** 390
- [135] Betti A, Fiori G and Iannaccone G 2011 *Appl. Phys. Lett.* **99** 242108
- [136] Amin N A, Ahmadi M T, Webb J F, Johari Z, Mousavi S M and Ismail R 2011 *Global J. Technol. Optim.* **2** 153
- [137] Dorgan V E, Behnam A, Conley H J, Bolotin K I and Pop E 2013 High-field electrical and thermal transport in suspended graphene *Nano Lett.* **13** 4581
- [138] Pop E 2013 private communication
- [139] Bae M H, Ong Z-Y, Estrada D and Pop E 2010 *Nano Lett.* **10** 4787
- [140] Jacoboni C and Reggiani L 1983 *Rev. Mod. Phys.* **55** 645
- [141] Zebrev G I 2011 *Nanotechnology and Nanomaterials, Physics and Applications of Graphene-Theory* ed S Mikhailov (Rijeka: Intech)
- [142] Serov A Y, Ong Z-Y, Fischetti M V and Pop E 2014 Role of substrate in high-field transport in graphene *Phys. Rev. B* submitted
- [143] Ouyang Y, Wang X, Dai H and Guo J 2008 *Appl. Phys. Lett.* **92** 243124
- [144] Yoon Y, Nikonorov D E and Salahuddin S 2011 *Appl. Phys. Lett.* **98** 203503
- [145] Zhou J and Dong J 2007 *Appl. Phys. Lett.* **91** 173108
- [146] Williams P F and Bloch A 1974 *Phys. Rev. B* **10** 1097
- [147] Brey L and Fertig H A 2007 *Phys. Rev. B* **75** 125434
- [148] Jin S, Fischetti M V and Tang T-W 2007 *J. Appl. Phys.* **102** 083715
- [149] Konar A, Fang T and Jena D 2011 *Phys. Rev. B* **84** 085422
- [150] Li Y, Jiang X, Liu Z and Liu Z 2010 *Nano Res.* **3** 545
- [151] Prange R E and Nee T W 1968 *Phys. Rev.* **168** 779
- [152] Sakaki H, Noda T, Hirakawa K, Tanaka M and Matsusue T 1987 *Appl. Phys. Lett.* **51** 1934
- [153] Jin S, Fischetti M V and Tang T-W 2007 *IEEE Trans. Electron Devices* **54** 2191
- [154] Gallagher P, Todd K and Goldhaber-Gordon D 2010 *Phys. Rev. B* **81** 115409
- [155] Basu D, Gilbert M J, Register L F and Banerjee S K 2008 *Appl. Phys. Lett.* **92** 042114
- [156] Zeng L, Liu X Y, Du G, Kang J F and Han R Q 2009 *Proc. 2009 Simulation of Semiconductor Processes and Devices (SISPAD)* pp 1–4
- [157] Dubois S M M, Lopez-Bezanilla A, Cresti A, Triozen F, Biel B, Charlier J-C and Roche S 2010 *ACS Nano* **4** 1971
- [158] Areshkin D A, Gunlycke D and White C T 2007 *Nano Lett.* **7** 204
- [159] Gunlycke D, Areshkin D A and White C T 2007 *Appl. Phys. Lett.* **90** 142104
- [160] Mucciolo E R, Castro Neto A H and Lewenkopf C H 2009 *Phys. Rev. B* **79** 075407
- [161] Martin I and Blanter Y M 2009 *Phys. Rev. B* **79** 235132
- [162] Evaldsson M, Zozoulenko I V, Xu H and Heinzel T 2008 *Phys. Rev. B* **78** 161407
- [163] Cresti A and Roche S 2009 *New J. Phys.* **11** 095004
- [164] Luisier M and Klimeck G 2009 *Appl. Phys. Lett.* **94** 223505
- [165] Yoon Y and Guo J 2007 *Appl. Phys. Lett.* **91** 073103
- [166] Yang Y and Murali R 2010 *Electron Device Lett.* **31** 237
- [167] Berger B *et al* 2006 *Science* **312** 1191
- [168] Cai J *et al* 2010 *Nature* **466** 470
- [169] Jiao L, Zhang L, Wang X, Diankov G and Dai H 2009 *Nature* **458** 877
- [170] Kosynkin D V, Higginbotham A L, Sinitskii A, Lomeda J R, Dimiev A, Price B K and Tour J M 2009 *Nature* **458** 872
- [171] Cresti A, Nemec N, Biel B, Niebler G, Triozen F, Cuniberti G and Roche S 2008 *Nano Res.* **1** 361

- [172] Sols F, Guinea F and Castro Neto A H 2007 *Phys. Rev. Lett.* **99** 166803
- [173] Todd K, Cou H-T, Amasha S and Goldhaber-Gordon D 2009 *Nano Lett.* **9** 416
- [174] Stampfer C, Guttinger J, Hellmuller S, Molitor F, Ensslin K and Ihn T 2009 *Phys. Rev. Lett.* **102** 056403
- [175] Behnam A, Lyons A S, Bae M H, Chow E K, Islam S, Neumann C M and Pop E 2012 *Nano Lett.* **12** 4424
- [176] Lemme M, Echtermeyer T, Baus M, Szafranek B, Bolten J, Schmidt M, Wahlbrink T and Kurz H 2008 *Solid-State Electron.* **52** 514
- [177] Moon J *et al* 2010 *Electron Device Lett.* **31** 260
- [178] Pezoldt J, Hummel C, Hanisch A, Hotovy I, Kadlecikova M and Schwierz F 2010 *Phys. Status Solidi c* **7** 390
- [179] Kim S, Nah J, Jo I, Shahrjerdi D, Colombo L, Yao Z, Tutuc E and Banerjee S K 2009 *Appl. Phys. Lett.* **94** 062107
- [180] Lee B, Mordi G, Kim M J, Chabal Y J, Vogel E M, Wallace R M, Cho K J, Colombo L and Kim J 2010 *Appl. Phys. Lett.* **97** 043107
- [181] Fischetti M V, Neumayer D A and Cartier E A 2001 *J. Appl. Phys.* **90** 4587
- [182] Fuchs R and Kliewer K L 1965 *Phys. Rev.* **140** A2076
- [183] Wang S Q and Mahan G D 1972 *Phys. Rev. B* **6** 4517
- [184] Hess K and Vogl P 1979 *Solid State Commun.* **30** 797
- [185] Moore B T and Ferry D K 1980 *J. Appl. Phys.* **51** 2603
- [186] Xiu K 2011 *Simulation of Semiconductor Processes and Devices (SISPAD) Int. Conf.* (New York: IEEE) pp 35–8
- [187] Ishigami M, Chen J H, Cullen W G, Fuhrer M S and Williams E D 2007 *Nano Lett.* **7** 1643
- [188] Meric I, Han M Y, Young A F, Ozyilmaz B, Kim P and Shepard K L 2008 *Nature Nanotechnol.* **3** 654
- [189] Li X, Barry E A, Zavada J M, Buongiorno-Nardelli M and Kim K W 2010 *Appl. Phys. Lett.* **97** 232105
- [190] Zou K, Hong X, Keefer D and Zhu J 2010 *Phys. Rev. Lett.* **105** 126601
- [191] Pirkle A, Chan J, Venugopal A, Hinojos D, Magnuson C W, McDonnell S, Colombo L, Vogel E M, Ruoff R S and Wallace R M 2011 *Appl. Phys. Lett.* **99** 122108
- [192] Ando T 2006 *J. Phys. Soc. Japan* **75** 074716
- [193] Chen F, Xia J L and Tao N J 2009 *Nano Lett.* **9** 1621
- [194] Ponomarenko L A, Yang R, Mohiuddin T, Katsnelson K, Novoselov K S, Morozov S V, Zhukov A, Schedin F, Hill E and Geim A K 2009 *Phys. Rev. Lett.* **102** 206603
- [195] Jang C, Adam S, Chen J, Williams E, Das Sarma S and Fuhrer M 2008 *Phys. Rev. Lett.* **101** 146805
- [196] Fallahazad B, Kim S, Colombo L and Tutuc E 2010 *Appl. Phys. Lett.* **97** 123105
- [197] Fallahazad B, Lee K, Lian G, Kim S, Corbet C, Ferrer D, Colombo L and Tutuc E 2012 *Appl. Phys. Lett.* **100** 093112
- [198] Ong Z-Y and Fischetti M V 2013 On the enhancement of room temperature electron mobility in top-gated MoS₂ *Phys. Rev. Lett.* at press
- [199] Fischetti M V, Fu Bo and Vandenberghe W G 2013 Theoretical study of the gate leakage current in sub-10 nm field-effect transistors *IEEE Trans. Electron Devices* at press